

Saturn's Magnetospheric Configuration

Tamas I. Gombosi, Thomas P. Armstrong, Christopher S. Arridge, Krishan K. Khurana,
Stamatios M. Krimigis, Norbert Krupp, Ann M. Persoon and Michelle F. Thomsen

Tamas I. Gombosi

Center for Space Environment Modeling, Department of Atmospheric, Oceanic and Space Sciences, The University of Michigan, Ann Arbor, Michigan, USA, e-mail: tamas@umich.edu

Thomas P. Armstrong

Fundamental Technologies, LLC, Lawrence, Kansas, USA, e-mail: armstrong@ftecs.com

Christopher S. Arridge

Mullard Space Science Laboratory, University College London, London, United Kingdom; and Centre for Planetary Sciences, University College London, London, United Kingdom, e-mail: chris.arridge@physics.org

Krishan K. Khurana

Institute of Geophysics and Planetary Physics, University of California at Los Angeles, Los Angeles, California, USA, e-mail: kkhurana@igpp.ucla.edu

Stamatios M. Krimigis

Applied Physics Laboratory, Johns Hopkins University, Laurel, Maryland, USA; and Center of Space Research and Technology, Academy of Athens, Athens, Greece, e-mail: tom.krimigis@jhuapl.edu

Norbert Krupp

Max-Planck Institute for Solar System Research, Katlenburg-Lindau, Germany, e-mail: krupp@mps.mpg.de

Ann Persoon

University of Iowa, Iowa City, Iowa, USA, e-mail: ann-persoon@uiowa.edu

Michelle Thomsen

Los Alamos National Laboratory, Los Alamos, New Mexico, USA, e-mail: mthomsen@lanl.gov

1 Introduction

Twenty five years is a human generation. Children are born, raised, educated and reach maturity in a quarter of a century. In space exploration, however, twenty five years is a very long time. Twenty five years after the launch of the first Sputnik, Saturn was visited by three very successful spacecraft: Pioneer 11 (1979), Voyager 1 (1980) and Voyager 2 (1981). The flyby trajectories are shown in Fig. 1. Twenty five years after the first Saturn flyby by Pioneer 11 the most advanced planetary probe ever built started orbiting Saturn and deployed a lander to reveal the mysteries of Titan. One can only guess the exciting future missions we may have 25 years after Cassini.

1.1 Pre-Cassini Understanding

The three pre-Cassini flybys provided a very good overall understanding of the large-scale magnetospheric configuration. The main controlling factors were the following:

Saturn has a dipole-like intrinsic magnetic field with the dipole axis closely aligned with the axis of planetary rotation (within about 1°). The equatorial magnetic field ($B_S \approx 2 \times 10^{-5}$ T) is very close to the equatorial magnetic field of Earth ($B_E \approx 3 \times 10^{-5}$ T) and about an order of magnitude smaller than that of Jupiter ($B_J \approx 4 \times 10^{-4}$ T).

The equatorial radius of Saturn ($R_S \approx 6.0 \times 10^4$ km) is comparable to the radius of Jupiter ($R_J \approx 7.1 \times 10^4$ km) and is about an order of magnitude larger than the radius of Earth ($R_E \approx 6.4 \times 10^3$ km). The rotation periods for Jupiter ($T_J \approx 10^h$) and Saturn ($T_S \approx 10.5^h$) are quite close, and they rotate about 2.5 times faster than Earth ($T_E \approx 24^h$). Centrifugal accelerations at the planetary equator, consequently, are comparable at Jupiter and Saturn, and they exceed that of Earth by about 1.5 orders of magnitude.

Most of the plasma in Saturn's magnetosphere is of internal origin, with the rings, the icy satellites and Titan identified as the primary plasma sources. It was recognized that the magnetospheric plasma is dominated by heavy ions (in the mass range of 10 – 20 amu), but due to the limited mass resolution of the plasma instrument the dominant heavy ion was not identified (both nitrogen and oxygen were suspected with the debate settling on oxygen during the 90's [147]). The total internal mass source was estimated as $10^{27} - 10^{28.5}$ molecules per second (or $\sim 10^{1.5} - 10^{2.5}$ kg/s), a large uncertainty due to orbital and instrument

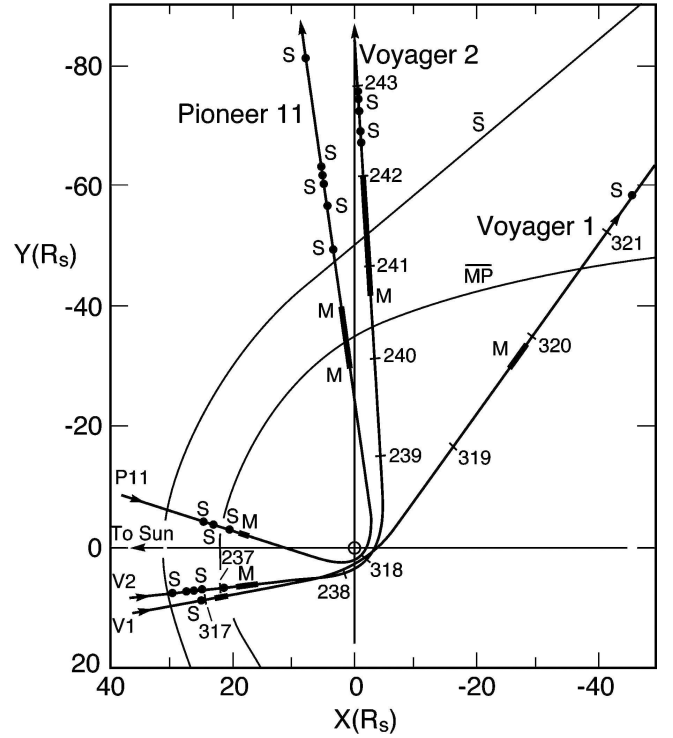


Fig. 1 Trajectories of the Pioneer 11, Voyager 1, and Voyager 2 spacecraft projected onto Saturn's equatorial plane. Observed bow shock (S) and magnetopause (MP) crossing are also shown (from [166]).

Fig. 2 Post-Voyager illustration of Saturn's magnetosphere. Cold regions are colored blue, regions of intermediate temperature are purple (blue plus red), and the hot regions are red. The satellite positions (M, E, T, D, and R for Mimas, Enceladus, Tethys, Dione, and Rhea, respectively), E ring (gray shaped rectangular region), neutral hydrogen cloud (circular region with white dots), and magnetopause boundary (MP) are displayed. (from [166])

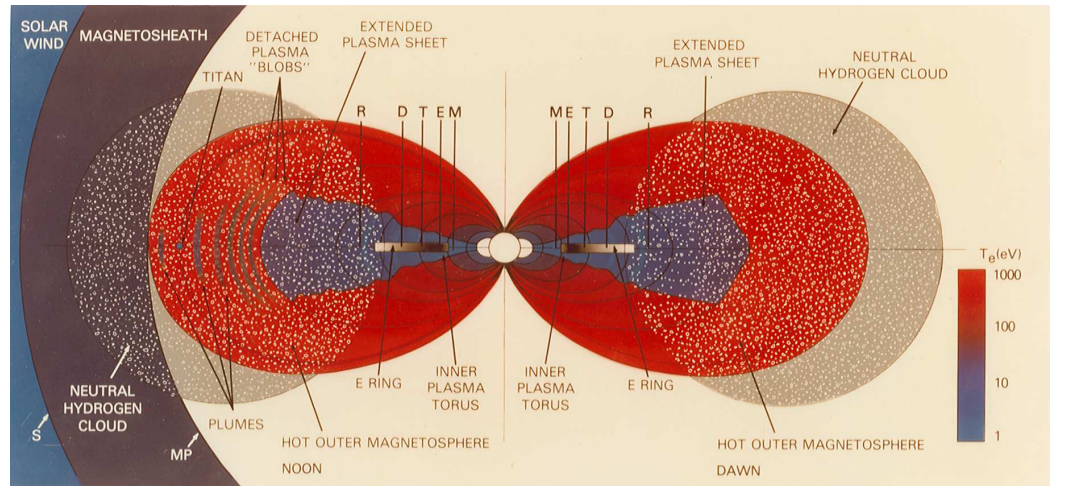
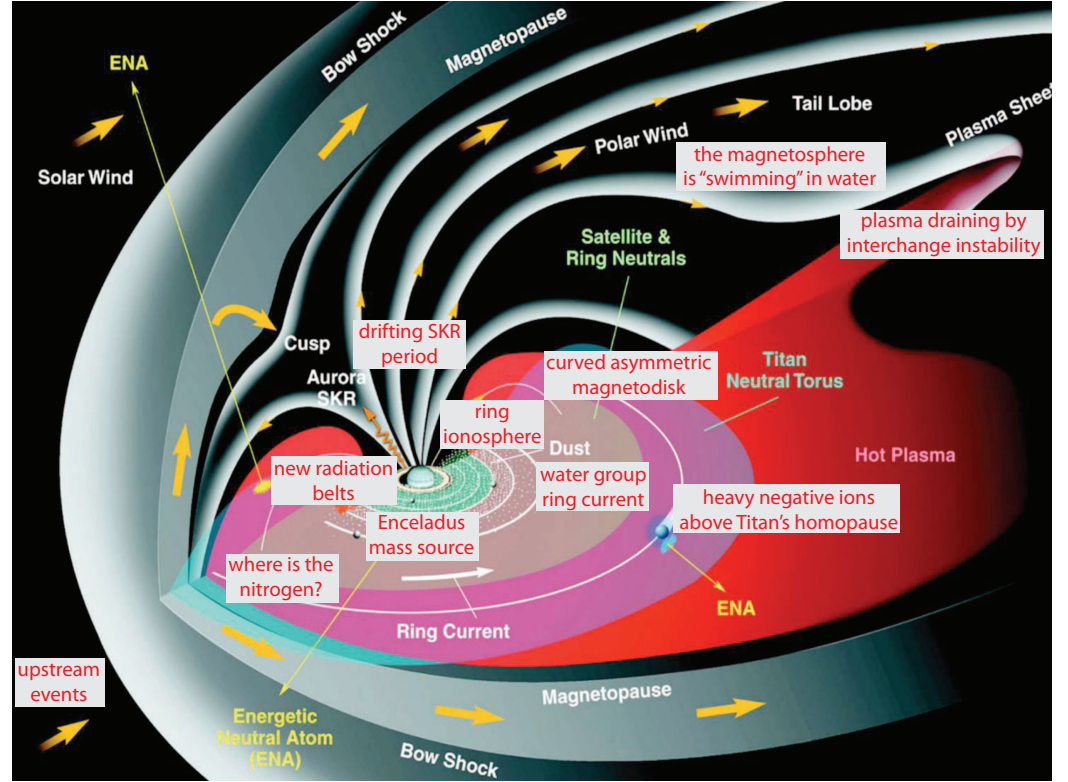


Fig. 3 Some of the exciting new discoveries made by the Cassini science teams during the Cassini Prime Mission. These discoveries are discussed in detail either in this Chapter or in the other magnetospheric Chapters of this book [35, 118, 126]. (background figure courtesy of the MIMI team).



limitations. In this respect the Saturnian system is again similar to Jupiter, where the Iogenic internal plasma source is about 10^{28} ($\sim 10^3$ kg/s) heavy molecules per second. This is a big difference from Earth, where under quiet conditions the ionospheric plasma source plays a relatively unimportant role in controlling the overall magnetospheric configuration.

Magnetic field lines are increasingly stretched as more and more plasma is added in the equatorial mass loading region. The increasing plasma content per unit flux tube area requires the transfer of more and more momentum from the rotating ionosphere to the increasingly stretched field line. However, the finite ionospheric conductivity limits this momentum transfer, and consequently, the angular velocity of the ‘heavy’ equatorial part of the magnetic field line exhibits an increasing corotation lag [70, 85]. Finally, the field line becomes so heavy that the ionosphere is unable to drag it around any more and corotation “breaks down” [70, 85] near a radial distance of

$$r_0 = \left(\frac{4M_S}{\mu_0 \eta_s \Omega_S^2} \right)^{1/4} \quad (1)$$

where M_S is the magnetic moment of Saturn, μ_0 is the magnetic permeability of vacuum, Ω_S is the angular velocity of the neutral thermosphere and η_s is the flux tube plasma content (per unit flux tube area) in the mass addition region. Expression (1) yields a corotation breakdown radius of $\sim 15R_S$ assuming a flux tube content of $\sim 10^{-3}$ g T $^{-1}$ cm $^{-2}$.

The solar wind encompassing Saturn’s magnetosphere is two orders of magnitude more tenuous than it is at Earth orbit. The interplanetary magnetic field at Saturn is about an order of magnitude weaker than at Earth and its nominal direction is nearly azimuthal. Under these conditions the solar wind was thought to have a relatively weak control over the magnetospheric configuration.

A summary of the pre-Cassini understanding of Saturn’s magnetospheric configuration is shown in Fig. 2. We note that no direct plasma observations were available from the distant magnetotail and therefore the schematics focuses on the region within about $30 R_S$.

1.2 Major Cassini Discoveries

The Cassini mission resulted in a number of exciting new discoveries. Some of these discoveries are noted in Fig. 3:

- During its approach to Saturn the Cassini spacecraft detected energetic (~ 100 keV/charge) magnetospheric ions (such as He^+ and O^+) upstream of the bow shock whenever the spacecraft was magnetically connected to Saturn's magnetosphere [113].
- During the initial Saturn Orbit Insertion (SOI) the spacecraft discovered a "ring ionosphere" dominated by water group ions originating from the icy material composing Saturn's spectacular rings [184].
- The SOI orbit also brought some other important discoveries, such as the fact that very few nitrogen ions were detected in the magnetosphere [174]. This was a surprise, since before the arrival of the Cassini spacecraft Titan was thought to be a major source of magnetospheric nitrogen. For a more complete summary of the results obtained during SOI we refer to the review paper by *André et al.* [8].
- The MIMI instrument discovered a new radiation belt inside the D ring [111].
- The plasma wave instrument (RPWS) discovered a very complicated, drifting periodicity of Saturn's kilometric radiation (SKR). A detailed discussion of this phenomenon can be found in a separate Chapter in this book [118].
- Cassini discovered that Saturn's ring current is primarily composed of accelerated water group ions [159]. This is not surprising in light of the discovery that nearly all major magnetospheric plasma sources are water dominated. These include the rings, the icy satellites and especially Enceladus, that turned out to be the dominant mass source for Saturn's magnetospheric plasma [197].
- The plasma produced inside Saturn's magnetosphere is primarily transported through the system by the interchange instability (see the chapter by *Mauk et al.* [126] in this book) and eventually drained by reconnection.
- Cassini discovered that Saturn has a bowl-shaped current sheet [14] that is due to the interplay between the tilt of Saturn's rotational axis and the direction of the solar wind flow at Saturn's orbit.
- Very heavy negatively charged particles (most likely aerosols) were discovered above the homopause of Titan [198]. This was a big surprise and the interpretation of this discovery is still under way.

1.3 Earth, Jupiter and Saturn

In order to put the results of the Cassini mission in perspective we briefly compare the magnetospheres of Earth, Jupiter and Saturn. Before Cassini the conventional wisdom was that strongly magnetized planets can have two distinct types of magnetospheres: solar wind controlled and internally controlled.

The terrestrial magnetosphere is the prototypical example of a solar wind controlled magnetosphere. As can be seen from the information presented in Table 1, Earth is a slow rotator (the corotational electric field is only dominant in the immediate vicinity of the planet) with a relatively small internal mass source originating from the high latitude ionosphere (~ 1 kg/s). The resulting solar wind interaction is usually referred to as the "Dungey cycle" [59]. This process starts at the dayside magnetopause

Table 1 Comparison of physical parameters of Earth, Jupiter and Saturn.

Parameter	Earth	Jupiter	Saturn
Heliocentric distance (AU)	1	5.2	9.5
Average IMF magnitude [nT]	4	1	0.5
Nominal Parker spiral angle from radial direction	45°	80°	85°
Typical solar wind ram pressure (nPa)	1.7	0.07	0.015
Equatorial radius	$1 R_E = 6,371$ km	$1 R_J = 71,492$ km $= 11.2 R_E$	$1 R_S = 60,268$ km $= 9.45 R_E$
Magnetic moment (T m^3)	7.75×10^{15}	1.55×10^{20}	4.6×10^{18}
Dipole tilt	10.5°	10°	$< 1^\circ$
Equatorial magnetic field (μT)	31	420	20
Typical subsolar bow shock distance	$\sim 13 R_E$	$\sim 70 R_J$	$\sim 27 R_S$
Typical subsolar magnetopause distance	$\sim 10 R_E$	$\sim 50 R_J$	$\sim 22 R_S$
Solar wind transport time from subsolar bow shock to terminator	$\sim 3.5^m$	$\sim 3.5^h$	$\sim 1.1^h$
Magnetospheric plasma source (kg/s)	~ 1	$\sim 10^3$	~ 300
Equatorial rotation period (hours)	23.934	9.925	10.53
Equatorial angular velocity (s^{-1})	7.29×10^{-5}	1.76×10^{-4}	1.66×10^{-4}
Equatorial rotation velocity (km/s)	0.465	12.6	9.87
Equatorial gravitational acceleration (m/s^2)	9.78	24.8	8.96
Centrifugal acceleration at the equator (m/s^2)	0.034	2.22	1.62
Corotation electric field at equator (mV/m)	14.2	5290	197
Solar wind motional electric field (mV/m)	1.6	0.4	0.2
Radius where $E_{\text{corot}} = 0.1 E_{\text{sw}}$	$3 R_E$	$115 R_J$	$31 R_S$

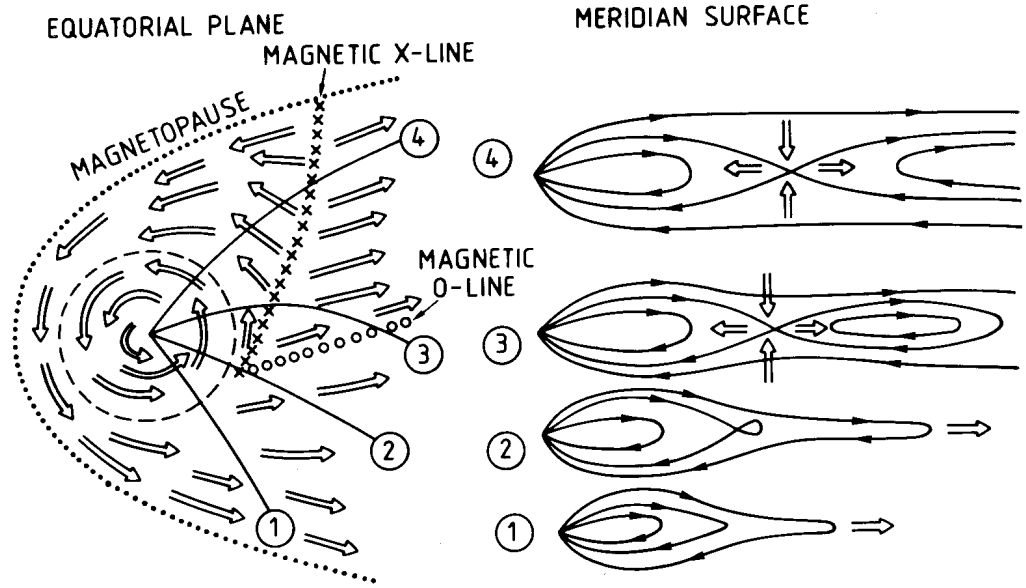


Fig. 4 Schematic representation of plasma flow in the equatorial plane (left panel) and of the associated magnetic field and plasma flow in a sequence of meridional cuts (right panel) [193].

where reconnection between the planetary magnetic field lines and the southward component of the IMF can take place along an extended region. This reconnection creates a set of open magnetic field lines originating from the high-latitude ionosphere and extending to the free flowing solar wind. The open (interplanetary) ends of these field lines are moving with the ambient solar wind speed, while the ionospheric ends are convecting antisunward. These open field lines form the open flux magnetospheric tail lobes. Eventually, the open flux tubes close again by reconnecting in the plasma sheet. This process forms stretched closed flux tubes on the Earthward side of the tail reconnection line, which contract back toward the Earth and eventually flow to the dayside where the process can repeat. On the other side, “disconnected” field lines accelerate the tail plasma downstream and eventually ‘accommodate’ it into the solar wind. The key feature of the “Dungey cycle” is therefore the magnetospheric convection controlled by reconnection.

Jupiter represents a prime example of a magnetosphere where the solar wind only plays a minor role. Jupiter is a fast rotator with a strong surface magnetic field (see Table 1). As a consequence, internal processes dominate the magnetosphere out to about $100R_J$ and the solar wind interaction (the Dungey cycle) is only marginally important. The corotational electric field far exceeds the motional electric field in the solar wind, and Io produces about 10^3 kg/s plasma deep inside the magnetosphere. This plasma source adds considerable “new mass” to the corotating magnetic flux tubes and eventually stretches them outward.

When a mass-loaded heavy magnetic flux tube stretches beyond the corotation breakdown distance, the plasma will continue moving outward unless there is some process that inhibits this motion. On the dayside the magnetopause acts as a barrier and forces the magnetic field line to move along the inner boundary of the magnetosphere thus forcing a corotation-like motion around the planet. On the nightside, however, the plasma can move without much resistance into the low pressure magnetotail. The magnetic field lines remain attached to the corotating ionosphere at one end and to the outward moving heavy equatorial plasma on the other end. Eventually the field line becomes so stretched and thin that a magnetic ‘O’ line is formed and a plasmoid is formed that can now freely move down the magnetotail. On the planetary side the newly shortened field line is ‘shed’ of its plasma content, and the magnetic stress pulls the equatorial part of the field line towards the planet, restoring the flow toward corotation. This process is called the “Vasyliunas cycle” [193] and it is shown in Fig. 4.

As can be seen from Table 1, Saturn falls somewhere between Earth and Jupiter. It is a fast rotator, but the equatorial magnetic field is comparable to that of Earth. The magnetospheric mass source is a factor of 3 smaller than that of Jupiter, and the corotation electric field is dominant inside a few tens of R_S . As a result of this intermediate parameter range Saturn’s magnetosphere exhibits both a Dungey cycle and a Vasyliunas cycle at the same time [18]. This fact makes the kronian magnetosphere even more fascinating and complex than the magnetospheres of Earth and Jupiter.

Badman and Cowley [18] pointed out that in the outer magnetosphere the rotational flux transport and the Dungey cycle are of comparable importance. Regions driven by planetary rotation should be dominated by heavy-ion plasmas originating from internal moon sources. The Dungey cycle layers should principally contain hot light ions originating from either the planet’s ionosphere or the solar wind.

A conceptual drawing (based on [46]) of Saturn’s ionosphere-magnetosphere coupling and plasma circulation is shown in Fig. 5. There are three distinct plasma convection regions in the ionosphere and magnetosphere. Closest to the planet ($r \leq 3R_S$)

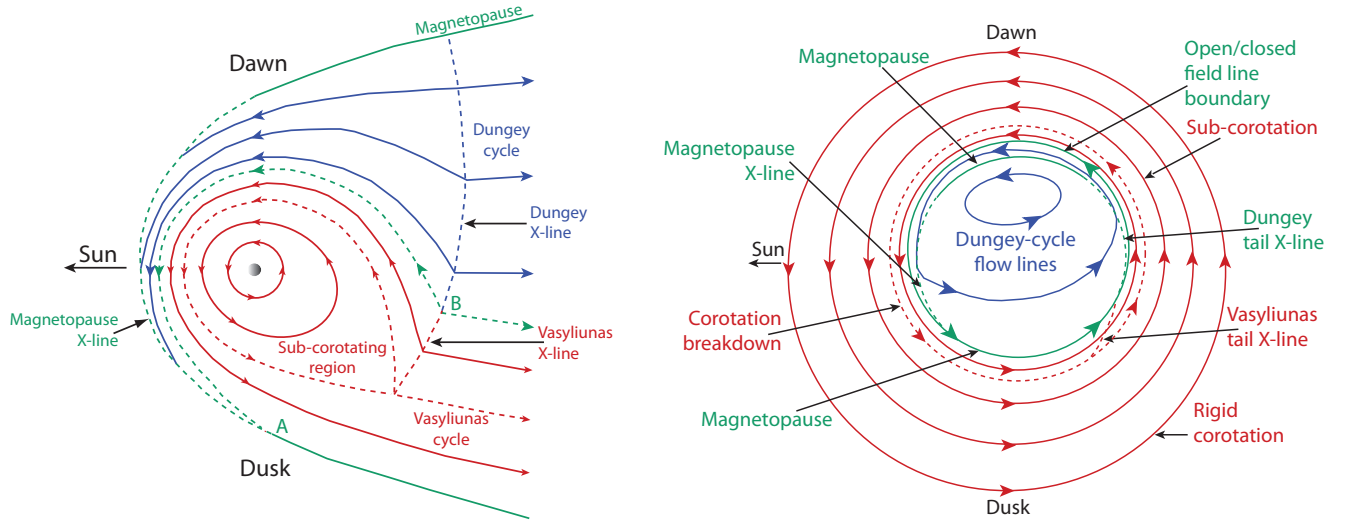


Fig. 5 Schematic representation of ionosphere-magnetosphere coupling at Saturn [46]). The left panel shows plasma convection in the equatorial plane of the magnetosphere and the right panel shows ionospheric convection in the northern high-latitude ionosphere. Three distinct convection regions can be distinguished: corotation, Vasyliunas-type plasmoid formation [193] and Dungey-type reconnection driven circulation [59].

the plasma corotates with the upper atmosphere. This region is shown by arrowed solid red circles in the ionosphere and arrowed solid red lines in the equatorial plane of the magnetosphere. Sub-corotation develops at larger radial distances as the magnetic field lines become increasingly mass loaded. The final breakdown of corotation is shown by the arrowed dashed red line both in the magnetosphere and in the ionosphere.

The second convection region starts at the corotation breakdown and it includes the Vasyliunas cycle. Beyond the corotation breakdown plasmoid formation “drains” magnetospheric plasma as suggested by Vasyliunas [193] (see Fig. 4). The associated X-line is shown by the dashed red line. In reality this is a highly intermittent process and numerical simulations indicate that on the dusk side small plasmoids containing plasma “blobs” are released from the stretched and tailward moving magnetic field lines. Eventually these plasma blobs evolve into a pinching of the field line and the Vasyliunas X-line is formed. Flux tubes that shed their plasma load in this way are “buoyant” in the centrifugal force and return to the inner magnetosphere through a process of flux-tube interchange described more fully in [126], thus completing the magnetic flux transport cycle.

The third distinct convection region is where the Dungey cycle [59] takes place. This process starts at the dayside magnetopause where reconnection between the planetary magnetic field lines and the northward component of the IMF can take place along an extended region (note that Saturn’s magnetic moment is oppositely oriented as the magnetic moment of Earth). This reconnection creates a set of open magnetic field lines originating from the high-latitude ionosphere and extending to the free flowing solar wind. The open (interplanetary) ends of these field lines are moving with the ambient solar wind speed, while the ionospheric ends are convecting antisunward as shown in the right panel of Fig. 5 (solid blue lines with arrows). On the dusk side these open field lines form the open flux tail lobes and they stay above the equatorial plane at all times. Point ‘A’ is at the dusk-side magnetopause and it represents the end of the dayside reconnection line. At point ‘B’ the lobe field lines start reconnecting and this point marks the duskward end of the Dungey-type tail X-line. This X-line is marked with dashed blue line in the left panel of Fig. 5. The Dungey cycle return flow takes place on the dawn side of the magnetosphere and it is compressed on the dayside due to the narrowing channel between the Vasyliunas cycle region and the magnetopause. The boundary between the Vasyliunas and Dungey cycle regions is marked by the arrowed green dashed line in the left panel of Fig. 5. Such Dungey cycle flux tubes, containing dominantly solar wind plasma, can also potentially mingle with flux tubes carrying inner magnetospheric plasma and may enter the inner magnetosphere via flux-tube interchange, as mentioned above.

2 Magnetic Field

2.1 Intrinsic Magnetic Field

The first *in-situ* observations of Saturn's intrinsic magnetic field were done during the Pioneer 11 flyby in 1979 [173, 3]. Combined with the magnetic field observations by the two Voyager spacecraft [40] the early measurements provided a surprisingly accurate picture of Saturn's intrinsic magnetic field. It can be described by a slightly displaced magnetic dipole that is very closely aligned with the planetary rotation axis [173, 40]. Detailed studies of the Cassini observations basically confirmed this conclusion and added some additional details.

The modeling of intrinsic planetary magnetic fields has a rich heritage stretching back into the 19th century with pioneering work by Gauss. Within planetary magnetospheres there can usually be found a region where the magnetospheric volume currents are weak and the field can be considered to be approximately curl-free (this is the region where the effects of external current systems can be neglected). Under this approximation the field in this region can be written as the gradient of some magnetic scalar potential ($\mathbf{B} = -\nabla\psi$), usually using spherical harmonics, which satisfies Laplace's equation ($\nabla^2\psi = 0$):

$$\psi(r, \theta, \phi) = a \sum_{n=0}^{\infty} \left(\frac{a}{r}\right)^{n+1} \sum_{m=0}^n P_n^m(\cos\theta) [g_n^m \cos(m\phi) + h_n^m \sin(m\phi)] \quad (2)$$

where a is the radius of the planet and r , θ and ϕ are spherical planetocentric coordinates. In expansion (2) the values g_n^m and h_n^m are referred to as the Gauss coefficients of the field model and indicate how strong each 'mode' contributes to producing the total field. The values of n are described as the degree and m the order of the expansion. The choice of a Schmidt quasi-normalization allows one to directly compare the contributions from each term and assess how important each contribution is. To determine the Gauss coefficients, least squares methods are typically used to minimize the squared deviation between a model field described by equation (2) and a set of magnetometer observations.

For such a model, one can only be sure of a unique solution for ψ if measurements are available which completely cover a closed surface about the origin. Spacecraft trajectories constitute single curves in space and because of this the values of Gauss coefficients from such models are not unique. Cross-coupling and mutual dependence between the coefficients can occur. Whilst the model may provide an excellent fit to the data along a given trajectory, it might be very wrong away from that trajectory. Furthermore, terms of degree n scale as $r^{-(n+1)}$ and, consequently, a large number of spacecraft trajectories at various radial distances, longitudes and latitudes are required in order to obtain a good estimate of the most important Gauss coefficients.

The first three Gauss coefficients from $n = 1$ can be considered as three components of the magnetic dipole moment vector, one each along the X , Y and Z axes. The dipole magnetic moment is:

$$M_0 = \frac{4\pi a^3}{\mu_0} \sqrt{(g_1^0)^2 + (g_1^1)^2 + (h_1^1)^2} \quad (3)$$

where μ_0 is the magnetic permeability of vacuum. In addition, the colatitude of the magnetic pole can be expressed as:

$$\lambda_0 = \arccos \left(\frac{g_1^0}{\sqrt{(g_1^0)^2 + (g_1^1)^2 + (h_1^1)^2}} \right) \quad (4)$$

A particular property of intrinsic magnetic fields with large quadrupolar ($n = 2$) components is that the effective dipole is shifted vertically out of the equatorial plane by a distance of $z_0 = a(g_2^0)/(2g_1^0)$. This offset has been observed near the equator close to Saturn and it must be accounted for in modeling.

In order to calculate the longitudes used in equation (2) one needs an accurate rotation rate for the planet. The rotation rates of terrestrial planets can readily be obtained by tracking surface features as the planet rotates. By their very nature, the giant planets do not have any such observable solid surfaces and so other methods must be used to measure or infer the rotation rate of the interior. At Jupiter it was found that decametric radio emissions from the auroral regions were strongly modulated by the rotation of its tilted magnetic field and hence are strongly tied to the rotation rate of the deep interior of the planet [37]. Thus the periodicity of decametric radio emissions provides a measure of Jupiter's internal rotation rate. Saturn's kilometric radiation (SKR) was also observed to have a periodicity close to that of cloud features and it was suggested that this also represented the rotation rate of the deep interior [36]. The SKR period was used to construct a longitude system (*Seidelmann et al.* [158] and *Desch and Kaiser* [55]) based on the *Carr et al.* [36] period of $10^{\text{h}}39^{\text{m}}22.4^{\text{s}} \pm 7^{\text{s}}$.

The accuracy of this rotation period does not pose a problem for the modeling of internal fields from a single spacecraft pass over a few days, or several spacecraft passes separated by a few months. The longitudinal error, or smear, produced by this error only amounts to several tens of degrees. But when attempting to combine datasets covering periods of several years the error becomes unacceptably large. In such cases one must ignore the longitudinal dependence and seek solutions to a zonal model. In this approximation we integrate equation (2) over the azimuth angle (ϕ) and only derive fits for the g_n^0 coefficients, effectively forcing the magnetic energy in the observations into purely zonal ($m = 0$) coefficients and producing an axisymmetric magnetic field model.

Table 2 Gauss coefficients and internal field characteristics for zonal magnetic field models.

	Z ₃ [40]	P ₁₁ 84 [50]	SPV [51]	ZMP [21]	Cassini SOI [57]	Cassini Zonal
g_1^0 [nT]	21535	21140	21160	21431	21084	21162
g_2^0 [nT]	1642	1600	1560	2403	1544	1514
g_3^0 [nT]	2743	2260	2320	2173	2150	2283
M_0 [10^{34} A m ²]	4.714	4.628	4.632	4.691	4.615	4.633
z_0 [km]	2298	2280	2220	3379	2207	2156

Two studies have produced non-axisymmetric field models using Pioneer and Voyager observations. *Connerney et al.* [40] combined magnetometer data from Voyagers 1 and 2, the coefficients of which are presented in Table 2. *Giampieri and Dougherty* [68] took a different approach. The Pioneer and Voyager datasets were combined and fitted with a non-axisymmetric field model but the rotation rate (and hence the longitude for each sample) was left as a free parameter. They sys-

tematically varied the rotation rate to identify the rotation rate with the smallest RMS deviation between the model and the data. This analysis yielded a rotation period consistent with the radio measurements, but the error was reduced to ± 2.4 s from the ± 7 s obtained from SKR. Comparing the models of *Connerney et al.* [40] and *Giampieri and Dougherty* [68] in Table 3 one can see that the dipole moments agree to within about 1%, the northward offsets to within 20%, and the dipole tilts are all less than one degree. One can easily see that the dipole moments and northward offsets from the non-axisymmetric models are in approximate agreement with all of the axisymmetric (zonal) models developed from the Pioneer and Voyager data (see Table 2).

Dougherty et al. [57] fitted a zonal spherical harmonic model to the Cassini SOI magnetometer data, accounting for the external magnetospheric field with a simple symmetric disc model [67]. The results of their inversion are presented in the second column of Table 3 and show very similar values compared to the Pioneer and Voyager inversions. This suggests that no significant secular change occurred between the Pioneer/Voyager and Cassini SOI epochs.

The most recent work on Saturn's internal magnetic field uses all the Cassini data to date and hence covers a much wider period of time than previously published studies. The axisymmetric model is in good agreement with the existing models. To treat the rotation rate issue, four different fits were produced using four different longitude systems which are based on different estimates of the rotation rate. Two of these rotation rates are based on a constant period determined from an analysis of magnetometer data [69] and from a study of Saturn's gravity field [5]. The other two are variable period systems, designed to reflect the observations of a drift in the SKR period [116] and a drift in the period of magnetic fields in the inner and middle magnetospheres [9]. It was found that the use of these updated models greatly improve the residuals from the fit. The dipole moment, northward offset and the dipole tilt of $\sim 0.1^\circ$ are all in good agreement with Voyager and

Table 3 Gauss coefficients and internal field characteristics for non-axisymmetric magnetic field models.

	C ₈₂ [40]	GD ₀₄ [68]	B ₁ ^a	B ₂ ^b	B ₃ ^c	B ₄ ^d
g_1^0 [nT]	21439	21232	21171	21268	21278	21246
g_1^1 [nT]	-143	23	2	7	-41	-12
h_1^1 [nT]	143	60	-2	1	-43	-49
g_2^0 [nT]	1882	1563	1584	1585	1606	1492
g_2^1 [nT]	-515	-132	-37	-42	-70	-204
g_2^2 [nT]	500	5	-17	-17	37	57
h_2^1 [nT]	-433	51	111	-69	5	-27
h_2^2 [nT]	-36	-112	5	-14	16	-26
g_3^0 [nT]		2821	2240	2178	2245	2651
g_3^1 [nT]		-209	-72	-29	-205	269
g_3^2 [nT]		282	28	3	49	-296
g_3^3 [nT]		-156	5	0	22	-2
h_3^1 [nT]		1365	33	-42	52	-401
h_3^2 [nT]		-80	-75	29	-92	-99
h_3^3 [nT]		192	2	6	33	-67
RMS [%]		-	2.54	2.61	1.95	1.75
M_0 [10^{34} A m ²]	4.634	4.693	4.656	4.658	4.651	4.648
Dipole tilt [°]	0.5	0.2	0.008	0.02	0.2	0.1
z_0 [km]	2645	2218	2255	2246	2274	2116

^a used the rotation rate given in [69]; ^b used the rotation rate given in [5]; ^c used the rotation rate given in [116]; ^d used the rotation rate given in [9].

Pioneer models. The formal errors of the non-axisymmetric coefficients, as calculated from the inversion, are smaller than the coefficients themselves, suggesting that they are well-determined. However the significance of these terms is questionable given the uncertainties in the rotation period.

2.2 The Magnetodisk

Planetary magnetodisks are formed when significant ring current is present over an extended region, and the dipole field becomes too weak to maintain stress balance and the current system needs to intensify in order to balance the mechanical stresses.

At Jupiter and Saturn, internal plasma sources play a significant role in this process. At Jupiter the synchronous orbit is at $2.3R_J$, while at Saturn it is even closer to the planet at $1.8R_S$. The main magnetospheric plasma sources at Jupiter and Saturn are Io (orbiting at $5.9R_J$ and producing $\sim 10^3$ kg/s new plasma) and Enceladus (orbiting at $3.9R_S$ and producing $\sim 10^{2.5}$ kg/s new plasma). The centrifugal force acting on the newly produced plasma at Io and Enceladus exceeds the gravitational force by a large factor; therefore only magnetic forces can confine the plasma. If the equatorial quasi-dipolar field cannot maintain stress balance with the plasma stresses, the field will become more and more stretched. Most of the plasma is confined to the equatorial region due to the centrifugal forces; therefore the magnetic field lines will be more and more stretched near the rotational equator as more mass is added. This magnetically confined, centrifugally outward driven plasma and the corresponding highly stretched closed magnetic field lines form the magnetodisk. We note that pressure gradient and anisotropy forces can also generate a magnetodisk. Detailed discussion of these processes can be found for instance in [153, 194].

The dayside magnetic field configuration of the terrestrial and Jovian and Saturnian magnetospheres are radically different. On the dayside at Earth the field has a quasi-dipolar form, not that different from the dipolar field produced by a dynamo in Earth's interior. The rather modest distortion of this field away from a dipole is produced by the Chapman-Ferraro current at the dayside magnetopause and the azimuthal electric current called the ring current. In contrast, the dayside configuration in Jupiter's magnetosphere is highly distorted. The field is quasi-dipolar out to a distance of approximately 20 Jovian radii, beyond which the field stretches out into a disc-like configuration called the magnetodisc.

Voyager and Pioneer observations of Saturn's dayside magnetic field configuration revealed a quasi-dipolar magnetosphere not too dissimilar from the terrestrial magnetosphere [173, 41]. *Connerney et al.* [41] concluded that Saturn's magnetosphere did not possess a magnetodisc despite the magnetosphere rotating rapidly and having internal sources of plasma (all ingredients suspected of generating the magnetodisc at Jupiter).

Using Cassini observations *Arridge et al.* [12] examined magnetometer data from Saturn's dawn flank magnetosphere and found a field configuration similar to that on Jupiter's dawn flank. They suggested that this was actually Saturn's magnetodisc where the dayside quasi-dipolar configuration was a consequence of the smaller size of the magnetosphere and thus suppressed the disc on the dayside. In a later paper [13] they surveyed the magnetometer data to determine where this magnetodisc-like field

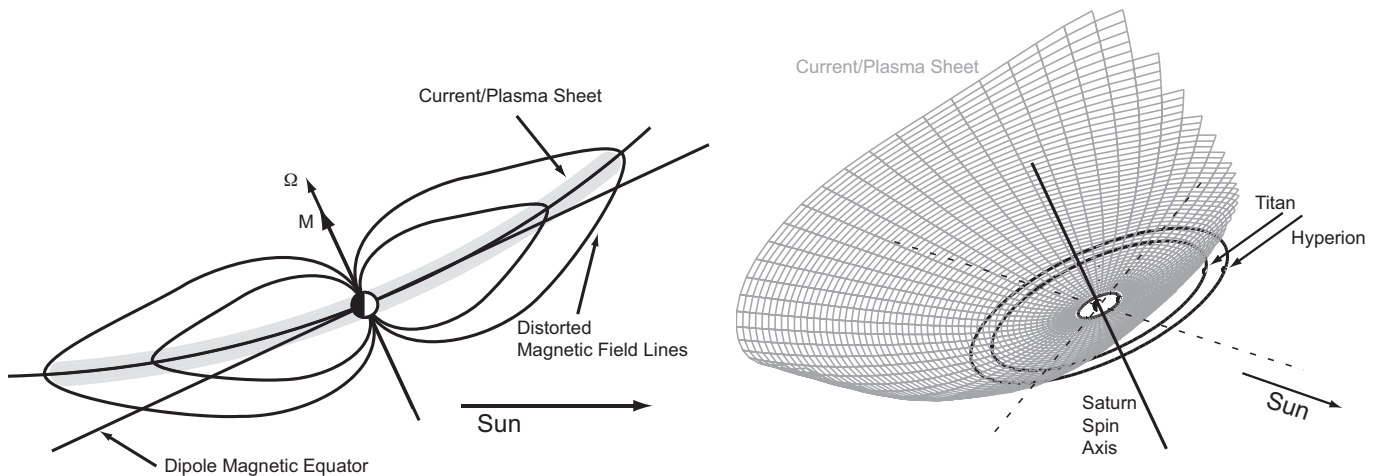


Fig. 6 Schematics illustrating the distortion of Saturn's magnetosphere. (left) The distorted plasma/current sheet and magnetic field lines in the noon-midnight meridian. (right) A three-dimensional view of this distortion and the resulting bowl-shaped current sheet. The orbits of Titan and Hyperion are included showing that they are underneath the sheet (from [14]).

configuration was observed. They found evidence for a magnetodisc not only on the nightside and dawn flanks where it was expected to exist, but also on the dayside.

The survey showed that the dayside magnetodisc only forms during intervals when the solar wind pressure is low and hence when the magnetosphere is expanded. Specifically, *Arridge et al.* [13] found that this highly stretched and distorted magnetic field configuration was only observed on the dayside when the subsolar standoff distance of the magnetopause was larger than $23R_S$. They noted that the dayside magnetosphere was compressed to less than $23R_S$ during all of the Pioneer 11 and Voyager dayside flybys, thus producing a quasi-dipolar dayside. The left panel of Fig. 6 illustrates this solar wind pressure-dependent distortion of Saturn's dayside magnetosphere.

The Voyager and Pioneer flybys occurred during near-equinox conditions and so were not well-placed to investigate seasonal magnetospheric effects. However, Cassini's arrival shortly after solstice provided an excellent opportunity. An unexpected seasonal effect, that has been first observed by Cassini [14], is illustrated in the right panel of Fig. 6. The dayside magnetospheric magnetic field and the plasma sheet surface are distorted so they lie to the north of the equatorial plane, i.e., completely the opposite of the behavior inferred at Jupiter. This northward warping was observed over the noon, dawn, and midnight sectors that were surveyed [14]. The dusk sector has yet to be examined for this effect. These observations led *Arridge et al.* [14] to describe the shape of the magnetosphere in terms of a bowl-shape, where the whole magnetosphere is bent above the equator beyond a characteristic distance called the hinging distance. The hinging distance was estimated to be between $15R_S$ and $30R_S$.

2.3 Empirical Magnetic Field Models

Planetary scientists frequently need quantitative description of the strength and the orientation of the magnetic field to understand the processes involved in magnetospheric and particle dynamics. As the spatial coverage of in situ magnetic field measurements in regions of interest is seldom complete, field models are constructed to provide the values of magnetic field globally. These models serve many purposes. For example, magnetic field models are frequently used in studies of single particle dynamics (drift and bounce of particles on stretched field lines, radial and pitch angle diffusion of particles in the magnetosphere, acceleration processes in the inner magnetosphere etc). The models also find application in understanding the magnetospheric reconnection geometry in the magnetotail to assess the location and frequency of magnetic substorms and storms in the magnetosphere. Another area where empirical models are vital is in field line mapping studies where ionospheric phenomena such as aurorae and satellite footprints need to be related to the source populations in the equatorial region of the magnetosphere.

Empirical models are constructed by specifying scalar, vector or Euler potentials in various regions of the magnetosphere. The models are constrained by ensuring that they satisfy fundamental conservation laws such as Maxwell's equations and stress balance in the form of a momentum equation. The first global model of Saturn's magnetosphere was constructed by *Maurice and Engle* [127] who followed the approach of *Beard* [20] where stress balance between the solar wind dynamic pressure and the magnetospheric magnetic field pressure determines the shape of the magnetopause. *Maurice and Engle* [127] used the GSFC Z3 model of the internal field [42] to prescribe the internal field of Saturn and the *Connerney et al.* [41] current sheet model to prescribe the contribution of the Saturnian plasma sheet. The field from the Saturnian magnetopause currents was first computed

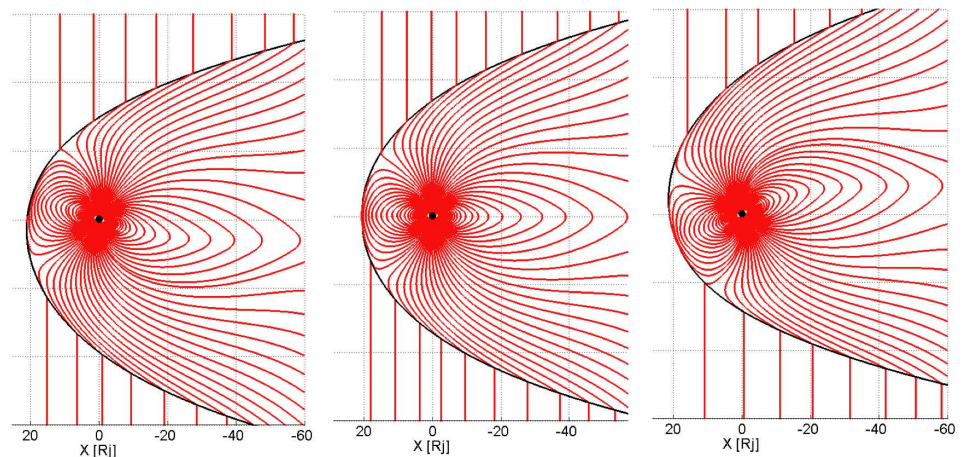


Fig. 7 Representative field lines from the latest field model of Saturn's magnetospheric field constructed from Voyager and Cassini data sets. Shown are field lines in the noon-midnight meridian for three situations of the dipole tilt -26° , 0° and 26° .

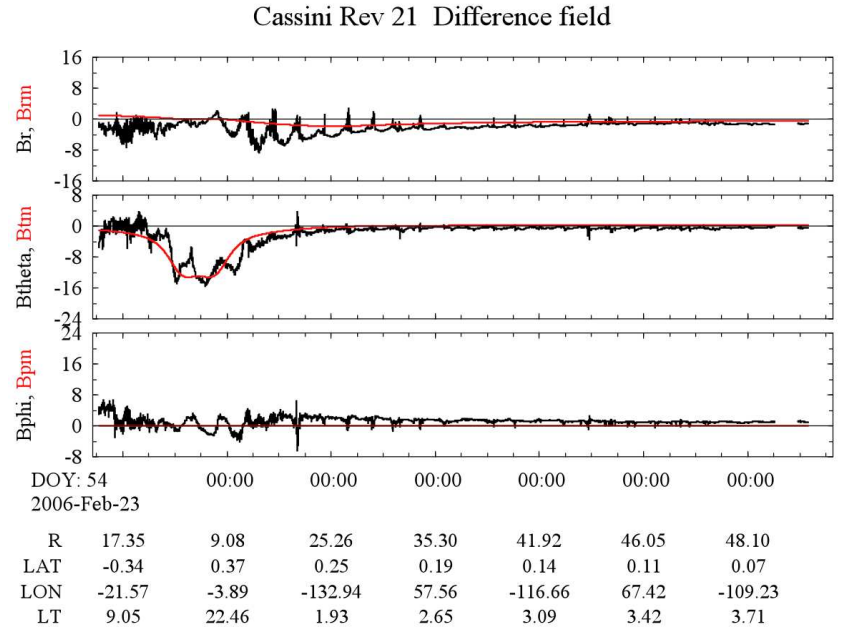


Fig. 8 The difference field from Rev 21 of Cassini (black traces) and the model field. The model predicts the average field quite accurately but does not explain the ten hour periodicity.

by constructing a wire frame model of the magnetopause current system and then using Biot-Savart integration. The computed field was next fitted to a spherical harmonic series for faster computation. Because of the choice of the harmonic series to express the field at the magnetopause (spherical rather than Cartesian or cylindrical harmonics which are better suited for currents arising from a paraboloidal surface), the *Maurice and Engle* [127] model is not applicable to the field of the stretched magnetotail. The model also lacks a magnetotail current system, does not include the hinging of the current sheet caused by the solar wind forcing and lacks bend-back of the field caused by corotation enforcement currents.

Recently, *Alexeev et al.* [4] have used the internal field model of *Dougherty et al.* [57] and the *Connerney et al.* [41] formulation of a thin current sheet with finite inner and outer boundaries to construct a new global magnetic field model. They confined the resulting field by a paraboloid magnetopause current. The model was fitted to data obtained from the SOI period. This model is more sophisticated and accurate than earlier models, but it still cannot account for the warping of the field resulting from the bowl shape of the current sheet, and it lacks radial currents that enforce corotation on the magnetospheric plasma.

New models of Saturn's magnetospheric field were constructed by using the general deformation technique successfully used by *Tsyganenko* [187, 188, 189] to model the Earth's magnetosphere. First, they constructed new modules to describe the ring current and the magnetotail fields. Next, they shielded the field interior to the magnetopause by using harmonic series to represent the magnetopause field. The model includes the bowl shape of the current sheet by using a description of a stretch deformation. The models (illustrated in Fig. 7) are based on data from Voyager and the first twenty five Cassini orbits. A comparison of the calculated field with observations shows a fairly good agreement (see Fig. 8) but also reveals systematic differences. The models, however, do not include the tilt of the current sheet (which produces spin periodicities in the data) and the sweep-back of the field lines.

Empirical magnetic field models have achieved a high level of sophistication. In spite of their limitations, they are a useful tool for investigating Saturn's complex magnetosphere. In combination with observations and numerical simulation they significantly contribute to our improving understanding of the Saturnian system.

3 Plasma Sources and Sinks

One of the fundamental questions of magnetospheric physics is the sources of the plasma that populates a magnetosphere. At Earth, many years of observational and theoretical work have demonstrated that there are two significant sources: the solar wind and the Earth's upper atmosphere. The mechanisms for entry and the relative importance of each source are still hotly debated, but there are no additional contenders of any significance. At Saturn, by contrast, there is a rich set of possible plasma sources: the solar wind, Saturn's ionosphere, Titan, the rings, and the icy satellites. One of the prime objectives of the Cassini mission was to assess the evidence for these various sources and their relative importance.

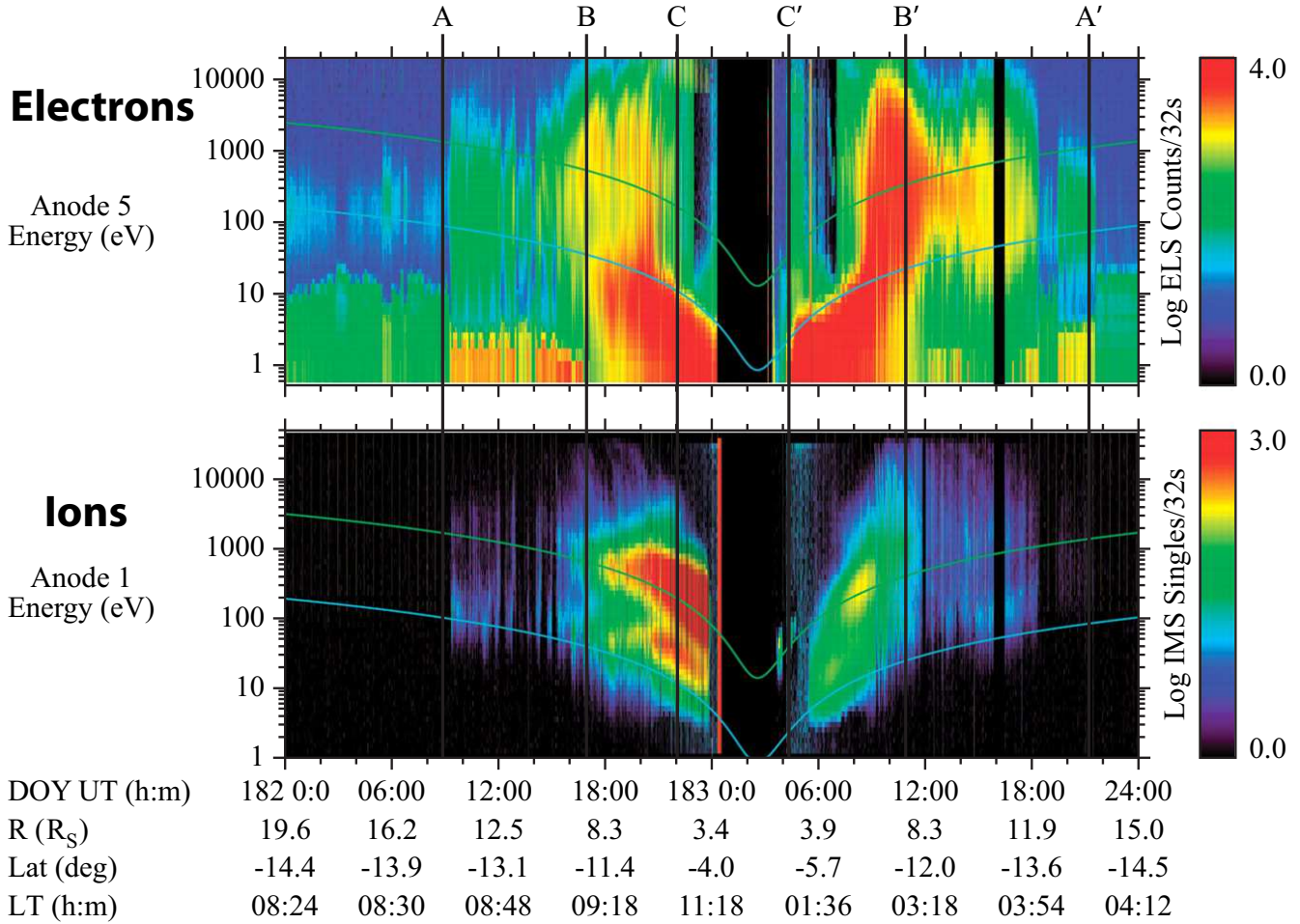


Fig. 9 Color-coded electron and ion count rates (proportional to energy flux) from the ELS (top) and the IMS/Singles (bottom), respectively, during Cassini's first pass through Saturn's magnetosphere (from [200]). The lower panel shows two dominant peaks in the E/q spectrum, corresponding to co-moving populations of H^+ and W^+ ions. The curved lines superimposed on the plots give the energy corresponding to the full corotation velocity for O^+ (upper curves in both panels) and H^+ (lower curves).

Fig. 9 shows two energy-time spectrograms from the Cassini Plasma Spectrometer (CAPS) of the energy flux of the thermal electrons (top panel) and the thermal ions (bottom panel) during orbit insertion (SOI). The lower panel shows two dominant peaks in the E/q spectrum, corresponding to co-moving populations of H^+ and W^+ ions (defined as a combination of O^+ , OH^+ , H_2O^+ , and H_3O^+). There is a clear inward gradient in the ion composition beginning near $9 R_S$ inbound and $8 R_S$ outbound, where the ratio of the water group ions to the hydrogen ions increases substantially [200]. The region between $L \sim 5$ and $L \sim 9$ is sometimes called the inner plasmasphere [167, 200].

Fig. 10 shows the CAPS plasma parameters for the inbound portion of SOI [167]. Within the inner magnetosphere the speed of the plasma increases (panel 3 of Fig. 10) to near corotation, and there is a sharp increase in the densities inside $L \sim 9$ (panel 1 of Fig. 10). *Young et al.* [200] and *Rymer et al.* [154] confirm the Voyager observations [166] that there are two electron populations in the inner plasma source region (5 to $9 R_S$) (panel 4 of Fig. 10). The density ratio of the cold electrons (< 20 keV) to the hot electrons (> 100 keV) is more than one order of magnitude throughout most of this region [200]. The energy-time spectrogram in the upper panel of Fig. 9 shows that the energy of the cold electrons approximately tracks the proton corotation energy [200]. The average energy of the hot electron component (100 eV to > 10 keV) increases with decreasing L value, consistent with the near-adiabatic inward transport [154]. The hot electrons drop out inside $L \sim 5$, due to collisions with the neutrals in Saturn's neutral cloud or losses to the E-ring [154, 200].

There are a number of observational clues to the origin of a plasma population: the spatial distribution, the mass composition, the energy distribution, and the angular distribution. However, telltale signatures of origin can be modified or obscured by physical processes such as collisions with neutral material (gas and dust). At Saturn there is strong evidence that neutral material significantly interacts with the magnetospheric plasma, so we need to view the plasma as not completely collisionless. In addition,

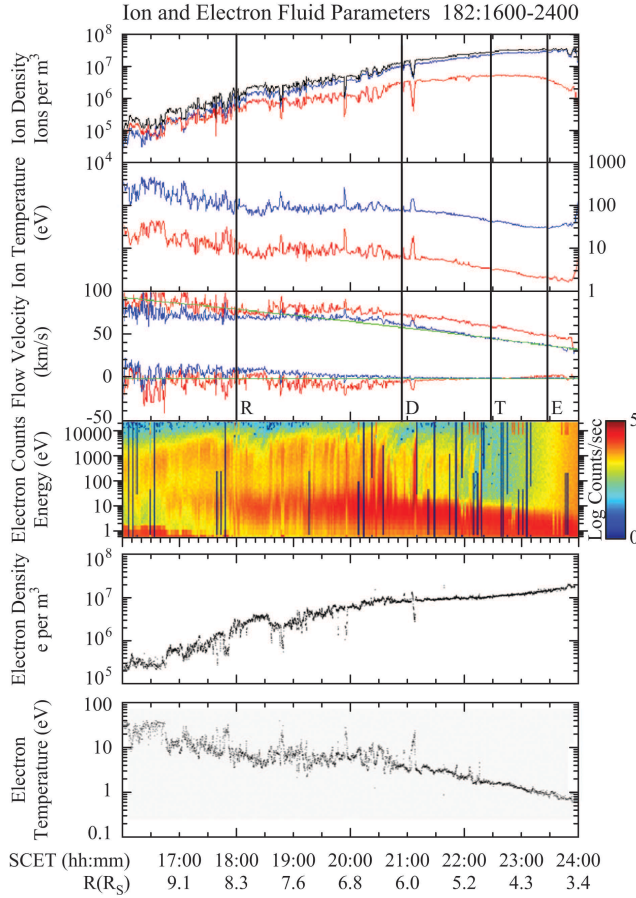


Fig. 10 An overview of the plasma parameters during Cassini orbit insertion on June 30, 2004: CAPS ion fluid parameters (top three panels) for protons (red) and water group ions (blue), electron energy spectrogram (panel 4), and electron densities (panel 5) and electron temperatures (panel 6) derived from CAPS/ELS using a Maxwellian fit to flux versus energy below 100 eV. Vertical lines mark the times when Cassini crossed the L-shells of Rhea, Dione, Tethys and Enceladus (from [167]).

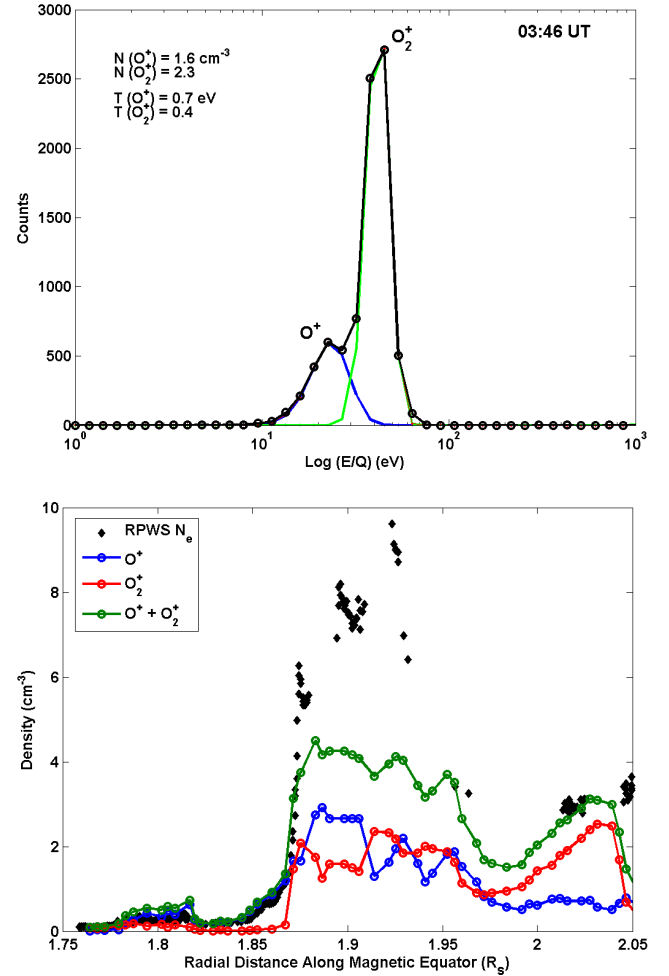


Fig. 11 Top: CAPS/IMS observations of O^+ and O_2^+ over the main rings during SOI. The corotation flow velocity was assumed. Bottom: Derived O^+ and O_2^+ densities over the main rings, compared with the RPWS-derived electron density (from [183]).

when molecular species are involved, as they are at Saturn, chemistry (e.g., gas-phase chemistry, photodissociation, etc.) can also introduce complications, and these effects need to be borne in mind when assessing the evidence for various sources.

Magnetospheric plasma primarily originates from a complex region in the inner magnetosphere where plasma is in constant motion, continually being created from sources in the atmosphere/ionosphere of the rings, the inner icy satellites, even the planet itself. Inside $L = 10$, there are plasma boundaries characterized by changes in the ion composition and in the bulk plasma properties. The most prominent ion components in Saturn's inner magnetosphere are the hydrogen ions (H^+) and the water group ions (W^+) [111, 167, 200].

We now consider Cassini evidence regarding the relative importance of the various plasma sources.

3.1 Rings ($< 3R_S$)

Deep inside the inner plasma source region, ion measurements by INMS [196] and CAPS [200] and high electron densities measured by the RPWS [79] revealed the existence of a tenuous plasma layer in the vicinity of Saturn's main rings. The electron density varies spatially in this region by more than an order of magnitude, and the electron temperature is only a few eV [195]. The RPWS electron densities reach a peak of $> 100 \text{ cm}^{-3}$ near the outer edge of the A ring and then decrease rapidly inside $2.2 R_S$ [79]. At the same time, the electron parameters derived from the Langmuir probe show an order-of-magnitude drop in

the electron temperature that strongly correlates with the order-of-magnitude electron density increase observed by RPWS [195]. *Wahlund et al.* [195] propose that the low plasma densities observed inside $2.2 R_S$ [79] are the result of absorption of the plasma by the ring particles and invoke the density increase inside the Cassini Division where ring particles have a lower density as a supporting argument. *Gurnett et al.* [79] suggest that the deep electron density minimum (0.03 cm^{-3}) at $1.7 R_S$ occurs because this is the location of synchronous orbit. Over the rings, *Moncuquet et al.* [134] found that the cold electron temperature is $\sim 1.5 \text{ eV}$ over the G-ring at $2.8 R_S$, dropping to $\sim 0.5 \text{ eV}$ at $\sim 0.5 R_S$ when Cassini passes through the ring plane.

The ion composition of the tenuous plasma layer located directly over the A and B rings consists of O^+ and O_2^+ [183, 196, 200]. The temperatures of these heavy ions drop to a minimum near synchronous orbit ($\sim 0.5 \text{ eV}$ for O^+ and $\sim 0.1 \text{ eV}$ for O_2^+) and increase with increasing radial distance from Saturn [184]. Significant O_2^+ is also detected outside the main rings near the F ring [184]. There is a sharp increase in the ion and electron densities at $\sim 1.85 R_S$ with the ion densities peaking at $\sim 4 \text{ cm}^{-3}$ over the B-ring [184]. Fig. 11, from [183], shows enhanced ion fluxes consistent with the presence of O^+ and O_2^+ , likely produced by UV photosputtering of the icy rings, with subsequent photoionization of the O_2 . This process has been modeled by *Johnson et al.* [96], who also showed that scattering and dissociation can populate the magnetosphere with O_2^+ beyond the main rings.

Beyond the A ring, photo-sputtering is supplemented, indeed dominated, by charged-particle sputtering by the magnetospheric plasma. While sputtering can produce ions directly, the most likely outcome of an ion striking an icy surface is the liberation of neutral water molecules, with a small fraction of dissociation products (e.g., O_2^+ , H_2^+). At one time, sputtering from icy satellites and E-ring particles was thought to be the source of the extended neutral atmosphere of water molecules and their dissociation products observed by the Hubble Space Telescope (e.g., [161]) and by Cassini (e.g., [60]). Ionization of this material, by solar photons or by electron impact is indeed the primary source of plasma in Saturn's magnetosphere. However, calculations of the sputter flux gave rates significantly too low to account for the observed neutral cloud (e.g., [162, 100]). Recently, *Johnson et al.* [98] have recalculated sputtering rates on ice grains and icy satellites, using plasma ion properties derived from Cassini CAPS observations [168, 169, 170]. While they still find sputtering to be a small contribution to the total neutral gas supply rate compared to the supply attributed to the gas and ice plumes observed to be emanating from Enceladus' southern polar region, it nonetheless has a significant effect on the lifetime of the small E-ring grains.

3.2 Icy Satellites ($3R_S$ to $6R_S$)

The overwhelming evidence from Cassini observations is that the plasma of the inner magnetosphere was actually produced by local ionization of gases liberated from the icy satellites and the rings, with the rings determined to be of lesser importance as discussed above. As previously seen by the Voyager spacecraft (e.g., [144]), Cassini has found inner magnetospheric plasma to

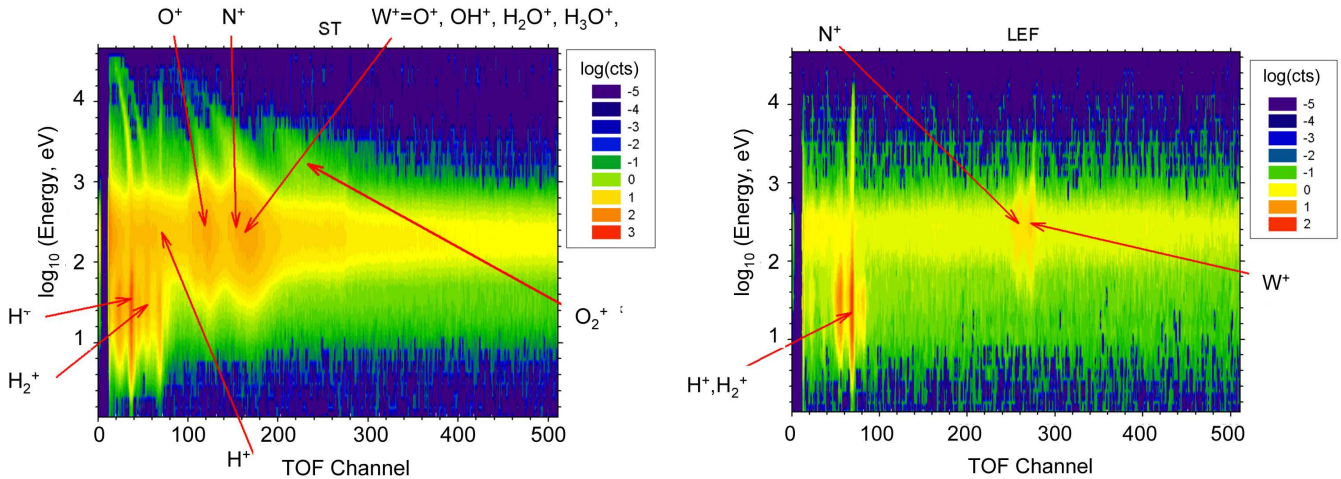


Fig. 12 Plasma ion composition measurements from the CAPS/IMS during the inbound portion of Cassini's SOI (from [167]). The counts are binned by energy/charge and time-of-flight and summed over the six-hour interval from 1800 – 2400 UT on 30 June 2004. Particles with a given m/q occupy distinct curves in E/q vs TOF space, and the identities of various species are indicated on the plots. The left panel shows measurements from the more sensitive straight-through (ST) detector, and the right panel shows the corresponding measurements from the linear-electric-field (LEF) section, which has lower sensitivity but higher resolution. The bands of counts that extend across the full TOF range are due to accidental coincidences caused mostly by penetrating radiation.

consist of two dominant ion components: H^+ and water-group ions (e.g., [200]). Fig. 9, from [200], shows that the energy-per-charge distribution of the bulk plasma exhibits two distinct peaks, corresponding to nearly corotational flow of H^+ and W^+ .

Fig. 12, from [167], shows definitive evidence from the CAPS IMS instrument that the heavier component is indeed W^+ . Fig. 12 was obtained by summing observations over six hours covering the radial range from 3.4 to 8.3 R_S . The left panel shows counts as a function of E/q and time-of-flight as recorded by the ST element of the IMS, and the right panel shows the corresponding measurements from the higher-mass-resolution LEF. In this representation, particular ion species should occupy specific locations, as indicated by the various labels. Noteworthy aspects of the figure include: 1) an energy-dependent background that extends across the entire range of time-of-flight, which is caused by accidental coincidences, especially with penetrating radiation; 2) the signatures of H^+ and H_2^+ extending from a few eV to several 10's of keV; 3) two peaks attributable to W^+ (in the left panel: that labeled “water groups neutrals” and that labeled “ O^- Peak,” the latter referring to oxygen from water group ions that enter the instrument with a positive charge, but emerges from the foil with a negative charge), extending from 10's of eV to > 10 keV; 4) a significant population of N^+ clearly distinguished from the O^+ peak in the LEF (right panel); and 5) evidence for molecular O_2^+ .

3.2.1 Enceladus

The dominant compositional signature illustrated in Fig. 12 (H^+ , H_2^+ , and W^+) points directly to water ice on rings and satellites as the primary source. This evidence is consistent with the conclusion that the primary source of plasma is ionization of the cloud of neutral water-group molecules observed through remote sensing measurements (e.g., [161]), a conclusion reached previously on the basis of Voyager observations (e.g., [147]).

The puzzle mentioned above as to the source of so much neutral gas, peaking near the orbit of Enceladus, was solved in 2005. Observations from a close Cassini flyby revealed the surprising fact that Enceladus is actively venting gas and ice grains [58, 83, 142, 180, 197]).

The primary gas emitted is water vapor, potentially accounting for the observed vast cloud of water vapor and water products. Johnson *et al.* [96] have modeled the distribution of neutrals emitted from the vents and found that the emitted gas should form only a narrow, nearly uniform torus centered on Enceladus' orbit. However, when they included the effects of subsequent charge-exchange and reactive collisions with ambient corotating plasma, they found a much more extended neutral cloud, very similar to that determined from HST observations. These secondary interactions with the original narrow torus molecules also explain the large population of H_3O^+ ions that peak near Enceladus' orbit [184, 170] since H_3O^+ is only formed in reactive collisions (e.g., $H_2O^+ + H_2O \rightarrow H_3O^+ + OH$) at low speeds (e.g., [74, 96]).

Using *in-situ* Cassini observations the total mass production from Enceladus was first estimated to be $> 10^2$ kg/s [184]. This mass addition rate was consistent with values deduced from earlier HST observations [101]. UVIS observations and a more detailed analysis of the *in-situ* measurements yielded a total plasma production rate of ~ 300 kg/s [83, 96]. While this production rate is somewhat variable, most observations are consistent with it.

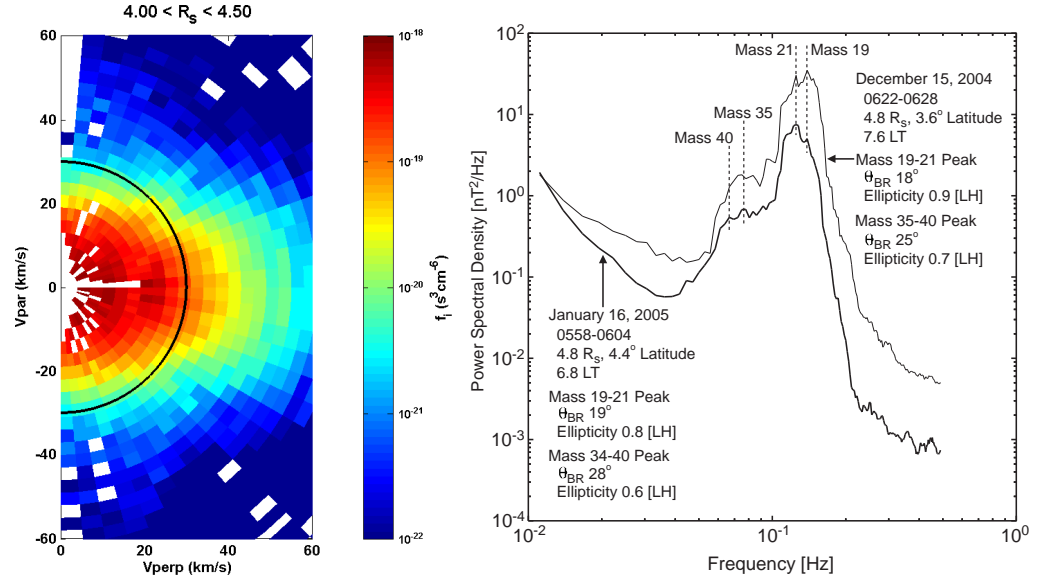
3.2.2 H^+ and W^+

While the core ion population is dominated by < 100 eV water group ions in the inner magnetosphere, CAPS detected a second non-thermal water group ion component from the vicinity of the Enceladus orbit out to about the Tethys orbit [185]. CAPS measurements of phase space velocity distributions of the water group ions in this region show the distinctive signature of pick-up ions, produced locally by local ionization and by charge-exchange collisions between the thermal water group ions and the water group neutral atoms and molecules.

Ionization of neutral atoms or molecules in the presence of a flowing plasma creates a telltale ring-type ion velocity-space distribution (for a detailed discussion of this process we refer to a later Chapter of this book [126]). Such so-called “pick-up” ion distributions are shown in the left panel of Fig. 13. Additional evidence for the pick-up of fresh ions in this region comes from observations of electromagnetic ion cyclotron (EMIC) waves by the Cassini MAG [120]. Such waves, illustrated in the right panel of Fig. 13, are produced by a plasma instability driven by the ring-type velocity distributions and typically have frequencies near the gyrofrequency of the picked-up ions. The density of the non-thermal pick-up ions (see [126]) is estimated to be $\sim 8\%$ of the thermal water group ion population [185].

Sittler *et al.* [168] note that the pick-up process is consistent with the observed correlation between the ion temperatures and the bulk flow speed and is likely to be the dominant energy source for the plasma in this region. As noted by Sittler *et al.* [168], the CAPS observations during SOI show that both the H^+ and W^+ temperatures have similar positive radial gradients, consistent with pick-up ion energization in a plasma whose near-corotational flow speed increases linearly with r (panel 3 of Fig. 10). The

Fig. 13 Observational evidence for ion pick-up near the orbit of Enceladus. Left: The phase space density of W^+ ions as a function of v_\perp and v_\parallel in the frame of the bulk flow, showing the clear ring-type distribution at $(v_\perp, v_\parallel) \sim (25, 0)$ km/s, superimposed on the bulk plasma centered at $(0, 0)$ (from [185]). Right: Magnetic field fluctuation spectra showing distinct peaks in spectral power near the gyrofrequency of W^+ and a heavier ion). Such waves are produced by an electromagnetic ion-cyclotron instability driven by an ion ring such as that shown in the left panel (from [120]).



temperature of the hydrogen ions increases steadily from ~ 2 eV just outside $3.4R_S$ to ~ 10 eV just outside $8R_S$. The water group temperature also increases steadily from ~ 40 eV to ~ 100 eV over the same radial distance [167]. The thermal electron temperature (panel 6 in Fig. 10) tracks the hydrogen ion temperature [154, 167] and is found to vary as L^2 [140, 168] over this radial distance. Electron temperatures derived from RPWS Langmuir probe measurements are qualitatively similar to, but lower than, the CAPS temperatures [195].

The near equality of the electron and proton temperatures has been attributed to collisional heating of the electrons [154]. However, it has been argued that Coulomb collisional heating can account for the observed electron energies outside $\sim 5R_S$, but the local heating and cooling effects seen near the E-ring and the orbit of Enceladus are probably due to cooling by dust particles in the E-ring or by the concentration of water neutrals in the vicinity of Enceladus.

The hotter electrons (> 100 eV) visible in Fig. 9 have their source in the middle or outer magnetosphere and are transported to the inner magnetosphere by interchange-like injections of hot plasma, disappearing inside $L \sim 6$ [154] (see section 5.1).

3.2.3 N^+

While the N^+ evident in Fig. 12 could in principle indicate a Titan source, the radial dependence of the N^+ phase space density and the energy of this population point to an inner magnetosphere source [174, 175]. This is illustrated in Fig. 14, which shows the

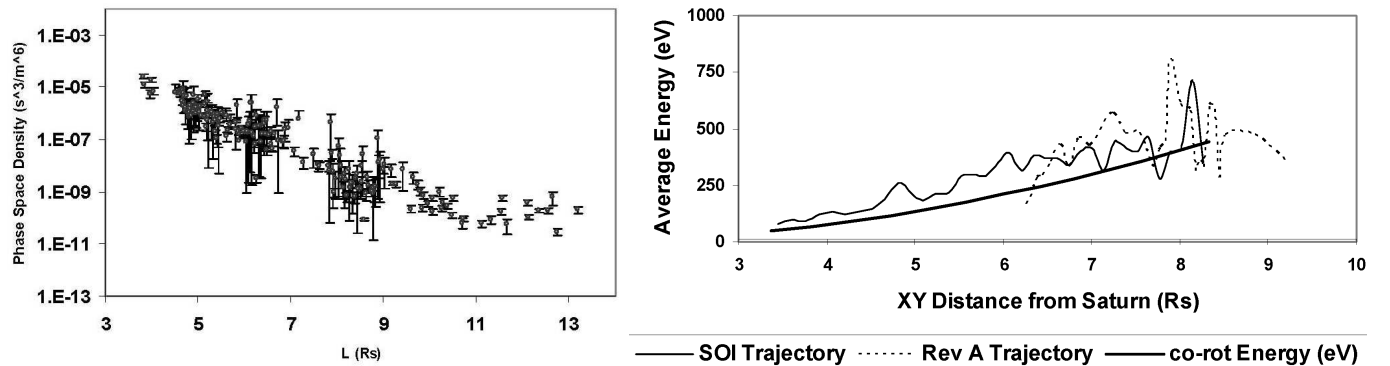


Fig. 14 Left panel: Nitrogen ion phase space density in the inner magnetosphere derived from CAPS/IMS time-of-flight measurements within $0.25 R_S$ of Saturn's equatorial plane (from [175]). The negative radial gradient strongly suggests a source in the inner magnetosphere. Right panel: Average energy of the nitrogen ions on two passes through the inner magnetosphere (from [174]). The heavy solid curve is the energy of a nitrogen ion exactly corotating with the planet.

phase space density derived by *Smith et al.* [175] as a function of radial distance (left panel) and the corresponding profile of the average energy of the population determined by *Smith et al.* [174] (right panel). The inward gradient of the phase space density clearly indicates that the source is in the inner magnetosphere. There is a peak at $L \sim 4$, near the orbital radius of Enceladus, but no measurements inside Enceladus' orbit were available due to penetrating radiation background. The average energy of the N^+ population (panel b) is consistent with pick-up in the local corotational electric field (solid line), and it is inconsistent with transport from a Titan source, which would be expected to produce an adiabatic energy increase with decreasing r . *Smith et al.* [175] also found a peak in the ratio of N^+/W^+ phase space densities in the narrow Enceladus torus region [96] near the orbital distance of that moon. Based on a comparison with simulations, they concluded that Enceladus is the principal source of N^+ in the inner magnetosphere. A more detailed subsequent analysis [176] sought to identify the source molecules for the observed N^+ : N_2^+ , consistent with INMS observations of mass 28 molecules near Enceladus [196]; or NH_3^+ , which would have potentially important implications for the physical properties of the ice on Enceladus. This study found definitive evidence for NH_4^+ , presumably from NH_3 , comprising a few percent of the inner magnetospheric heavy ions. While no similarly definitive evidence for N_2^+ was found, a best fit to CAPS data included small amounts of N_2^+ , with upper limits near the INMS fraction, leading to the conclusion that both molecular nitrogen and ammonia are emitted from Enceladus. One possible local source might be the ionization of NH_3 from the surface ice of Saturn's inner satellites [54].

3.3 Minor Sources

Titan has definitely been found to be a source of magnetospheric plasma, picked up from its upper atmosphere (e.g., [111]), but surprisingly little nitrogen, which is the signature ion for a Titan source, has been found in the outer magnetosphere (e.g., [200, 174, 175]). Cassini has thus found no real evidence for the Titan-sourced nitrogen plasma plumes inferred from Voyager observations [61, 62]). This lack of nitrogen is likely attributable to the inability of flux tubes at Titan's orbital distance to execute complete drift orbits around Saturn, such that Titan-originating plasma cannot build up to substantial densities (e.g., [200, 175]). Whatever the reason, there is no evidence in the inner magnetosphere for significant amounts of plasma of Titan origin.

The solar wind likewise does not appear to be a dominant source of plasma for Saturn's inner magnetosphere, although there is some evidence for solar wind entry into the outer magnetosphere via magnetopause reconnection (e.g., [128]), as well as for the existence of open polar cap magnetic flux, which implies the existence of a Dungey-like reconnection-driven circulation that delivers solar wind plasma to the outer magnetosphere (e.g., [48, 16, 114] and see Section 4). There is as yet, however, no definitive assessment of the relative importance of solar-wind-driven transport in populating the outer magnetosphere. With respect to the inner magnetosphere, it appears that the solar wind is at best responsible for the hot, tenuous material that accompanies low-content magnetic flux tubes in exchange for filled ones containing colder inner-magnetospheric plasma (see Section 1.3). And even for that hot, tenuous population, there is some compositional evidence that much of it may have originated in the inner magnetosphere as well (e.g., [167, 111, 159]).

While the icy satellite and Enceladus sources of plasma are quite significant in the inner and outer magnetosphere, Saturn's ionosphere may also play a role through the polar wind. The polar wind refers to the supersonic outflow of particles along open magnetic field lines at high latitude. While the Saturnian polar wind has not been observed yet, *Glocer et al.* [71] carried out model calculations and predicted that Saturn's high latitude ionospheres might add a few kg/s of H^+ , H_2^+ and H_3^+ ions to the magnetosphere. While this process is only a minor plasma source for Saturn's magnetosphere, the polar wind ions might serve as important tracers to better understand the magnetospheric configuration and dynamics.

3.4 Loss Processes

To maintain an approximate steady state of the magnetospheric plasma population, the production of plasma by these various sources must be balanced by roughly equivalent losses. Candidate loss processes include recombination, loss to the atmosphere through pitch-angle scattering, absorption by neutral material (satellites and ring particles), and radial transport.

The recombination timescale depends on the ion species, the electron density, and the electron temperature. As noted by *Sittler et al.* [170], recombination is much slower for atomic ions (O^+ , H^+) than for molecular ions (e.g., H_2O^+ , OH^+ , H_3O^+). *Sittler et al.* [170] have estimated the effective recombination timescale for the inner magnetospheric plasma by taking a composition-weighted average of the timescale for each relevant species (H^+ , O^+ , OH^+ , H_2O^+ , H_3O^+). The relative composition of the various species was determined from CAPS time-of-flight measurements [200, 170]. The calculated recombination lifetime is $\sim 4 \times 10^5$ s inside of $L \sim 5$ and climbs rapidly outside of that distance.

By contrast, the timescale for radial transport is large at low and small at high L values. Using a form of the radial diffusion coefficient derived for Io by *Siscoe and Summers* [165], *Richardson* [147] found the radial transport time to be $\sim 5 \times 10^5$ s at $L=6$, decreasing as L^{-3} beyond that. If $L \sim 6$ marks the onset of the interchange instability (see [126]), radial diffusion must decrease substantially inward of that location, resulting in very long transport times inside the orbit of Dione. This break in transport properties is consistent with the flattening of the radial profiles of the electron phase space densities beyond $L \sim 6-8$ [154].

Evidence for plasma losses due to precipitation is indirect and primarily stems from the observations of EMIC waves (e.g., [120]; see Fig. 13). The minimum lifetime τ_{SD} for particles pitch-angle scattering in these waves is given by the strong diffusion limit (e.g., [104]):

$$\frac{1}{\tau_{SD}} = \frac{\Omega_B}{\pi} (1 - \cos \alpha_L) \quad (5)$$

where Ω_B is the particle bounce period and α_L is the equatorial loss cone angle. Taking the characteristic particle speed to be the pick-up velocity,

$$v = LR_S \Omega_S \quad (6)$$

where Ω_S is Saturn's rotational angular speed, Eq. (5) gives $\tau_{SD} \sim 2.7 \times 10^6$ s at $L=4$, increasing as L^3 beyond that. Thus, in spite of the robust activity of the EMIC instability, precipitation is not likely to be a significant factor in the loss of inner magnetosphere ions.

The last potential loss mechanism is absorption by E-ring material. For low-energy particles whose range in ring material is less than the average grain size, the lifetime against loss by grain impact is [181]:

$$\tau_{absorp} = \frac{T_B}{2\eta} \cos \alpha_{eq} \quad (7)$$

where η = optical opacity of the ring ($\eta = Nd\pi r_0^2$), N = number of ring particles per unit volume, d = ring thickness, r_0 = ring particle radius and α_{eq} = equatorial pitch angle.

From *Showalter et al.* [163], the peak optical depth of the E-ring is at the orbit of Enceladus, where the geometric cross-section per unit area, i.e., the optical opacity, is $5.3 \pm 1.3 \times 10^{-5}$. Again taking $v = LR_S \Omega_S$ as the characteristic ion speed, for an equatorial pitch angle of 80° , the lifetime against absorption is 3.7×10^7 s, much longer than other loss timescales.

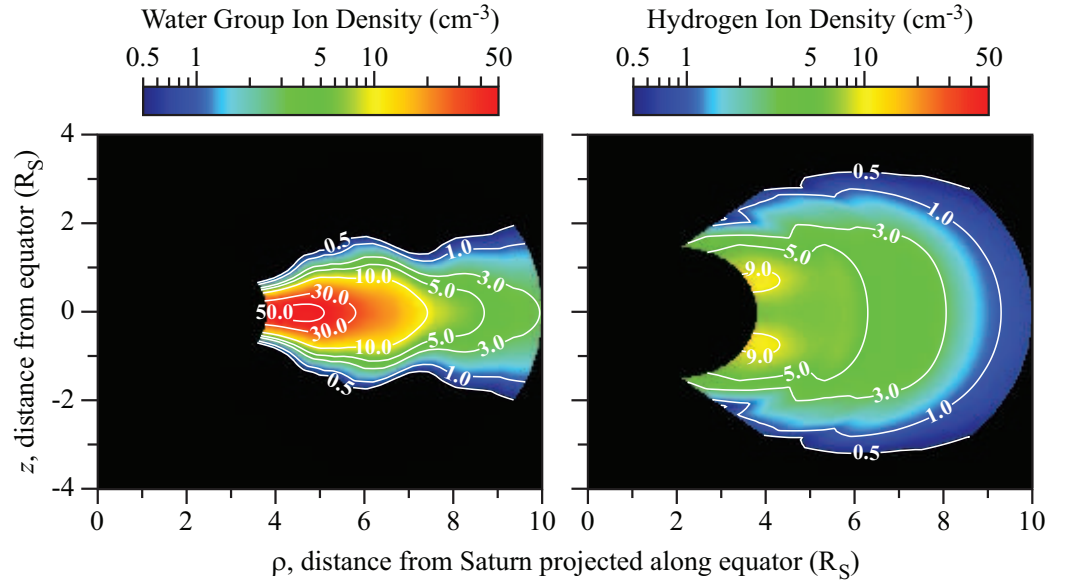
In summary, estimation of lifetimes against various plasma loss mechanisms shows that inside of $L \sim 5-6$ recombination is likely to be the most important loss process, whereas beyond $L \sim 6$, rapid radial transport dominates. In particular, the operation of the interchange instability (c.f. Section 5.1 and [126]) beyond the peak flux-tube content at $L \sim 6$ very efficiently removes plasma produced in the inner magnetosphere, delivering it well into the plasma sheet of the outer magnetosphere. Indeed, the cool water-group plasma originating in ionization of the near-Saturn neutral cloud extends to the dayside magnetopause and well down the tail (e.g., [129, 128]).

3.5 Plasma Density Models

The first density models describing the distribution of electrons and ions in Saturn's magnetosphere were developed using in situ plasma measurements from the Pioneer 11 and Voyagers 1 and 2 spacecraft, along with remote sensing observations from the Hubble Space Telescope [145, 146, 148, 149]. Several density models have been developed to take advantage of the wealth of in situ plasma and plasma wave measurements obtained during years of Cassini orbits around Saturn. Using plasma wave measurements of the upper hybrid resonance emission band for several of the early equatorial passes, *Persoon et al.* [138] showed that the plasma diffuses radially outward from Saturn and the equatorial electron density varies inversely with increasing radial distance as $R^{-3.7}$. When sufficient high-latitude electron densities became available, *Persoon et al.* [139] developed a simple scale height model, based on a dominant centrifugal force acting on the plasma. The scale height model identifies the heavy ion component of the plasma inside $L=10$ and shows that the equatorial density of this ion component varies as $L^{-4.1}$ and the plasma scale height varies as $L^{1.8}$ [139].

Sittler et al. [170] used the CAPS ion and electron fluid parameters as boundary conditions and solved the full set of first-order differential equations which give the balance of forces acting on the plasma along Saturn's dipole field lines inside $L=10$. The resulting 2D density contour plots show the strong equatorial confinement of the heavy water group ions and a butterfly distribution of the proton density, indicating that the protons peak off the equatorial plane due to the strong influence of the ambipolar electric field acting on the light ions.

Fig. 15 Contour plots of the ion densities in the plasma source region where z is the distance above/below the equatorial plane and ρ is the perpendicular distance from Saturn's spin axis. The density contours are constructed from the comparison of the diffusive equilibrium model to measured electron densities from the RPWS instrument, assuming symmetry about the spin axis and mirror symmetry about the equator (from [140]).



Persoon et al. [140] derived a simplified analytic solution to the same field-aligned force balance equation and developed a diffusive equilibrium model for a two-species plasma. The analytical model was compared to the RPWS electron density measurements for latitudes up to 35° . The fit of the diffusive equilibrium model to the measured densities yields the ion equatorial densities and scale heights for both dominant ion species, which are used to construct ion density contour plots in the meridian plane. Fig. 15 shows the density contour plots for the water group ions (left panel) and the hydrogen ions (right panel) derived from the fit of the diffusive equilibrium model to the measured RPWS densities. The contour plot for the water group ions clearly shows that these ions are strongly confined to the equatorial plane at all L -values. The contour plot for the hydrogen ions (right panel) shows that the density of the lighter ions peaks off the equator at low L -values under the influence of a strong ambipolar force. However, the growing strength of the mirror force acts to cancel the ambipolar effect at larger L -values.

4 Magnetospheric Regions

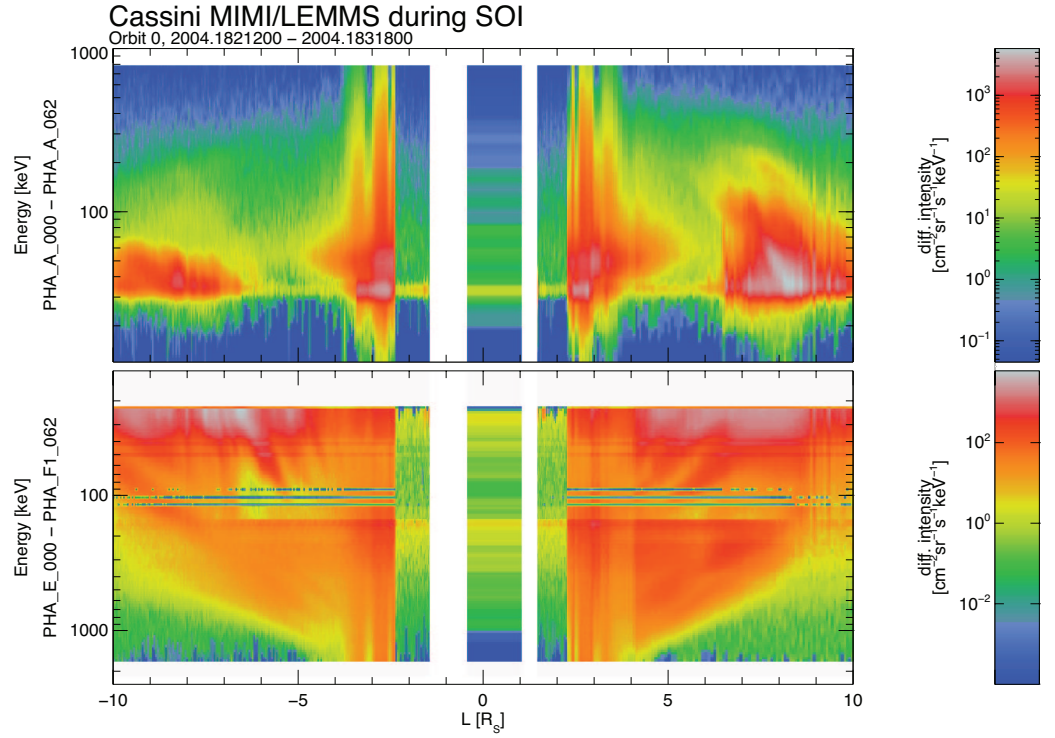
4.1 Trapped Radiation

Our knowledge about Saturn's radiation belts before Cassini is based on the in-situ particles and fields measurements of the flyby missions Pioneer 11, Voyager 1, and 2 summarized in [192]. The charged particles of the radiation belts in the Saturnian magnetosphere with energies of hundreds of keV to tens of MeV can be found mainly inside $6 R_S$. Typical charged particle intensities measured in the middle and inner magnetosphere as a function of dipole L are shown in Fig. 16.

The top panel shows energetic ions and the bottom panel energetic electrons measured by the MIMI/LEMMS experiment aboard Cassini during SOI around Saturn in July 2004. Energetic ions are abundant in the middle magnetosphere ($L > 7 - 8$) but between $3.5 - 7 R_S$ they are absent, because of charge-exchange processes between these hot ions and the cold neutral gas that transforms these populations into hot energetic neutral atoms and cold ions. Energetic (< 100 keV) electron fluxes also drop inside $7 R_S$ with respect to the values in the middle magnetosphere, but in the region where energetic ions are not present, hot electrons are much more abundant. Inside $3.5 R_S$ energetic particles in the range of $100 - 200$ keV appear (typical for radiation belts), while MeV particles are also present. In the center of each panel ($L < 2.3$), a plasma void region is seen, where energetic particles have been depleted by Saturn's main rings. In both panels, ion and electron intensities show dispersed features as a function of energy. These are called "injections" and are thought to be the result of instabilities occurring between the middle and outer magnetosphere (where hot plasma is present) and the inner magnetosphere (where energetic ions are absent and hot electrons are less abundant) [125]. Those injection events play a major role in magnetospheric particle transport [35]. At this point the relation between the injection events and the interchange process is unclear.

The radiation belts are to some extent transient, given the continuous depletion of energetic particles by the icy moons, the rings and the neutral gas that are present in that region. All charged particles pass through the orbital plane of Saturn's moons

Fig. 16 Dynamic spectrograms (energy versus L) of energetic ion (top panel) and electron intensities (bottom panel) inside of $10 R_S$ for Cassini's Saturn insertion orbit in July 2004 measured with the MIMI/LEMMS instrument aboard Cassini. Electron energy is plotted increasing downward for comparison with the features in the ion population. The radiation belt outside the main rings ($L > 2.3$) is transitioning to an extended, highly dynamic plasma sheet outward to the magnetopause. (modified from [111])



and rings while executing one of the fundamental motions of trapped radiation: the bounce motion along the magnetic field lines. Unlike at other planets, even equatorial particles are continuously absorbed by an extended ring system and by a number of moons with almost circular and equatorial orbits within the radiation belts. As a consequence, losses of particles to the icy moon surfaces and ring particles are expected to be higher compared to the losses in other planetary magnetospheres. *Carbary et al.* [32] give a good summary of the Voyager 1 and 2 findings. Among the important results were the calculation of the diffusion coefficient D_{LL} at the distance of Dione and the evaluation of various magnetic field models. *Van Allen et al.* [190] extracted D_{LL} values from a Mimas absorption signature and suggested that a filtering effect to radially diffusing electrons is taking place at Enceladus that results in a monoenergetic electron spectrum in the innermost Saturnian radiation belts.

The variability of the absorption signatures has been extensively studied by *Roussos et al.* [151] using Cassini energetic particle data. Inside $2.3 R_S$, and in the regions magnetically connected to the main rings, energetic particles are completely absent. Many of Saturn's moons are continuously immersed in the planet's radiation belts and are exposed to its trapped energetic particle population. The energetic particles are absorbed by the moons forming evacuated regions within the magnetosphere, the lifetime of which depends on the effectiveness of particle diffusion processes (and most importantly, radial diffusion) (see also [126, 35]). In addition these absorption regions continuously drift in the magnetosphere. Monitoring the properties of the depleted flux tubes (depth, shape, magnetospheric coordinates, longitudinal separation from the absorbing moon), provide important information about the dynamics of the magnetosphere or even the absorbing object. The absorption regions are classified in two main categories: macrosignatures and microsignatures [190]. Macrosignatures are the permanent and azimuthally averaged decreases of the count rates in the radial distribution of energetic particles. Microsignatures are count rate decreases that are strongly dependent on the longitudinal distance between the signature's location and the absorbing body. Satellites, rings or dust concentrations can be the source of both macrosignatures and microsignatures. Fig. 17 gives an example of ion macrosignatures in the radiation belts of Saturn [150] caused by the moons Janus, Mimas, Enceladus, Tethys, and Dione. The depletion in the intensity of 10 MeV protons is seen in all latitudes and local times as a function of L . Those macrosignatures in ion fluxes with $E > 10$ MeV are not initially sharp or deep, as for energetic electrons. A large percentage of such ions can escape absorption by the icy moons due to gyration and bounce motion; however, these shallow absorption regions reencounter the moon before diffusion processes have any significant effect on them and therefore they become deeper, until an equilibrium is reached between ion diffusion and ion depletion (near steady-state situation). In the Cassini data from 2004 – 2007 it is observed that for all moons this equilibrium is not reached: the ion depletion is almost 100% around the moon orbits. This means that ion absorption rates are always faster than diffusion. For this reason, no ions of $E > 10$ MeV exist along the L -shells of the moons Janus, Epimetheus, Mimas, Enceladus, Tethys and Dione. At these locations, ions are absent in almost all magnetospheric local times and latitudes, independently of each moon's location.

Fig. 17 Ion macrosignatures as a function of L-shell and local time (top) and latitude (bottom). The color denotes the ion differential intensities of the Cassini MIMI/LEMMS P7 channel, that detects ions with energy greater than about 10 MeV/nucleon. The macrosignature locations show an excellent correlation with the L-shells of the moons Janus, Epimetheus, Mimas and Enceladus. Data shown correspond to the period July 2004-July 2007 and are averaged every 86 s (from [150]).

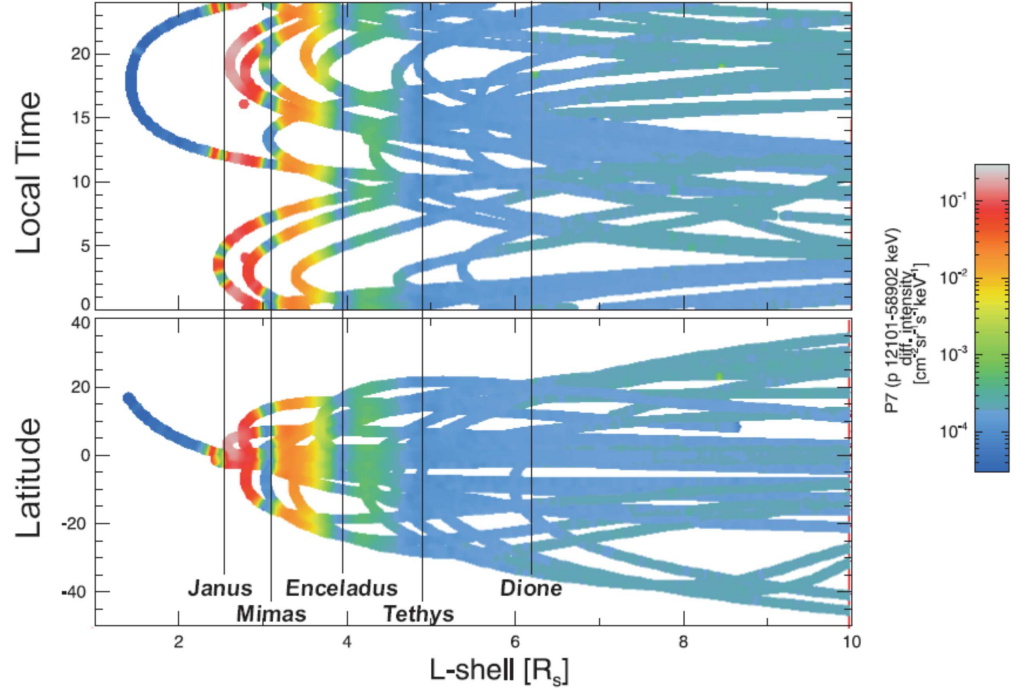


Fig. 18 shows two examples of many microsignatures observed in MIMI/LEMMS data on Cassini, recorded on day 229 in 2006 in electron intensities in the inner magnetosphere caused by the moons Dione (at 03:51-03:55 UT) and Helene at around 03:58 UT [152]. These microsignatures are only seconds to minutes long. From the depth and the shape of the signature as a function of longitude difference between the object and the observer it can be determined what object caused the depletion on one hand and on the other hand diffusion processes responsible for the refilling can be studied.

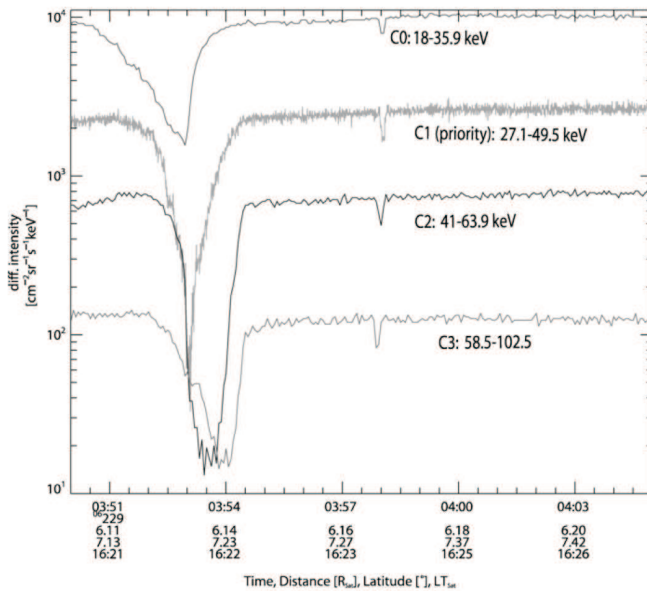


Fig. 18 Microsignatures of the Saturnian moons Dione (03:5103:55 UT) and Helene (03:58 UT) in energetic electron intensities (channels C0–C3 of the MIMI/LEMMS instrument onboard the Cassini spacecraft) measured on day 229 in 2006 (from [152]).

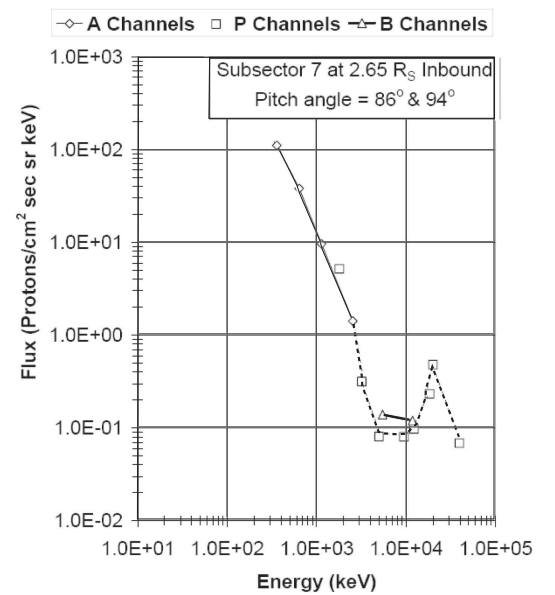


Fig. 19 Proton energy spectrum of Saturn's radiation belts measured with the three different sets of energy channels (A, P, and B) of the MIMI/LEMMS instrument aboard Cassini in July 2004 at 2.65 R_s (from [10]).

A representative energy spectrum of trapped energetic protons at $2.65 R_S$ and at nearly perpendicular pitch angle during the inbound portion of the first Cassini orbit around Saturn in July 2004 is shown in Fig. 19. Besides a power-law energy dependence of the spectrum, a prominent secondary peak in the energy spectrum is observed around 20 MeV. The agreement among 3 different sensor arrangements (A, P and B-channels) of the MIMI/LEMMS instrument with measured values of particle flux and energy shows that systematic errors of measurement are probably no greater than 10%. This secondary peak confirms the Voyager observations by *Krimigis and Armstrong* [106]. The two-component energy spectrum of protons can be interpreted with two different source populations: the lower energy protons originate in the solar wind or inside the magnetosphere by violating the adiabatic invariants and the secondary peak most probably originates from Cosmic Ray Albedo Neutron Decay (CRAND) described by *Cooper et al.* [43, 44].

Saturn's radiation belts have been modeled by *Santos-Costa* [156]. This three-dimensional model shows that absorption by dust plays the major role in the innermost part ($1 - 2.3 R_S$), while local losses from interactions with satellites are more important in the $2.3 - 6 R_S$ region, consistent with observations by the Pioneer and Voyager spacecraft and by Cassini as described above.

The uniqueness of the first Cassini orbit that provided data very close to the planet inside and above the innermost D-ring led to the discovery of a new trapped particle population. The discovery of this new radiation belt inside the D-ring (see Fig. 20) was only possible because the spacecraft was inside the main radiation belts. Only therefore the energetic neutral atoms (ENAs) originating from the new radiation belt (via charge-exchange processes) that normally interact with ions in the main belts could be measured with MIMI/INCA [111].

The ENA-emitting region inward of the innermost D ring (Fig. 20) is explainable by double charge-exchange processes where planet-directed ENAs from the main radiation belt are stripped of electrons when they enter Saturn's exosphere and are trapped as ions which will subsequently undergo another charge-exchange collision with exospheric neutral atoms and thus be transformed back into ENAs. This process of stripping and charge exchange may be repeated many times, but some of these particles will eventually escape the exosphere as ENAs. Thus, this double (or multiple) charge-exchange process forms a low-altitude ENA emission region inside the D-ring. A similar trapped radiation belt was identified and explained by charge exchange in Earth's radiation belts by in situ measurements at low altitudes [135]. The first direct measurements of the particle population inside the D-ring will be possible when Cassini will traverse multiple times through that region on polar orbits during the final phase of its mission.

Energetic particles (tens to thousands of keV) are found throughout the plasma source region, but the intensity is found to vary with radial distance and is often correlated with the orbits of the inner satellites. *Krimigis et al.* [111] observed a depletion in the more-energetic ions between the L-shells of Dione and Enceladus, indicating energetic particle loss through charge-exchange with neutral gas in this region [60]. Just outside the orbit of Rhea ($8.7 R_S$), there is a rapid increase in the energy of both the energetic ion and the non-thermal electron populations [111].

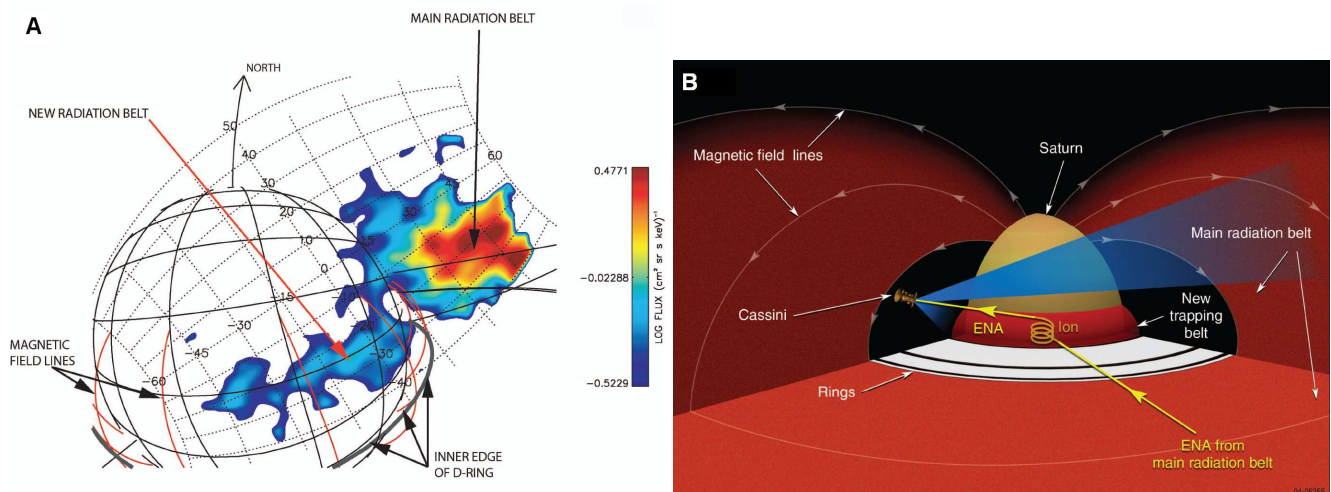


Fig. 20 (A) INCA image in 20 to 50 keV/nuc ENAs. The bright region above Saturn's limb is caused by ENAs produced by charge-exchange collisions between main radiation belt ions and near equatorial gas distributions. The band of emission above the equator is produced by the same ENAs from the main belt being stripped in Saturn's exosphere between the inner edge of the D ring and the cloud tops, trapped there temporarily as energetic ions, and then reemitted as ENAs. (B) Schematics of the charge exchange/stripping process that begins as ENA emission from the main belt and produces ENA emission from Saturn's exosphere (from [111]).

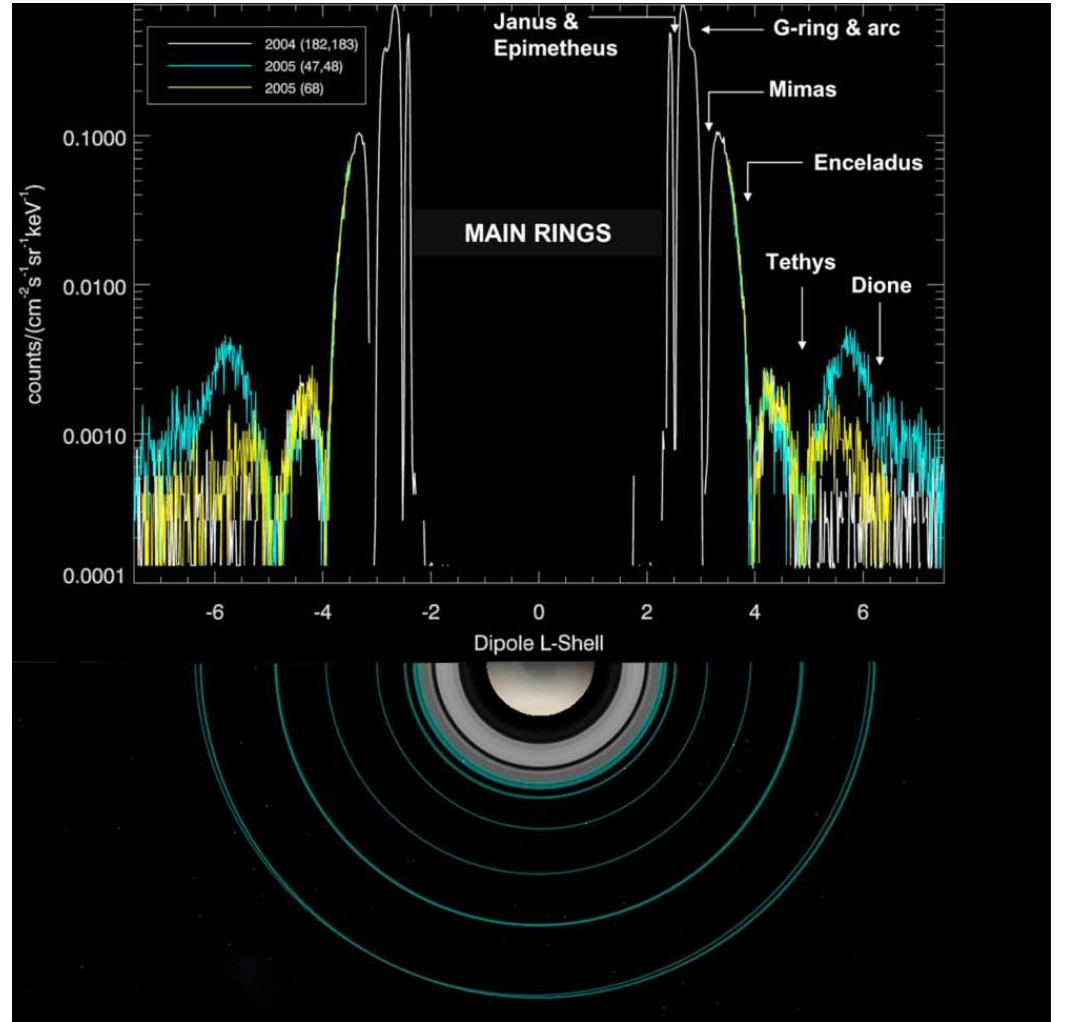


Fig. 21 MeV ion fluxes in the innermost magnetosphere. Differential ion fluxes from the ion channel P2 of LEMMS (2.28 – 4.49 MeV/nuc) are plotted as a function of the dipole L-shell. Negative (positive) L denotes the inbound (outbound) part of the orbit (from [151]).

The variability of the radiation belts in response to solar wind disturbances has been recently demonstrated by *Roussos et al.* [151] who analyzed Cassini MIMI/LEMMS data. Fig. 21 shows MeV fluxes in the inner magnetosphere. Profiles are plotted for three different periapsis passes. The 2004 profile (white curve) is the most common, identified in 27 out of the 36 orbits considered in this study. Flux peaks are clearly separated at several icy satellite L-shells, as indicated. A dropout is also seen at the G-ring L-shell. The lowest background is measured above the main rings that absorb all magnetospheric energetic ions, while Saturn’s volume and the strong dipole field “shadow” the instrument from penetrating, galactic cosmic rays. Note that fluxes do not reach background at the depletion region of Janus and Epimetheus, meaning that some flux can be transported across their shared orbit. The two profiles of 2005 (yellow and turquoise curves), that correspond to an orbit with a periapsis at $L = 3.5$, reveal a flux enhancement centered close to Dione’s L-shell (Dione belt). The enhancement is isolated only outside Tethys’s L-shell. Similar enhancements are seen in all LEMMS channels between 30 keV/nuc and 10 MeV/nuc. In this study a whole series of Cassini orbits through the main radiation belts have been studied. It has been recognized that for some of the periapsis passes MeV ion fluxes increased in a region between the orbit of the moons Dione and Tethys (shown as blue curves in Fig. 21). Those increases correlate very well with interplanetary disturbances arriving at Saturn. After a few weeks or months the so called “Dione belt” increases disappear and the “normal” radiation belt fluxes were registered again (white and yellow curves in Fig. 21). It is therefore assumed that this increase is due to interaction processes between the particles in the interplanetary medium and the magnetosphere. However, inside the orbit of Tethys no change or increase could be detected during those events, from which the authors concluded that the source population of the innermost radiation belts must be different. The most probable source of those particles is the CRAND process as mentioned above.

4.2 Ring Current

The combination of gradient and curvature drifts in a non-uniform magnetic field generates a ring current that opposes the background field (c.f. [76]). The concept of an electrical current encircling the Earth at high altitudes was first proposed in the early 1900s to explain the depression of the horizontal component of the Earth's magnetic field during geomagnetic storms. Away from Earth, ring currents of a different nature and size were observed at Jupiter and Saturn. In the latter case, a ring current was inferred from magnetic field measurements during the Voyager 1 and 2 flybys [41] and confirmed from particle measurements made by the Low Energy Charged Particle (LECP) and plasma (PLS) instruments [107, 108, 124, 130].

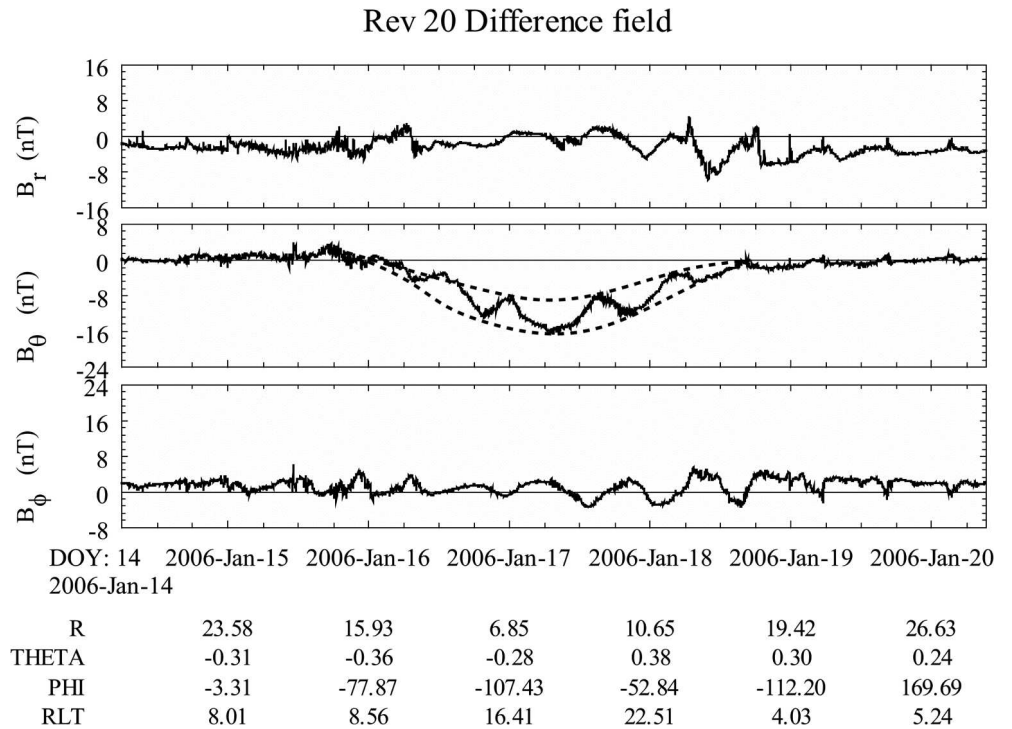
At Saturn, the field generated by the ring current is northward and depresses the strength of the planetary field locally where the plasma energy maximizes. The total current observed flowing through the ring current region is estimated to be between 8 and 17 MA [41, 27]. As the field generated by a ring current is roughly uniform inside the ring, the field remains depressed even inside the ring current region. Fig. 22 (reproduced from *Khurana et al.* [105]) shows the perturbation field (observed – internal field) measured in the magnetosphere during Rev 20 in a spherical coordinate system. The perturbation field in the B_θ component is northward (negative B_θ) inside of $\sim 12R_S$ which is a manifestation of the ring current plasma. Detailed modeling shows that a ring current starting at a radial distance of $\sim 6R_S$ and peaking near the radial distance of $10R_S$ is required to correctly model this perturbation field.

The inner edge of the ring current lies between 6 and $8R_S$ but the outer edge of the ring current is strongly controlled by the magnetopause location on the dayside and lies anywhere between 12 and $22R_S$. In addition, the strength of the ring current is also directly related to the magnetospheric size. The lowest values of the ring current strength (8 MA) are observed when the dayside magnetopause is near its minimum location ($\sim 19R_S$) whereas the strongest currents (17 MA) are observed when the dayside magnetopause is located near $31R_S$.

Bunce et al. [27] used the *Connerney et al.* [41] model to examine the variation of the model ring current parameters with the subsolar magnetopause distance. In this work the thickness of the current sheet was fixed at $2.5R_S$. For each pass of Cassini through the dayside, the residual (observed – model internal field) magnetic field vectors were fitted by eye to the model. The location of the last inbound magnetopause crossing and the magnetopause model of *Arridge et al.* [11] were used to establish the subsolar magnetopause distance for that pass. Using their sets of ring current parameters, they also calculated Saturn's total magnetic moment (dipole + ring current) and axial ring current field (essentially Saturn's Dst).

As the total magnetic flux from the planet is conserved, the field is enhanced elsewhere, namely in regions above and below the ring current (called the lobe regions) both locally and in the distant magnetosphere. The effect of the ring current on the field can be visualized as a physical pulling out of the planetary field lines from the inner low-latitude magnetosphere into the high

Fig. 22 The external field in Saturn's magnetosphere ($B_{\text{dif}} = B_{\text{obs}} - B_{\text{int}}$) observed during Rev. 20. The depression in the B_θ component near the planet ($r < 14R_S$) arises mainly from the ring current. The perturbation field in this component can be seen to oscillate by a factor of 2. Two envelopes (dashed lines) representing the minimum (upper envelope) and the maximum value (lower envelope) of the ring current field have been drawn to aid the eye (from [105]).



latitude regions of the magnetosphere. The percent reduction of field strength from this “field diversion” is quite modest in the ring current regions of planets ($< 10\%$ in Saturn’s inner magnetosphere) because of the strong dipolar field close to the planet. However, in the outermost parts of the magnetosphere, the ring current and its extension – the current sheet – can make the lobe field many times stronger than that expected from a dipole field.

Fig. 22 also contains evidence for the presence of an azimuthal asymmetry of the ring current visible as a rotational modulation of the B_θ component. The azimuthally symmetric part of the ring current produces a depression of ~ 8 nT near the closest approach (see the upper envelope indicated by a dashed curve in Fig. 22), whereas the asymmetric part increases the depression by another ~ 8 nT (the lower envelope). A survey of such data from Cassini reveals that the ring current region anomalies are always present in the magnetic field observations obtained from the inner/middle magnetosphere. They have a period close to that of the planetary rotation and show a systematic phase relationship with the azimuthal (B_θ) and radial (B_ρ) component of the field (see Fig. 33) which has been shown by *Gurnett et al.* [80], *Southwood and Kivelson* [179] and *Andrews et al.* [9] and to have a period identical to that of the SKR intensity. The asymmetric ring current amplitude is seen to vary from orbit to orbit over a range of 25 – 200% of the value of the symmetric ring current. The field and plasma data clearly establish that the energetic particle azimuthal anomalies and their associated partial ring current are a semi permanent feature of Saturn’s magnetosphere.

Together with its clear presence in the in-situ particle and magnetic field measurements, the energetic particle contribution to the asymmetric Saturnian ring current is visible through the energetic neutral atom (ENA) images that the MIMI/INCA sensor obtained, once Cassini switched to high latitude orbits in July 2006 [112]. Briefly, the ENA technique relies on charge exchange between trapped ions and a residual neutral gas that results in fast atoms escaping the system and being sensed as if they were photons. ENA images offer a complete picture of the instantaneous energetic particle distribution, for almost every region of interest within the magnetosphere. The ENA distribution provides direct information on the dynamical features of the energetic part of the ring current, which cannot possibly be revealed through the in-situ measurements from individual equatorial passes of the spacecraft. One such image is shown in Fig. 23. The ring current maximum intensity is generally outside the orbit of Rhea; observable intensities may extend beyond the orbit of Titan. Overall, the image in Fig. 23 illustrates that although this interval was chosen specifically as an example with minimal local time/ longitudinal structure, the ring current, unsurprisingly, is not the uniform, symmetric construct postulated in early modeling of Saturn’s magnetic field.

The ring current geometry does not resemble the neatly-modeled, symmetrical current sheet extending from ~ 8 to $\sim 15 R_S$ that fit the magnetic field data from the limited Voyager and Pioneer 11 coverage [39]. Both in-situ measurements and ENA images have shown that the ring current can at times be highly variable, possibly dominated by a series of injections [125], with strong longitudinal asymmetries that corotate nearly rigidly with the planet, contrary to the Earth’s ring current, where no rotational modulation is seen and initial asymmetries are primarily organized by local time effects. One such injection event is shown in Fig. 24 [112], a sequence of six INCA images covering a Saturn rotation. The top left panel shows a large, factor of 10, intensity increase between dawn and local midnight that moves anticlockwise through dawn, then day side, then local evening (middle right panel), then local midnight, and then returns to its original location some 11^h later (bottom right panel).

Since the Pioneer/Voyager epoch, the field due to Saturn’s ring current has been modeled using a simple azimuthal symmetric disc model, originally developed to model the Jovian magnetodisc ([41] and references therein). The current density in this model

Fig. 23 ENA image of the ring current as viewed from above the northern hemisphere. This image, in the range 20 – 50 keV, was obtained on 19 March 2007, with MIMI/INCA, at a latitude of 54.5° and radial distance $24.5 R_S$. Saturn is at the center, and the dotted circles represent the orbits of Rhea and Titan. The Z axis points parallel to Saturn’s spin axis, the X axis points roughly sunward in the Sun-spin-axis plane, and the Y axis completes the system, pointing roughly toward dusk. The INCA field of view is marked by the white line and accounts for the cut-off of the image on the left. (from [112]).

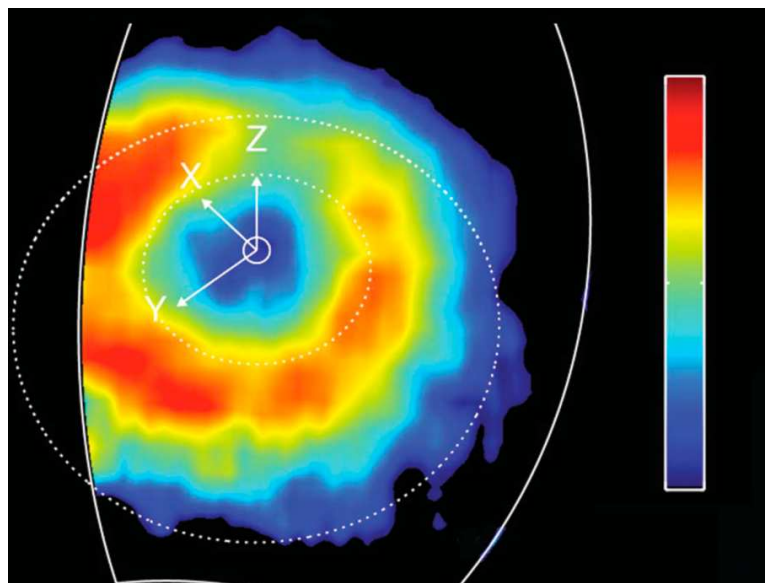
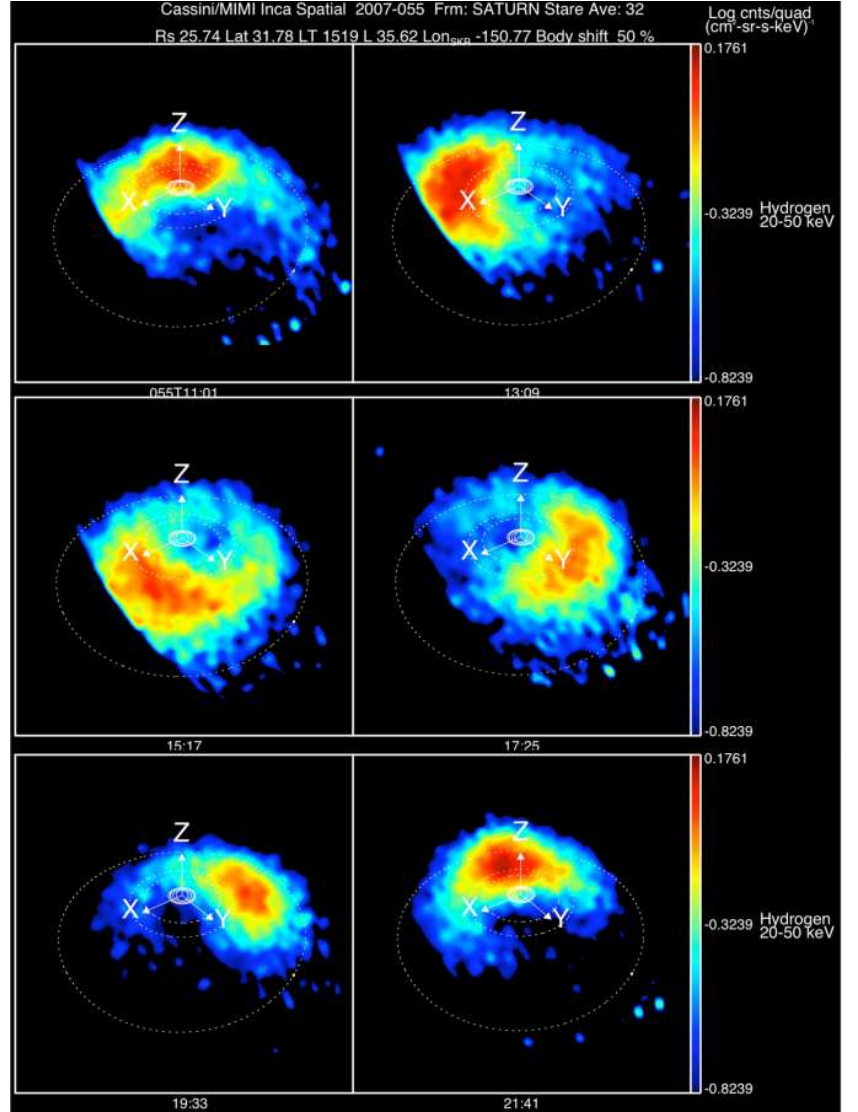


Fig. 24 Sequence of six ENA images in neutral hydrogen, taken by INCA in the range 20 – 50 keV on February 24, 2007, covering a full Saturn rotation. Cassini was located at 32° latitude and $26 R_S$ from Saturn at local time 15:12. Saturn is at the center, the X axis is pointing approximately in the solar direction, Y is pointing towards dusk, and Z is pointing along Saturn's spin vector. Dotted lines show the orbits of Dione, Rhea, and Titan in proper perspective. The images are spaced at roughly 2^h intervals (from [112]).



is zero in the region outside of the inner and outer edges, and outside of $z \pm D$ (where D is the sheet half-thickness). Inside this region the current density is uniform in z and has a $1/r$ radial dependence. This particular radial dependence was chosen for reasons of mathematical convenience and has been criticized by studies that compare the magnetic stresses measured in situ in Saturn's magnetosphere [124] and theoretical stress balance calculations [193]. *Beard and Gast* [21] developed a ring current model which had a more flexible current density profile, and compared more favorably to that measured from Voyager data by *Mauk et al.* [124]. Nevertheless, the model produces reasonably good fits to the magnetometer data and has been also applied to Cassini magnetometer data. *Arridge et al.* [13] showed that fits of the *Connerney et al.* [41] model in the outer magnetosphere could be radically improved by considering the bowl-shaped hinging of the current sheet.

Fig. 25 presents these results as a function of subsolar magnetopause standoff distance. With the exception of the inner edge, each parameter increases with system size - principally due to the increase in the outer edge of the ring current. *Bunce et al.* [27] showed that the ring current region occurs on a fixed band of field lines and therefore expands and contracts as the magnetopause position varies. The ring current region therefore maps to a fixed co-latitude range in the ionosphere ($14^\circ - 20^\circ$ N, $16^\circ - 22^\circ$ S). This lies just equatorward of the observed southern hemisphere aurora, indicating that the aurora are not associated with the mass-loading processes occurring inside the ring current region, but with processes in the outermost layers of the magnetosphere [28]. This finding is in approximate agreement with the considerations of *Arridge et al.* [12] who qualitatively observed that the magnetodisc appeared to extend right to the magnetopause.

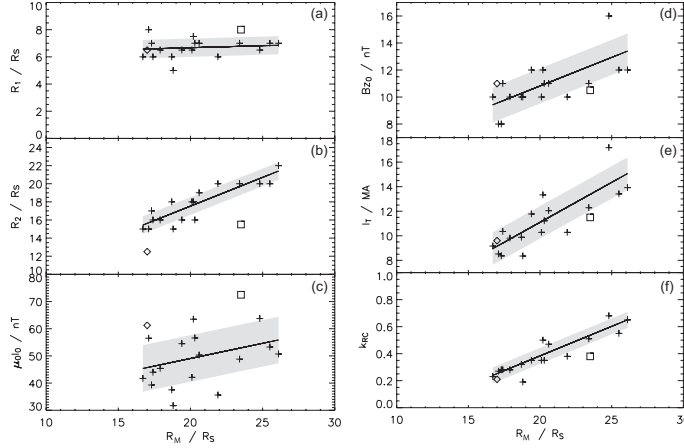


Fig. 25 Fitted ring current parameters as a function of subsolar magnetopause standoff distance. Panels (left-a) inner edge, (left-b) outer edge, (left-c) intensity, (right-a) axial (Dst) field, (right-b) total current, (right-c) ratio between the ring current and dipole magnetic moments. (from [27]).

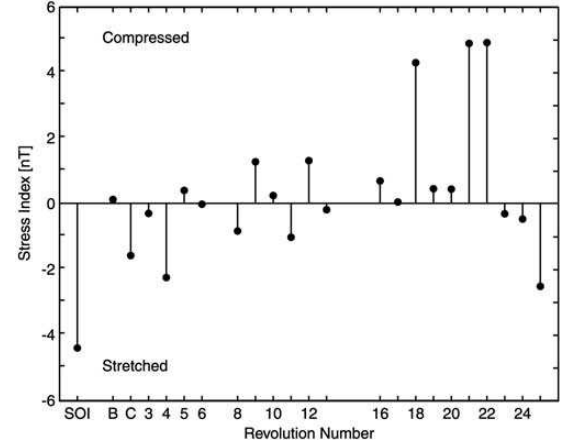


Fig. 26 Stress indices constructed for each pass of Cassini through the inner magnetosphere (from [121]).

The linear fits in Fig. 25 represent an empirical model for the properties of the ring current with system size. *Bunce et al.* [28] used this to confirm that the total magnetospheric field on the dayside stretched out into a magnetodisc for low solar wind dynamic pressures, confirming the results of *Arridge et al.* [13].

The Dst index is used as a measure of the strength of the ring current and stress state of the terrestrial magnetosphere. *Leisner et al.* [121] subtracted a model of Saturn’s magnetosphere from magnetometer data in the inner magnetosphere to produce a similar index for Saturn’s magnetosphere. The important difference between Saturn and Earth is that both internal and external stresses may affect this kronian Dst index, producing compression or stretching of the magnetic field lines. Fig. 26 presents the stress indices calculated by *Leisner et al.* [121] where positive (negative) stress indices indicate a compressed (expanded) magnetosphere relative to a ground state. The calculations indicate several large-scale deviations from the ground state and numerous small-scale deviations near the noise level of the analysis that are consistent with variations in solar wind dynamic pressure.

The radial, steady-state form of the force balance equation for a collisionless, single-ion plasma in the equatorial plane, can be written as:

$$\rho \Omega^2 r - \frac{\partial P}{\partial r} = j_\phi B_z \quad (8)$$

where r is radial distance, P is the particle pressure, j_ϕ is the azimuthal current density, ρ is the plasma mass density and Ω is the angular velocity of the plasma. Here we made the assumption that $B \approx B_z$ in the nominal magnetic equatorial plane (ideal dipole field). The non-trivial challenge for theory and spacecraft observations is to establish which force dominates in balancing the magnetic stress: centrifugal stresses or pressure gradients. Observations and modeling from *Voyager* [130, 124] showed that energetic particle pressure gradients (thermal current) were more important inside $\sim 14R_S$, but corotation centrifugal forces (inertial current) became more important at larger distances, a result consistent with the work of *Arridge et al.* [12]. This result is also supported by the work of *Bunce et al.* [27] who showed that in the compressed state, the thermal and inertial currents were comparable in size but when the magnetosphere is in its most expanded state, the inertial currents are several times stronger than the thermal currents.

In parts of the magnetosphere where the particle pressure gradient is comparable to or greater than the inertial term, the azimuthal ring current density is decisively modified by the behavior of the suprathermal pressure. Furthermore, the pressure gradient force is expected to dominate over the centrifugal force during injection events, when the energetic particle pressure is significantly increased and highly variable.

Arridge et al. [12] re-examined the contribution of these two terms to the force balance in the ring current using Cassini data. Transient current sheet crossings observed beyond $\sim 18R_S$ were used to estimate the magnetic stress, and the lobe magnetic field strength to infer the radial plasma pressure gradient assuming tangential pressure balance across the plasma sheet. They found that beyond $25 - 30R_S$ centrifugal stresses dominated in this force balance, with pressure gradients more important inside this distance. Additionally, the stress balance calculations also yielded an estimate of 10^6 kg for the total mass in the magnetodisc. For mass-loading rates of $10 - 100$ kg/s this requires $3 - 30$ hours ($0.3 - 3$ planetary rotations) to completely replace the mass in the magnetodisc.

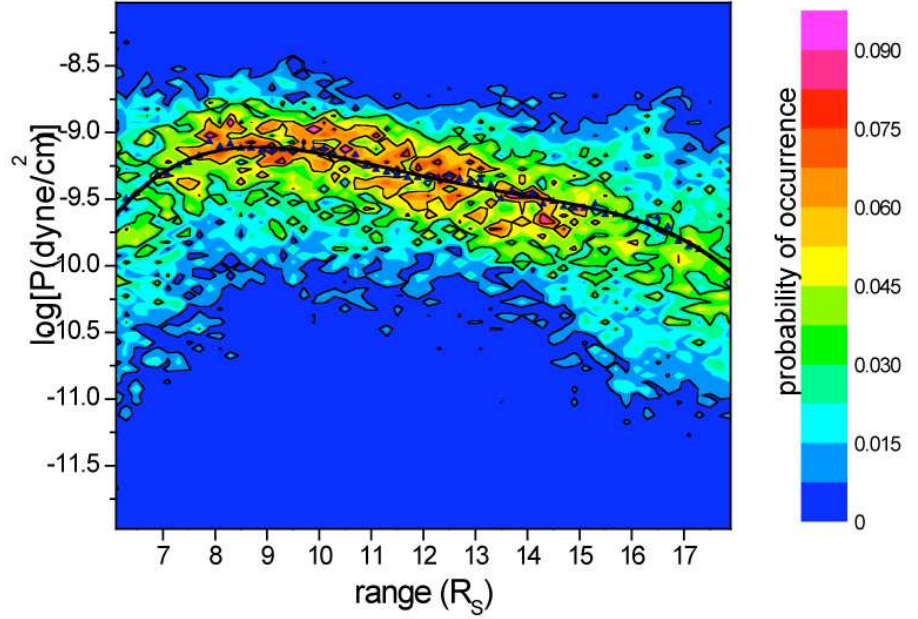


Fig. 27 Radial energetic particle ($E > 3$ keV) pressure profile for the nominal equatorial plane, as observed from all equatorial passes of Cassini, during 3 years in orbit around Saturn. The upper triangles correspond to the pressure medians, while the black solid line is a polynomial fit to the medians (from [160]).

Sergis et al. [159] investigated the energetic plasma pressure in the middle magnetosphere between ~ 8 and $18R_S$ using the MIMI/CHEMS and LEMMS instruments. Fig. 27 shows the suprathermal equatorial pressure profile that corresponds to the first three years of Cassini in orbit, based on equatorial plane data that have been statistically weighted according to the time that Cassini spent within each radial distance interval [159]. The color scale is the pressure probability of occurrence. The suprathermal pressure maximizes inside the ring current, with typical values of $\sim 10^{-9}$ dyne/cm² between ~ 8 and $\sim 10 R_S$, gradually decreasing further out. The measured plasma β is kept close to or above unity outside of $8 R_S$, with indications that the energetic particle population, rather than the denser cold plasma, controls most plasma pressure in this region of the magnetosphere, in agreement with the limited measurements during Voyager [124]. Given the fact that MIMI does not measure the cold plasma pressure, these values should be viewed as a lower limit of both pressure and plasma β . Inside of $8 R_S$, the ring current ions are lost through charge exchange with the neutral cloud and absorption by the icy satellites as described above. Some energetic electrons are lost from satellite interactions and others lose their energy by collisions with the neutral cloud and with dust from the E-ring of Saturn.

The analysis of MIMI/CHEMS compositional data obtained during the first three years of Cassini in orbit (July 2004-July 2007), indicates that the O^+ ions play a very important role in the energetic particle pressure, often being the dominant component. The O^+ partial pressure on average represents more than 50% of the total suprathermal pressure, and, at times, clearly dominates. This becomes more evident in the equatorial plane, in agreement with the density distribution of the neutral water products, and the several O^+ -rich injection events often seen in the equatorial plane.

One of the direct implications of the high- β discovery in a large part of the Saturnian magnetosphere is that a realistic magnetopause pressure balance equation should necessarily include the suprathermal pressure term, in addition to the magnetic pressure supplied by the planetary field.

4.3 Plasma Sheet

The properties of electrons between 0.5 eV and 26 keV in Saturn's magnetotail plasma sheet have been investigated and it was found that the electron temperature is approximately 200 eV beyond $20 R_S$ and was approximately constant with radial distance. The electron distributions are approximately Maxwellian (there is some evidence for Kappa distributions) and occasionally bi-Maxwellian distributions are observed with temperatures of 20 eV and 200 eV. The density at the center of the plasma sheet varies between 10^{-1} cm⁻³ at $20 R_S$ and 10^{-3} cm⁻³ at $60 R_S$ and can be represented by a power-law: $n_e \sim r^{-1.75}$. The electron β was found to maximize at values of 1.0 to 10.0 at the center of the current sheet - the exclusion of ions and energetic particles necessarily mean that this is a lower limit to the tail plasma β .

The plasma density in the lobe was near or at the noise level for the CAPS/ELS instrument and implied that the number density was $\leq 10^{-4} \text{ cm}^{-3}$. No evidence was found for a variation of electron temperature between the lobe and the central plasma sheet.

Arridge *et al.* [15] organized CAPS/ELS and magnetic field observations by SLS3 longitude [117] and studied periodicities near Titan's orbit. They showed that the electron density varied by more than an order of magnitude between a minimum near $170^\circ \pm 20^\circ$ and a maximum near $350^\circ \pm 20^\circ$. The electron temperature was essentially constant with longitude but with some weak evidence for an increase in temperature towards 170° . An analysis of the magnetometer data showed that the effective density modulation was primarily produced by a periodic motion of the plasma sheet and not by a density asymmetry in the frame of the plasma sheet (although one might exist). Interestingly the plasma sheet periodicity was either absent or at a lower amplitude when the dayside field structure was quasi-dipolar.

Observation of plasma-sheet ions is complicated by the fact that corotational flow dominates essentially out to the magnetopause and the fact that the ion thermal speed is typically comparable to the flow speed throughout the magnetosphere. This means that there are strong flow anisotropies, so the instrument viewing is crucial. For CAPS to see plasma-sheet ions, it needs to be looking into the flow, a condition frequently not satisfied because of constraints on the spacecraft orientation to enable measurements by the optical instruments.

From CAPS ion observations during SOI, Young *et al.* [200] reported that the plasma sheet beyond $\sim 9R_S$ was dominated by H^+ ions, although water-group ions indicative of an inner-magnetospheric source did continue to be present (see Fig. 9).

During SOI, however, Cassini was at a latitude of about -13° , and subsequent lower-latitude passes indicated that the apparent H^+ dominance was primarily a latitude effect. Due to the strong centrifugal force on the plasma, heavy ions are particularly closely confined to the equatorial plane. Near the equator, water-group ions are indeed as abundant as H^+ , as seen in Fig. 28, obtained just before noon local time at a radial distance between 15 and $17 R_S$ and much closer to the equatorial plane than the SOI pass. The energy-time spectrogram for the ions in the upper panel of Fig. 28 shows the characteristic strong periodicity associated with the actuation of the CAPS field of view back and forth across the transonic flow. As in the inner magnetosphere (e.g., Fig. 9), there are two bands of ions, the higher-energy one corresponding to flowing W^+ , and the lower-energy one corresponding to flowing H^+ . The actual fluxes are variable, but it is clear that the W^+ constitute a significant portion of the plasma.

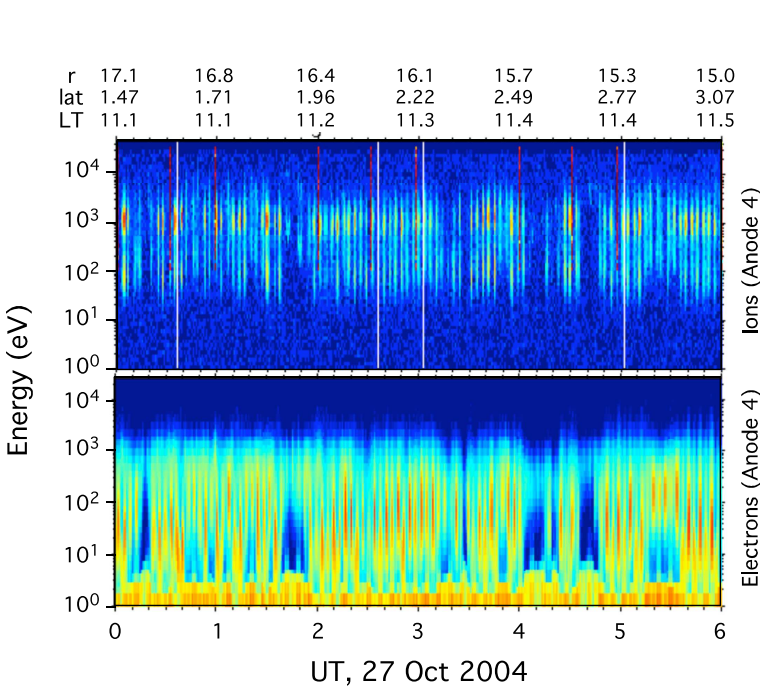


Fig. 28 Energy-time spectrogram of ion (top) and electron (bottom) energy flux observed by CAPS in the near-equatorial dayside plasma sheet. The two peaks in the ion energy spectrum correspond to flowing W^+ (higher energy) and H^+ (lower energy). There is strong modulation at the CAPS actuation period (~ 7 minutes) as the field of view is swept in and out of the flow. In addition to this modulation, there are significant variations in the plasma properties, as seen in both ions and electrons, with regions of cool, dense plasma alternating with regions of hot, tenuous plasma.

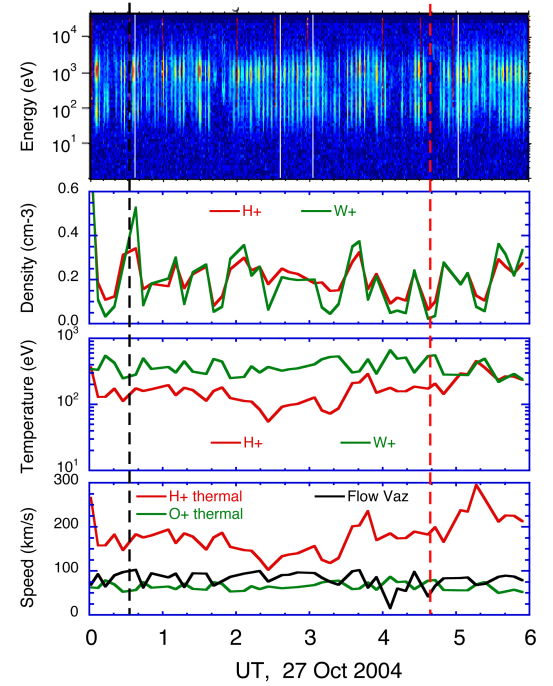


Fig. 29 Bulk moments derived from CAPS measurements for the same interval as Fig. 28, showing the general anti-correlation of the density and temperature, particularly for the W^+ . The bottom panel shows that the ion thermal speed is comparable to the flow speed, accounting for the strong modulation as the instrument field of view is swept in and out of the flow.

Fig. 28 illustrates another aspect of the plasma sheet in the outer magnetosphere, namely that the region beyond $\sim 11R_S$ is often characterized by significant variations in the plasma properties over fairly short time scales. Fig. 28 shows regions of relatively cool, dense plasma alternating with regions of more tenuous, hotter plasma. This variation can be seen in both the ions (upper panel) and the electrons (lower panel). Fig. 29 shows the ion moments derived from a numerical integration of the CAPS SNG observations, confirming the anti-correlation of the density and temperature of the plasma during this interval, especially for the W^+ ions. In the hot, tenuous regions, the W^+ is more strongly depleted than the H^+ . The bottom panel of the figure confirms what was mentioned above, namely that the ion thermal speeds are comparable to the bulk flow velocity (dominantly azimuthal), particularly for the W^+ .

It is possible that the alternations in the plasma properties seen in Figs. 28 and 29 are simply due to rapid variations in the effective latitude of the spacecraft, due to flapping of the plasma sheet or azimuthal variations in its thickness. It is also possible that these different regimes represent the intermingling of flux tubes with different plasma content. *McAndrews et al.* [129] suggest that similar low-density, hotter regions seen in the tail plasma sheet are the remnants of previously distended flux tubes that have been broken open by centrifugal stresses on the nightside, releasing the bulk of the cool, heavy plasma near the equator. Such emptied flux tubes would therefore allow the return of magnetic flux to the inner magnetosphere, to replace the heavily loaded flux tubes there with more buoyant ones containing the hotter, tenuous remnant plasma. As discussed above in Section 1.3 and in Section 5.1, there is good evidence that this interchange process is an important means by which Saturn sheds the plasma produced in the inner magnetosphere. Discrimination between these two possible explanations of the observed plasma sheet structure awaits further analysis of the Cassini data.

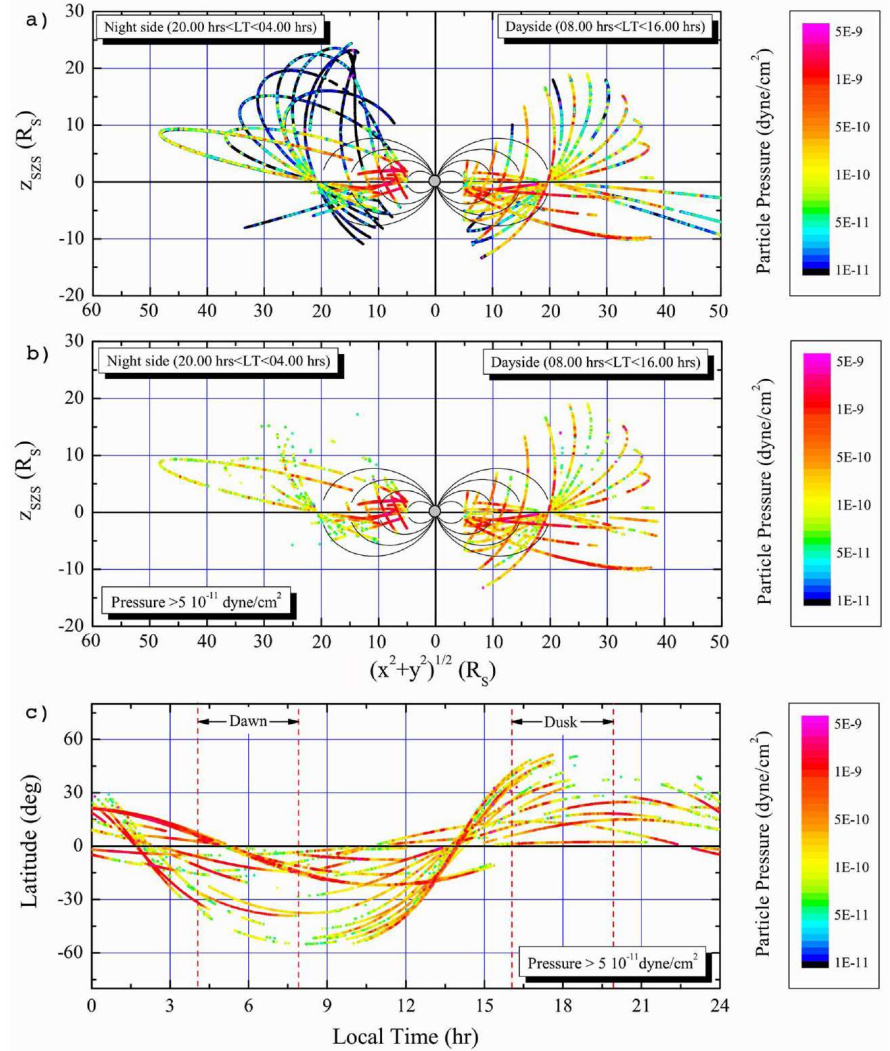
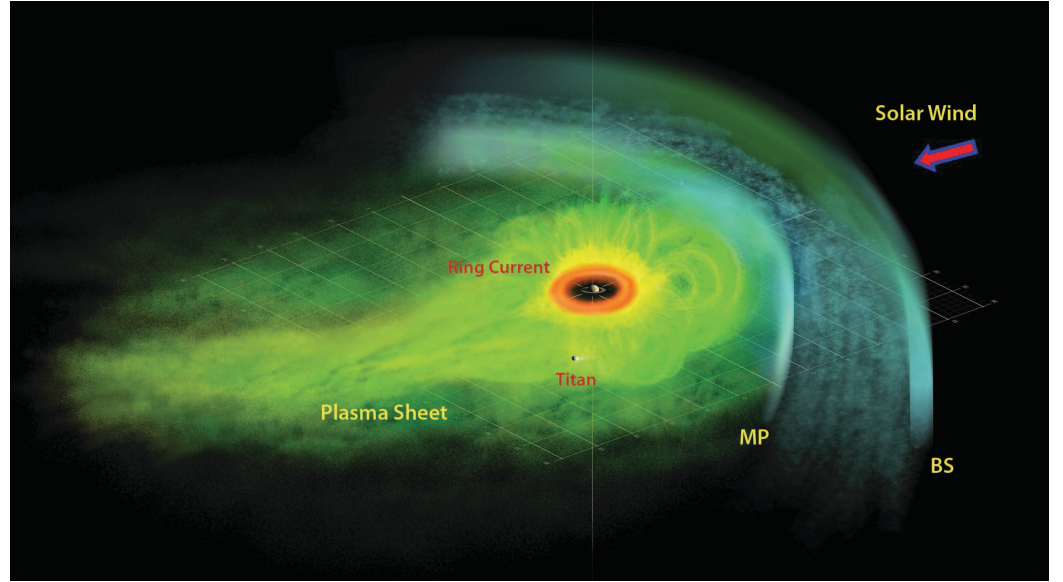


Fig. 30 Pressure profiles (~ 3 to $4,000$ keV) obtained for the July 2004 to June 2007 period and projected onto the $(\sqrt{X^2+Y^2}, Z)$ plane. Top: Pressure profile on the dayside (right) and night-side (left) over the full dynamic range measured by the CHEMS and LEMMS sensors ($5 \times 10^{-13} - 5 \times 10^{-9}$ dynes cm^{-2}), clearly illustrating the orbital coverage. Middle: The same data but for a threshold $> 5 \times 10^{-11}$ dynes cm^{-2} ; the day-night asymmetry at $R > 20R_S$ is striking. Bottom: Pressure coverage in local time and along the Z axis for all data, but also including the dawn-dusk coverage not shown in the other two panels (from [112]).

Fig. 31 Schematic representation of Saturn's plasma and neutral environment. Saturn is at the centre, with the red 'doughnut' representing the distribution of dense neutral gas (H, O, O₂ and OH) outside the rings. Beyond this region, energetic ions populate the plasma sheet to the day side magnetopause, filling the faintly sketched magnetic flux tubes to higher latitudes and contributing to the ring current. The plasma sheet thins gradually towards the night side. (from [112]).



The spatial extent and pressure structure of the plasma sheet has been investigated by mapping the partial ion pressure (> 3 keV) over a period of ~ 3 years, from July 1, 2004 to June 30, 2007 [112]. The results are shown in Fig. 30 plotted in the ρ, Z plane and separated into the dayside and night side parts. The top panel includes all measured off-equatorial values but excludes the dawn-dusk portion so as to obtain a clear separation of day-night effects. Although the orbital coverage in Z is not uniform, the higher pressures on the dayside appear to extend to much higher latitudes than the night side, certainly at $< 20R_S$. This fact is clearly evident in the middle panel, where pressures $< 5 \times 10^{-11}$ dynes/cm² have been omitted. Not only is the day-night asymmetry striking, but also the shape of the night side plasma sheet beyond $\sim 20R_S$ is outlined and is seen to be tilted northward at an angle $\sim 10^\circ$, although the orbital coverage in this region is not extensive. Examination of each Cassini orbit at all available local times suggests that the dayside plasma sheet extends to the magnetopause at local noon but thins gradually toward the night side, even though the detailed distribution with local time is not fully determined because of incomplete latitudinal/local time coverage.

Our current understanding that has evolved from the pressure distribution so far is shown in Fig. 31. This view from above Saturn's equatorial plane illustrates the compressed dayside plasma sheet and indicates its expansion to northern and southern latitudes. It is expected that the sheet gradually thins on the dusk side but is drawn tail-ward at midnight and again inflates at dawn. Whether there is loss of plasma on the night side is not clear, because this sketch represents an average picture of all orbits over a nearly three-year period. Acceleration events, however, have been observed repeatedly both in the magnetotail [112] and in parts of the magnetosphere, where the injected plasma cloud clearly corotates with the planet, as illustrated in Fig. 24.

4.4 Magnetotail

The interaction of the solar wind with Saturn's internal and external fields produces a long magnetotail on the night side in which the magnetic field decreases away from the planet at a much slower rate than a dipole field. Both drag applied by the solar wind on the magnetosphere, and the reconnection of the IMF field lines to those of Saturn play a role in transferring magnetic flux from the day side magnetosphere to the night side magnetotail.

At the center of the magnetotail, a current sheet maintained by the hot plasma of Saturn's magnetosphere keeps the magnetic field at a very low value. Above and below the current sheet, the magnetic field is much stronger, points nearly radially outward ($B_r > 0$) above the current sheet, and radially inward ($B_r < 0$) below the current sheet. These regions outside the current sheet are called the lobes and house the open flux of Saturn's magnetosphere, which is connected to the solar wind IMF field at one end and to Saturn's ionosphere on the other. Fig. 32 shows the strength of the magnetic field (directed mainly in the radial direction) observed during the inbound leg of Rev. 26 and that expected from Saturn's dipole in the lobe region (dashed line).

In the low-latitude regions of the magnetotail the signs of the radial and azimuthal components of the field are observed to be opposite to each other outside a radial distance of $\sim 12R_S$. Thus, the field lines appear to have a bent-back configuration in

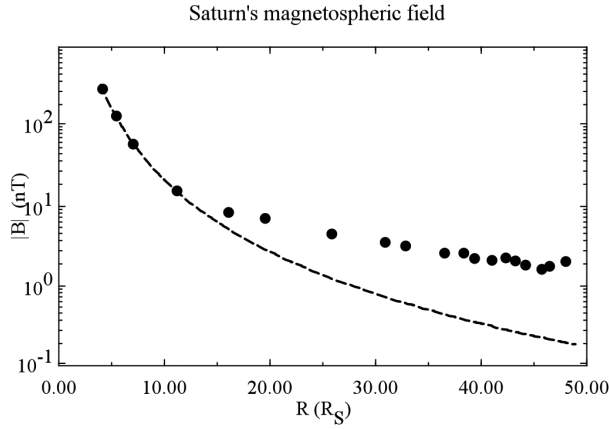


Fig. 32 Magnetic field strength in the low latitude lobe region (dots) observed during the inbound leg of Rev. 26 and the dipole field in the same region (dashed line).

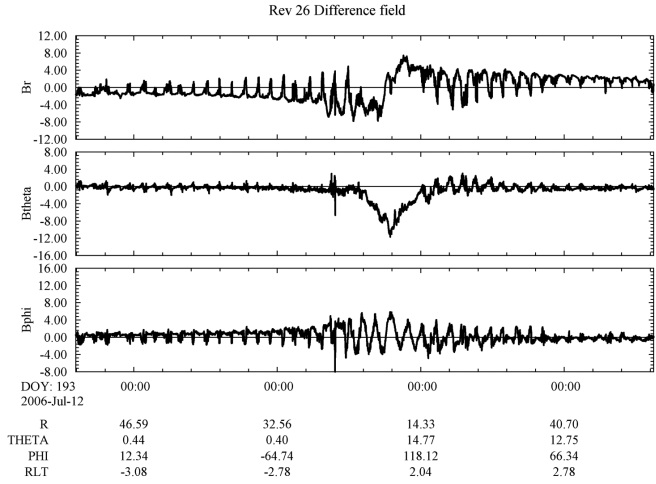


Fig. 33 The difference field observed during Rev. 26. Notice, the out of phase periodicities observed in the B_r and the B_ϕ components. In each rotation of Saturn, the B_r component reverses twice.

the outer magnetosphere. This swept-back appearance arises from the presence of radial currents flowing in the magnetosphere which enforce corotation on the plasma.

A striking feature of magnetic field observations from the magnetotail region is the presence of periodicities close to the rotation period of Saturn [9]. Fig. 33 shows an example of such periodicities. The two reversals of B_r in each spin period illustrate that the spacecraft travels across the current sheet in a periodic fashion, which is possible only if the current sheet is tilted with respect to Saturn's equatorial plane and is rotating with a period close to that of Saturn. A model put forward by *Khurana et al.* [105] postulates that the tilt of the current sheet arises naturally from the action of solar wind lift on an azimuthally asymmetric magnetosphere (see Fig. 6)

Southwood and Kivelson [179] also propose a tilted current-sheet interpretation for the periodicities in the magnetotail. In their model they suggest that the tilt is produced by an effective dipole moment rotating in the equatorial plane in the middle magnetosphere. They show that a system of field-aligned currents flowing on magnetic shells between 12 and 15 R_S can produce a tilted dipole beyond these shells but a uniform “cam-shaft” field inside, consistent with the periodicities in the azimuthal and radial magnetic field components. *Carbary et al.* [33] proposed an alternative interpretation and suggested that compressional motions in the inner and middle magnetosphere, produced by an azimuthally asymmetric density profile, would translate to transverse motions in the outer magnetosphere when Saturn's dipole was tilted with respect to the solar wind.

Plasma flow observations from Saturn's magnetotail shed light on the global convection pattern discussed in Section 1.3. The main issues are the extent to which corotation is enforced on the night side, evidence for the “shedding” of material originating in the inner plasma source region, and evidence for the return of magnetic flux to the day side. Fig. 34 shows the results of a recent study by *McAndrews et al.* [129] of ion flows in Saturn's magnetotail. For plasma dense enough to be detectable by the CAPS IMS, the flows are dominantly in the corotational direction, even out to very large distances ($\sim 40R_S$), although the flow speed is well below full corotation. However, beyond $\sim 20R_S$, there is no evidence of an inward component of these flows, and it appears that the pull from the ionosphere may be inadequate to drag the more distant flux tubes around to the day side to complete their convective circuit.

For the intervals studied by *McAndrews et al.* [129], the plasma was relatively cool and dense, with a water-group/hydrogen composition similar to that seen in the dayside plasma sheet (Section 4.3), indicative of plasma originating in the inner magnetosphere. An estimate of the mass per unit flux for these intervals shows it to be generally at or below the critical value above which the magnetic field should be unable to confine the plasma [72]. This evidence confirms the conclusion that these flux tubes are still closed and still loaded with inner magnetospheric plasma, although they may not be able to complete the circulation onto the dayside intact.

Another aspect of the tail plasma studied by *McAndrews et al.* [129] was that between the intervals with a detectable ion population were numerous intervals of much lower density, as indicated by the more sensitive electron measurements. While some of these low-density intervals may reflect excursions to higher latitudes in the flattened tail plasma sheet, at least some of them are attributable to flux tubes depleted of their plasma content through down-tail loss to a planetary wind [129]. They thus presumably represent the magnetic flux that must return to the dayside outer magnetosphere (cf., [193]).

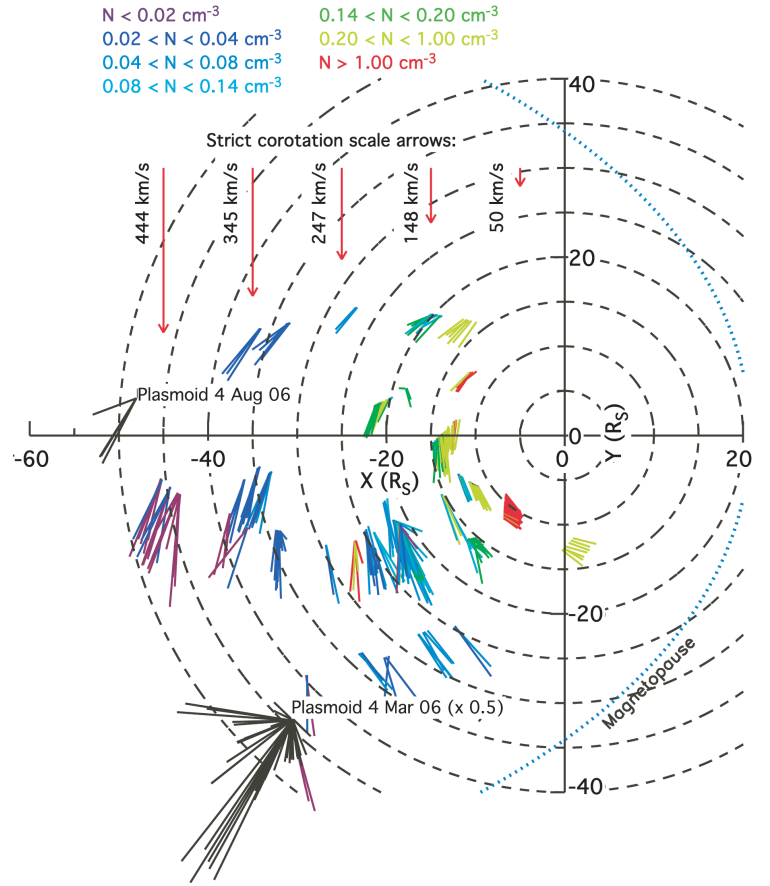


Fig. 34 Equatorial plane projection of plasma flow velocities derived from CAPS IMS data for various intervals during Cassini passes through Saturn's magnetotail region. The vectors originate at the spacecraft location and point in the direction of the flow, with a length proportional to the flow speed and a color determined by the density. Velocities derived by *Hill et al.* [87] for two plasmoid events are also indicated (colored black) (from [129]).

The down-tail loss of plasma may occur by way of magnetic reconnection of flux-tubes strongly distended by centrifugal forces. Evidence for magnetic reconnection and the subsequent expulsion of a plasmoid has been seen in both magnetic field [93] and plasma measurements [87]. The locations of the two plasmoid events reported by *Jackman et al.* [93] for which *Hill et al.* [87] could measure plasma properties, are shown in Fig. 34, with their corresponding flow vectors, which have a strong radial component. However, to date very few such plasmoid events have been identified in Cassini tail observations, suggesting that large-scale reconnection of this type may be relatively infrequent, and smaller-scale processes may dominate the normal mass loss down-tail. One clue to the frequency of occurrence of large-scale plasmoid release events is that just before the in situ detection of one of the events, the MIMI/INCA instrument observed a burst of energetic neutral atoms emanating from a location midway between Saturn and Cassini, probably a signature of the reconnection event that produced the plasmoid [87]. Such ENA brightenings have been attributed to a substorm-like process taking place in the near-tail region [133], and the brightenings are associated with bursts of Saturn Kilometric Radiation (SKR) and possibly with injections of energetic particles deeper into the inner magnetosphere [125]. The occurrence rate of ENA brightenings, SKR enhancements, and energetic particle injections may therefore suggest the frequency of plasmoid releases into the tail, indicating whether or not this mechanism is sufficient to shed the plasma produced in the inner magnetosphere or whether other, smaller-scale processes might also be needed. This analysis has not been done to date.

4.5 Global MHD Models

Hansen et al. [81] were the first to develop a global MHD model to study the large-scale interplay between the solar wind, Saturn's fast rotating embedded magnetic dipole and magnetospheric plasma sources. They modeled Saturn's magnetosphere using a version of the global, 3D MHD model BATS-R-US [143]. Their present model [82] includes several important improvements, such as a substantially modified prescription of the mass loading distribution and the use of observed conditions to prescribe the upstream solar wind. Other improvements include the use of the semi-relativistic form of the MHD equations [77], an implicit time stepping algorithm [186], and better resolution.

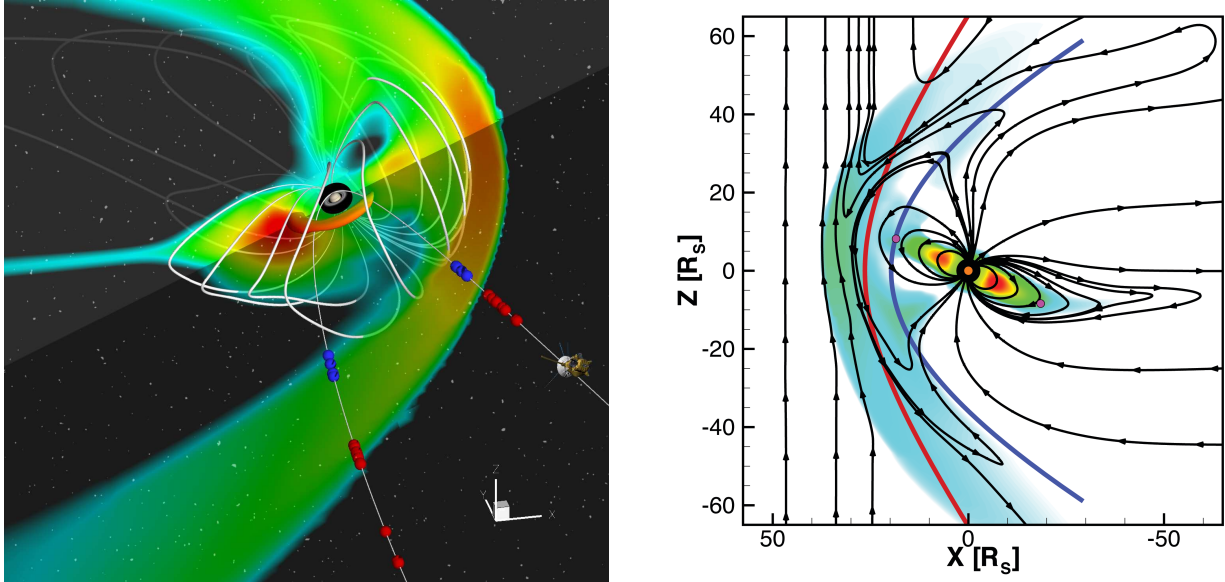


Fig. 35 Left panel: A snapshot of Saturn's simulated magnetosphere during the SOI period. The thick white lines are a 3D representation of the last closed magnetic field lines. On the dayside they represent the magnetopause while on the nightside they represent the inner magnetosphere. The crescent at 6-7 R_S is a density isosurface showing that the plasma is concentrated near the rotational equator. The color code represents pressure in the equatorial and noon-midnight planes. The solid grey trajectory of Cassini is shown with observed bow shock (red) and magnetopause (blue) crossings (from [78]). Right panel: Noon-midnight meridional plane of Saturn's simulated magnetosphere at the time of the first bow shock crossing. Color contour is the thermal plasma pressure with black lines representing magnetic field lines. The solid red and blue lines are respectively the *Slavin et al.* [171] average magnetopause and bow shock models. The intersection of Titan's orbit with this plane is shown as two small pink dots (from [82]).

Because the addition of mass to the kronian system is significant, *Hansen et al.* [82] include this process in their MHD model through appropriate source terms for ionization, pickup, recombination and ion-neutral drag. The inner source due to dust and icy satellites is modeled as an axisymmetric torus confined near the equatorial plane using data from *Richardson and Sittler* [145] and *Richardson et al.* [147]. They use an average mass of 16.6 amu which assumes a nearly equal mix of OH and O. A total mass loading rate of $\sim 10^{27} \text{ s}^{-1}$ is used in the *Hansen et al.* [82] simulations (but this is an adjustable parameter that can be scaled as necessary). Mass loading due to Titan is modeled as an axisymmetric torus. The torus is centered on Titan's orbit and has a much lower mass addition rate than the inner source. The Titan related mass loading rate is $\sim 5 \times 10^{25} \text{ s}^{-1}$ and it was obtained by using a peak neutral density of $\sim 10 \text{ cm}^{-3}$ combined with a neutral lifetime ($\sim 3 \times 10^7 \text{ s}$ [19]) and average mass (14 amu).

Hansen et al. [82] assume that the rotation and dipole axes are aligned and tilted 24.48° away from the Sun. The simulation domain covers the region of $96R_S < X < -576R_S$, $-192R_S < Y, Z < 192R_S$. Utilizing adaptive blocks, they are able to highly resolve the inner equatorial plane while also resolving the bow shock, magnetopause and tail regions appropriately. The smallest computational cells near the icy satellite mass loading region in the equatorial plane are $3/16 R_S$ across while the largest cells ($6 R_S$) are located far downtail. The inner boundary is at $3 R_S$.

Global MHD simulations have been successfully used to put the Cassini observations in a global perspective and to predict new phenomena. *Hansen et al.* [82] applied the model to describe Saturn's magnetosphere under conditions appropriate for the period just before the Cassini orbit insertion (26–29 July 2004). They successfully simulated the bow shock and magnetopause crossings [78] and investigated the compressibility of the dayside magnetopause [82]. The compressibility derived from the simulations ($\alpha \approx 5.2$ is in excellent agreement with the observed value (see Section 6.4.2). They also successfully simulated the bowl shaped magnetodisk, the plasma 'drizzle' along the dusk magnetotail and the global magnetospheric convection pattern [82]. These features can be seen in Fig. 35.

Fukazawa et al. [64, 65] used a different global MHD model to investigate the influence of IMF B_z on Saturn's magnetosphere. They found that the subsolar magnetopause and bow shock positions are sensitive to the solar wind dynamic pressure, but they are insensitive to the IMF B_z and the amount of reconnected magnetic flux. They also found that vortices were formed in the magnetosphere that increased magnetic reconnection along the flanks of the magnetopause.

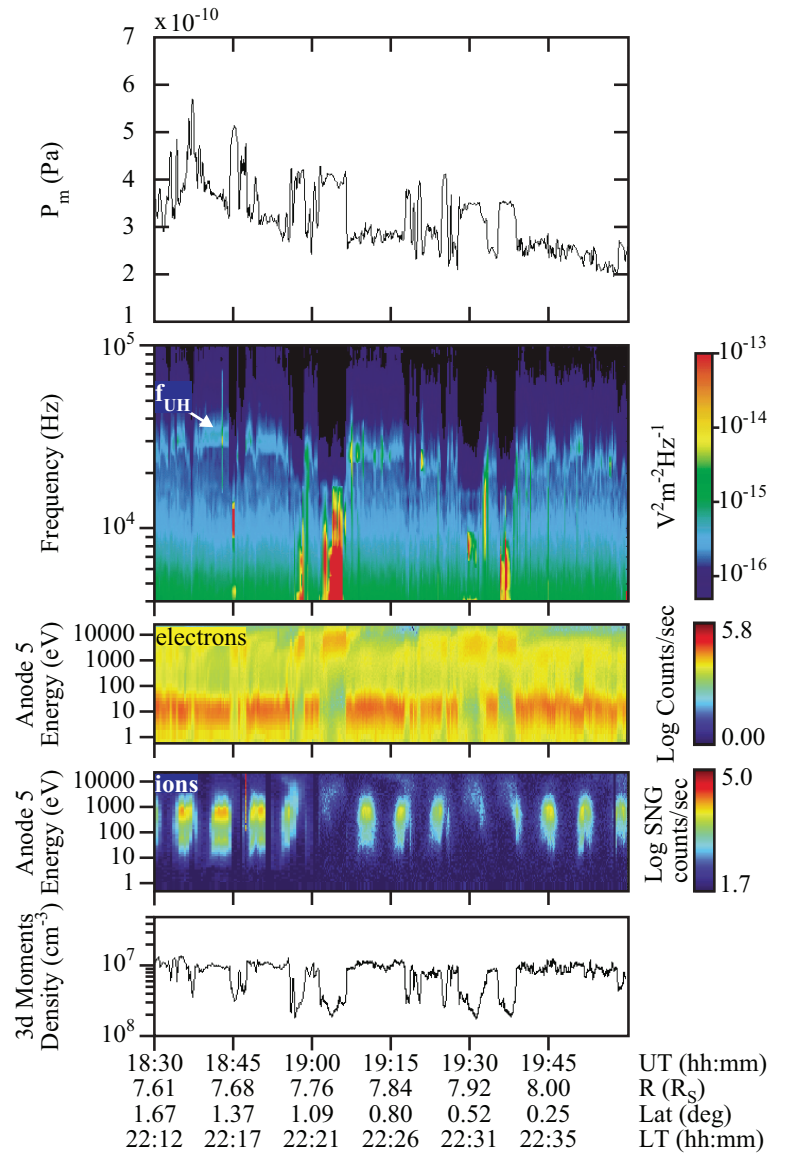
5 Ionosphere-Magnetosphere Coupling

5.1 Radial Transport

Saturn's magnetospheric plasma is primarily produced deep in the magnetosphere, partly by photoionization but predominantly by electron impact ionization of the water-group neutral gas cloud liberated by the Enceladus geysers and redistributed by charge-exchange with corotating plasma. Because the electron temperature is regulated by collisional equilibration with the pick-up H^+ ions, little electron impact ionization can occur inside $L \sim 6$, where the H^+ corotational energy finally exceeds the 10 – 20 eV needed for ionization. Thus, even though the neutral cloud is most dense near Enceladus itself, the peak plasma production is further out.

The peak in plasma production at $L \sim 6$ leads to a negative radial gradient in the flux-tube plasma content beyond that distance, which is unstable to flux-tube interchange. The onset of interchange rapidly transports the plasma outward into the outer magnetosphere. Inside of $L \sim 6$, the transport is much slower (see also [35]), and the primary loss mechanism is recombination. Some authors have hypothesized a global circulation pattern in the inner magnetosphere (e.g., [73, 80], which would shorten the

Fig. 36 A multi-instrument analysis of a series of injection events on October 28, 2004, showing correlations between enhancements in the magnetic pressure (panel 1), the disappearance of the upper hybrid emission band (panel 2) coinciding with significant density drop-outs (panel 5), and the depletion of the low-energy plasma population coinciding with the appearance of a hot plasma component (panels 3 and 4) inside the well-defined boundaries of the interchanging magnetic flux tubes (from [7]).



inward transport time, but so far analysis of CAPS ion data shows radial flows of less than $1 - 2$ km/s [168, 199], although a comprehensive study has not yet been done.

The situation is different with the electrons. Phase space density analysis of the CAPS/ELS electron measurements of both the hot and cold electron populations located the source of the cold electron population (< 100 eV) in the inner magnetosphere and the source of the hot electron component (100 eV to > 10 keV) in the outer magnetosphere at $L \sim 11$ [154]. However, the simple plasma transport cycle of outward-convecting flux tubes containing cold, dense plasma and inward-convecting flux tubes containing hot, tenuous plasma required further investigation when *Burch et al.* [31] found evidence of pitch angle distributions consistent with the outward transport of hot electrons. Subsequently, *Rymer et al.* [155] presented a circulation model for electrons which originate in the inner magnetosphere and circulate in a cycle of outward and inward convection, driven by the centrifugal interchange instability. Heated plasma drifts out of the inward-convecting flux tubes through gradient and curvature drifts, disappearing by $L \sim 6$ when, caught up in the corotating plasma, the heated plasma subsequently convects radially outward along with the colder and denser background plasma [155].

The first observational evidence that the interchange process is occurring at Saturn was obtained during Cassini's orbit insertion in 2004 [6, 30, 86, 119, 125]. Centrifugal interchange events have magnetic and plasma signatures consistent with distant magnetic flux tubes containing hot tenuous plasma convecting inward to replace tubes containing cold, dense plasma. Such injection events occur throughout the plasma source region in the range $5 < L < 11$ [86, 154]. Due to adiabatic gradient and curvature drifts, the injected plasma exhibits significant longitudinal drift dispersion, which is evident as V-shaped dispersion signatures on linear energy-time plots [86]. By estimating the slope and thickness of the V-shaped signature, *Hill et al.* [86] were able to deduce the age and longitudinal width of the injection events.

Remote events have a dispersed energy signature with decreasing ion energy and increasing electron energy occurring sequentially within the boundaries of the event [200]. Similar energy dispersion curves can be seen for the more energetic ions [125]. Characteristically, local events have deep density gradients and high plasma temperatures coincident with the abrupt boundaries of the injection event [7], with higher plasma temperatures exceeding the background temperatures by a factor of thirty [154]. Fig. 36 is a multi-instrument display depicting magnetic and plasma parameters during a series of local injection events taken during Cassini's first full orbit around Saturn on October 28, 2004. The top panel shows enhancements in the magnetic pressure that correlate with the intermittent disappearance of the upper hybrid resonance emission band (panel 2) and significant drop-outs in the plasma density (panel 5). Another characteristic signature of these injection events is the depletion of the low-energy plasma population coinciding with the appearance of a hot plasma component (panels 3 and 4) inside the well-defined boundaries of the interchanging magnetic flux tubes [7]. The local events show evidence of decreasing ion energies and increasing electron energies occurring simultaneously within the boundaries of the event with little dispersion [30]. The low plasma densities and hotter temperatures found inside the local injections are characteristic of the magnetospheric plasma found at larger radial distances [30].

Injection events also have characteristic signatures in the magnetic field and plasma wave data. Plasma waves associated with density-depleted flux tubes include intense, narrow-banded electrostatic emissions at the electron cyclotron harmonics [131] and whistler-mode electromagnetic chorus emissions [88]. The onset of these plasma waves is clearly associated with the well-defined boundaries of the inward-convecting magnetic flux tubes. In addition to the plasma wave signatures, there are magnetic field signatures associated with these events. Typically the dispersion signatures on the energy-time CAPS spectrograms correlate with diamagnetic depressions in the magnetic field magnitude [7, 86], although there are injection signatures which correlate with diamagnetic enhancements as well [7]. Although both magnetic signatures correspond to inward-propagating magnetic flux tubes containing hotter, low-density plasma, the deepest density cavities and largest temperature increases within the boundaries of these injection events correlate with magnetic field enhancements [7].

The rapid outward transport of inner magnetospheric plasma has two major implications for magnetospheric configuration. First, as discussed above, the presence of this plasma gives rise to a ring current that significantly distorts the magnetic field. Second, the magnetosphere has to find a way to drain it to maintain an approximate steady state. The relatively low densities in the outer magnetosphere make recombination an unlikely solution, and the tiny size of the loss cone likewise rules out significant losses from precipitation. Thus, the material must be transported out of the magnetosphere. This problem was addressed by *Goertz* [72], who suggested that the plasma is lost to a planetary wind (see [193]) when loaded flux tubes convect into the night side and break open. As discussed above, this would occur when the magnetic tension is unable to enforce azimuthal motion, i.e., when the mass per unit flux exceeds a critical value related to the magnetic field strength [72].

A recent study of plasma in the magnetotail [129] has shown that, even to downtail distances $\sim 40 - 50 R_S$, regions of cool, dense, partially-corotating water-group plasma are commonly encountered, but the great majority of these have an estimated mass per unit flux at or below the critical value. Between these apparently intact flux tubes bearing inner magnetospheric plasma, there are regions of significantly lower density (typically below the CAPS threshold for ion detection, but still detectable in the electrons). The interpretation of this finding is that flux tubes that were sufficiently loaded to exceed the critical limit have broken open earlier in their passage through the tail, losing the bulk of their contents down-tail, and returning to the day side

with a much more tenuous, hotter, and heavy-ion-depleted residual plasma. These emptied flux tubes subsequently form the low-density regions seen in the dayside outer magnetosphere, interspersed with mass-loaded flux tubes that have not yet exceeded their critical limit in their passage through the night side.

5.2 Corotation, Subcorotation and Corotation Breakdown

The highly conducting layer in the ionosphere is thin compared to the radius of the planet. Therefore, the height-integrated ionospheric current density can be written as [193]:

$$\mathbf{j}_{iono} = \Sigma (\mathbf{u}_n - \mathbf{u}_{mag}) \times \mathbf{B} \quad (9)$$

where Σ is the height integrated ionospheric conductivity, \mathbf{u}_n is the velocity of the neutral atmosphere at ionospheric altitudes, \mathbf{u}_{mag} is the velocity of magnetospheric plasma just above the ionosphere. The frozen-in MHD condition ($\mathbf{E} = -\mathbf{u} \times \mathbf{B}$) implies that plasma elements originally on a magnetic field line remain on the field line at any later time. This means that the plasma velocity just above the ionosphere, \mathbf{u}_{mag} , determines the plasma velocity perpendicular to this field line (the convection velocity) everywhere along this field line (e.g., [76]).

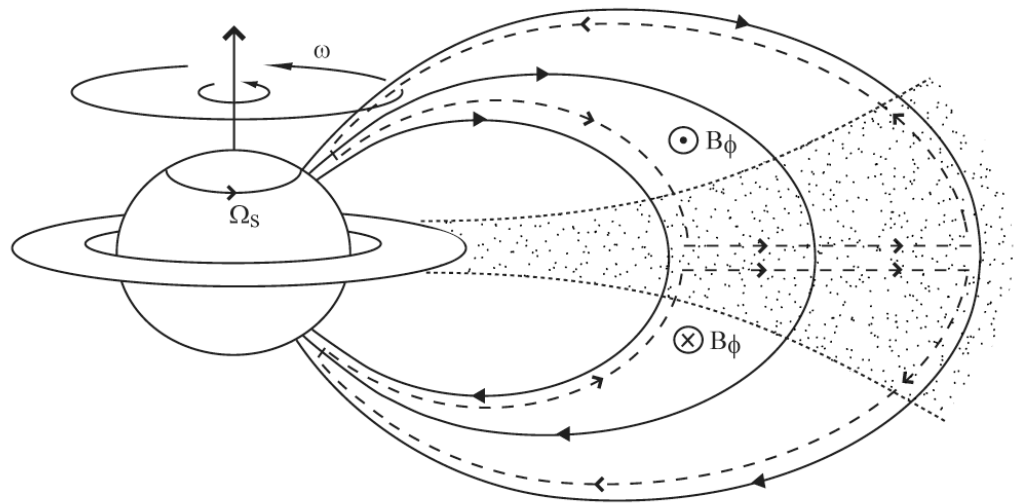
If the height-integrated ionospheric conductivity is very large ($\Sigma \rightarrow \infty$) the upper atmosphere and the magnetosphere above must move with the same velocity, $\mathbf{u}_n = \mathbf{u}_{mag}$ [193]. Since the upper neutral atmosphere corotates with the planet with an angular velocity Ω_u (note that Ω_u is not the internal rotation rate of Saturn), the magnetospheric footpoint of the field line moves with a velocity of $\mathbf{u}_{mag} = \Omega_u \times \mathbf{r}$. In other words, the footpoint of the magnetospheric field line *corotates* with the upper atmosphere.

As it has been discussed earlier (see Section 3) the rings, Enceladus and the icy satellites produce $\sim 10^2$ kg of water group ions per second near the equator between $3R_S$ and $5R_S$ radial distance. This plasma is “loaded” to rotating closed magnetic field lines that are increasingly stretched by the balance between magnetic stresses and centripetal forces [70, 84].

In the MHD limit the ionosphere rotates with Ω_S and it “drags along” closed magnetic field lines that are increasingly “mass loaded” in the equatorial region. This process generates a coupling current system that is depicted in Figure 37.

Subcorotation is primarily caused by addition of newly ionized particles to the local plasma population (see [126, 75, 76]). The process of ion pick-up results in a slowing of the plasma flow since newly-created ions enter the plasma essentially at rest in the Keplerian frame, thereby adding negative momentum in the plasma frame. It is interesting to note that the thermal velocity of a uniformly filled pickup ring is the same as the transport velocity of the magnetic field lines. This means that even a small percentage of heavy pickup ions (such as W^+) have a large contribution to the plasma pressure. The evidence for the pick-up of new ions in the inner magnetosphere is thus consistent with the observations of subcorotation in this region (e.g., [144, 63, 125, 199]). The left panel of Fig. 38, from [199], shows the azimuthal plasma flow speeds derived from CAPS

Fig. 37 A meridional cross section through Saturn’s magnetosphere extending to distances of $\sim 15 - 20R_S$. The arrowed solid lines are closed magnetic field lines. The rotating plasma is shown by the dotted region. The angular velocity of a particular shell of field lines, ω , and the angular velocity of the neutral upper atmosphere in the Pedersen layer of the ionosphere, Ω_S , are also shown. The frictional torque on the magnetospheric flux tubes is communicated to the equatorial plasma by the current system shown by the arrowed dashed lines. This current system bends the field lines out of meridian planes into a ‘lagging’ configuration. [45].



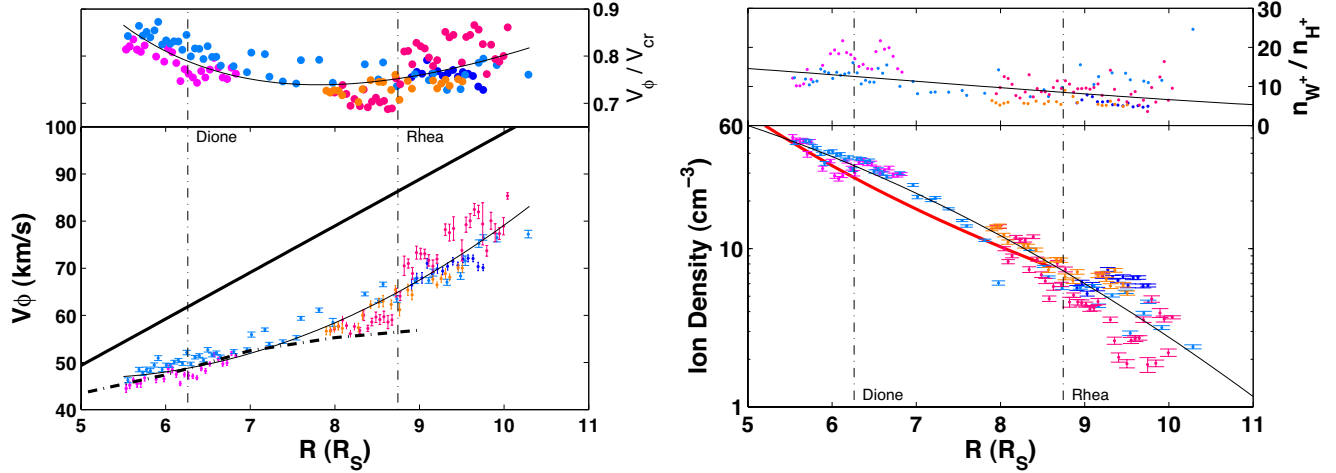


Fig. 38 Left panel: Azimuthal flow speed derived from CAPS IMS measurements made on several passes through the inner magnetosphere (different colors represent different passes) (from [199]). The heavy solid line shows the value of azimuthal flow for perfect corotation, and the top panel shows the ratio of the measured speed to perfect corotation. The heavy dashed curve is the azimuthal flow speed inferred by *Mauk et al.* [125] from SOI observations of energetic particle injections, and the thin curve is an analytical function fit to the CAPS measurements. Right panel: Total ion density derived from the same measurements as shown in the left panel. The top panel shows the ratio of the derived water-group density to the derived H^+ density. The red curve in the lower panel is the analytical function from a fit to the RPWS total electron density [139], and the thin curve is an analytical function fit to the CAPS measurements.

observations from several inner magnetosphere passes, with the flow curve inferred by *Mauk et al.* [125] shown as a dashed curve.

Local ion pick-up, however, is not the only process that could produce the observed sub-corotation. In fact, there are three candidate causes:

1. local ionization within the inner magnetosphere, via photoionization or electron-impact ionization, as discussed above (which is a plasma density source as well as a momentum-loading process);
2. momentum exchange between existing plasma and neutrals, which could be either ion/neutral collisions or charge exchange, but which is dominated by charge exchange (e.g., [157] momentum-loading with no change in density);
3. outward transport of plasma, with low ionospheric conductivity preventing its acceleration up to full corotation as discussed by *Hill* [85].

The relative importance of these processes is determined by a complex mix of factors, including the height-integrated Pederson conductivity of Saturn's ionosphere, the radial dependence of the density and composition of neutrals, the energy distribution of magnetospheric electrons, and the ion density and composition. Using plasma parameters derived from the Voyager encounters *Richardson et al.* [144] and *Saur et al.* [157] modeled these three processes for Saturn's inner magnetosphere and were able to approximately reproduce the Voyager-observed subcorotation, including some notable dips in the azimuthal velocity profile, with a very small effective Pedersen conductivity and substantial ionization and charge-exchange (at roughly equal rates throughout the modeled region).

Analysis of Cassini data can likewise help identify the relative contributions of the various processes producing subcorotation and thereby pinpoint the primary plasma source region. RPWS measurements [138, 139] showed that the equatorial electron density in the inner magnetosphere ($3.6 < L < 8.6$) falls off with distance as $\sim L^{-4.1}$. Conservation of flux-tube content during radial transport would produce a radial density dependence of L^{-4} (for uniform density within the flux tube; or L^{-m} where $m < 4$ if the plasma is equatorially confined due to temperature anisotropy or centrifugal effects). The fact that m is found to be greater than 4 suggests diffusive transport of plasma from a source in the inner region to a sink beyond $L \sim 8.6$.

A subsequent analysis of CAPS ion observations for a number of equatorial passes through the inner magnetosphere produced the density profile shown in the right panel of Fig. 38 [199]. Comparison with the *Persoon et al.* [139] profile, indicated by the red curve, shows generally good correspondence, but a slightly different radial dependence. The best fit relationship found by *Wilson et al.* [199] was not L^{-m} , but rather $n \sim A \times \exp(-BL^2)$. When multiplied by L^4 to approximate flux-tube content, this function actually reveals a peak in the estimated flux-tube content at $L \sim 7$. If a multiplier of L^3 is used to qualitatively account for equatorial confinement, the peak is at $L \sim 6$. This is consistent with the more sophisticated analysis of flux-tube content performed by *Sittler et al.* [170] using CAPS observations from SOI and inferred temperature anisotropies. Their derived flux-

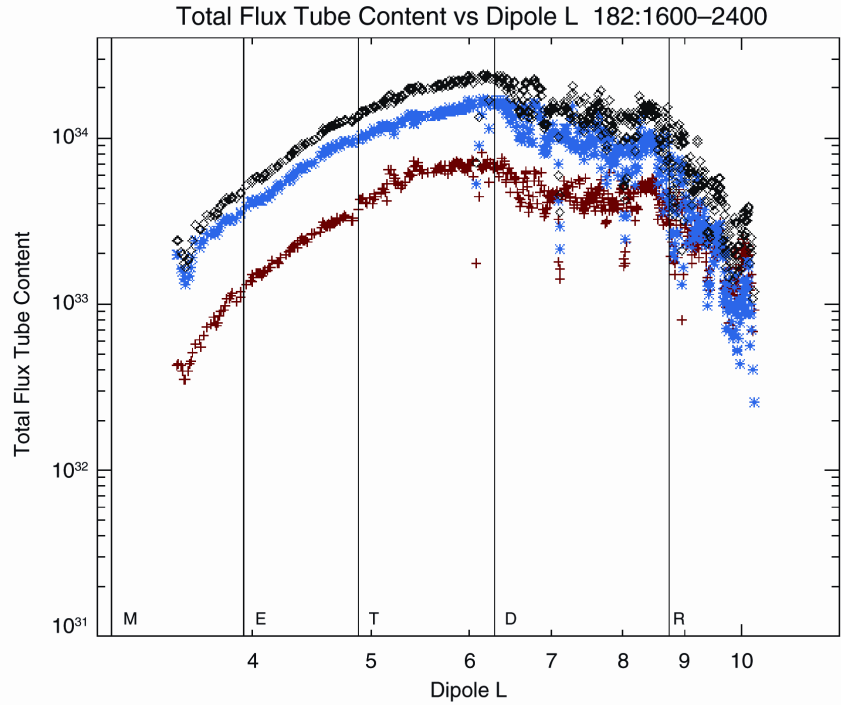


Fig. 39 Total flux tube content for protons, $n_p L^2$ (red), and for water group ions (blue), $n_w L^2$, and the sum of protons and water group ions (black) plotted as a function of dipole L. Icy satellite L shells are indicated. (from [170]).

tube content profile is shown in Fig. 39. There are two important conclusions to be drawn from Fig. 39: First, the presence of the peak in flux-tube content at $L \sim 6$ suggests that the net plasma transport is inwards inside of that point. Since inward transport would produce supercorotation via the Hill mechanism (process 3 above), the observation of subcorotation in this region requires significant ionization and/or mass-loading there, which agrees with the conclusions of *Saur et al.* [157].

The second important point in Fig. 39 is that beyond the peak in flux-tube content there is substantial variability in the derived values. This variability is due to the action of the interchange instability (described above), which exchanges fully loaded flux tubes from the inner magnetosphere with flux tubes from the outer magnetosphere that contain only hot tenuous plasma (e.g., [86, 30, 6, 7]). As discussed by *Southwood and Kivelson* [177], plasma should be interchange-unstable when the flux-tube content decreases with radial distance, as indeed observed.

Using the neutral torus model of *Johnson et al.* [96] and the electron temperature observed by CAPS, *Sittler et al.* [170] calculated the ion production rate profile corresponding to the SOI observations represented in Fig. 39. They found a broad peak in ion production per unit L between $L \sim 4.5$ and 6.5 . The peak is a convolution of the neutral density, which peaks inside of $L \sim 5$, and the electron energy flux, which falls off rapidly inside $L \sim 6$. The decline in electron energy flux is due to loss of hot electrons delivered from the outer magnetosphere via interchange events, combined with the low local electron temperature produced by collisional coupling to the cool, corotating H^+ [154]. Significant electron impact ionization can only occur for electron energies greater than ~ 20 eV, and the electron temperature falls below this inside of $L \sim 6$ due to the small pick-up energy of H^+ (c.f. Fig. 9). However, the non-thermal tail represented by the hot outer-magnetospheric population diffusing inwards makes a significant contribution to the ionization, even at the low flux levels near Enceladus' orbit [53].

6 Upstream and Solar Wind Boundaries

Saturn orbits the Sun at a heliocentric distance of approximately 9.5 AU. At this distance the nominal Parker spiral is nearly in the azimuthal direction (85° from the radial direction). The out-of-the-ecliptic component of the interplanetary magnetic field (IMF) is typically quite small, well below 1 nT. The solar wind dynamic pressure is approximately two orders of magnitude weaker at Saturn than it is at Earth (it scales with d^{-2} , where d is the heliocentric distance). As discussed earlier in this Chapter, Saturn's intrinsic magnetic field at the planetary equator is comparable to that of Earth. Combined with the fact that there are significant plasma sources deep inside Saturn's inner magnetosphere, it is expected that the solar wind interaction plays an important role

in forming the magnetospheric boundaries (bow shock and magnetopause) but it does not have a major influence on the inner magnetosphere.

6.1 Upstream Conditions

The approach of Cassini to the Saturn system in late 2003 and early 2004 provided an opportunity to study the properties of the upstream solar wind. *Jackman et al.* [90, 91] examined the behavior of the IMF upstream of Saturn during January-June 2004 and found a structure dominated by corotating interaction regions (CIRs). These CIRs produced repeating patterns of compressions and rarefactions in the solar wind occurring at approximately the solar rotation period. Each compression region was typically associated with a crossing of the heliospheric current sheet. We note that if the heliospheric current sheet is slightly tilted, which is usually the case especially in the late declining phase of the solar cycle, we observe a two-sector structure in the ecliptic. This means that there are two current sheet crossings per solar rotation. The repeatability of these compression regions was sufficient for the authors to predict the arrival of a compression region during Cassini's SOI orbit at Saturn. The arrival of this compression was confirmed using in-situ observations, which amongst other findings, showed that the magnetopause was expanded during the inbound pass of Cassini (indicating a rarefaction region) and that the magnetopause was compressed during the outbound pass [57]. More recently, *Jackman et al.* [94] have shown that the typical spiral angle of the IMF near Saturn's orbit is in close agreement with the Parker spiral angle at Saturn's location in the heliosphere. *Jackman et al.* [94] also studied the meridional angle of the field and found a distribution of angles which peaked near zero degrees. Typical field strengths in the solar wind at Saturn were 0.1 nT and $1 - 2\text{ nT}$ in rarefaction and compression regions, respectively.

Solar wind plasma measurements at Saturn have not been obtained routinely due to viewing limitations, but the January 2004 joint Cassini – Hubble Space Telescope (HST) campaign provided an opportunity to study the upstream IMF and solar wind parameters at the same time as HST was observing the ultraviolet aurora. *Crary et al.* [49] used this dataset to show that the solar wind speed varies by approximately 25% about an average of $\sim 525\text{ km s}^{-1}$ whilst the density varies by more than two orders of magnitude. The density was found to be elevated in compression regions and reduced to less than $2 \times 10^{-3}\text{ cm}^{-3}$ in rarefaction regions. The range of solar wind dynamic pressures varied from 10^{-3} nPa to about 0.2 nPa .

Zieger and Hansen [201] have introduced a 1D MHD model of solar wind propagation that is able to provide solar wind predictions at any location in the ecliptic plane between 1 and 10 AU. The boundary conditions at 1 AU are estimated from near-Earth solar wind observations assuming that the solar corona is in a quasi-steady state on the time scale of half a solar rotation. The time dependent MHD solution can be mapped to the location of any moving spacecraft, planet or other celestial body. *Zieger and Hansen* [201] have validated the solar wind propagation model with 12 years of heliospheric observations from the Voyager, Pioneer and Ulysses spacecraft, quantifying the variations of the prediction efficiency both in space and time on a statistical basis. The solar wind predictions at the apparent opposition were found to be highly reliable even at solar maximum. The solar

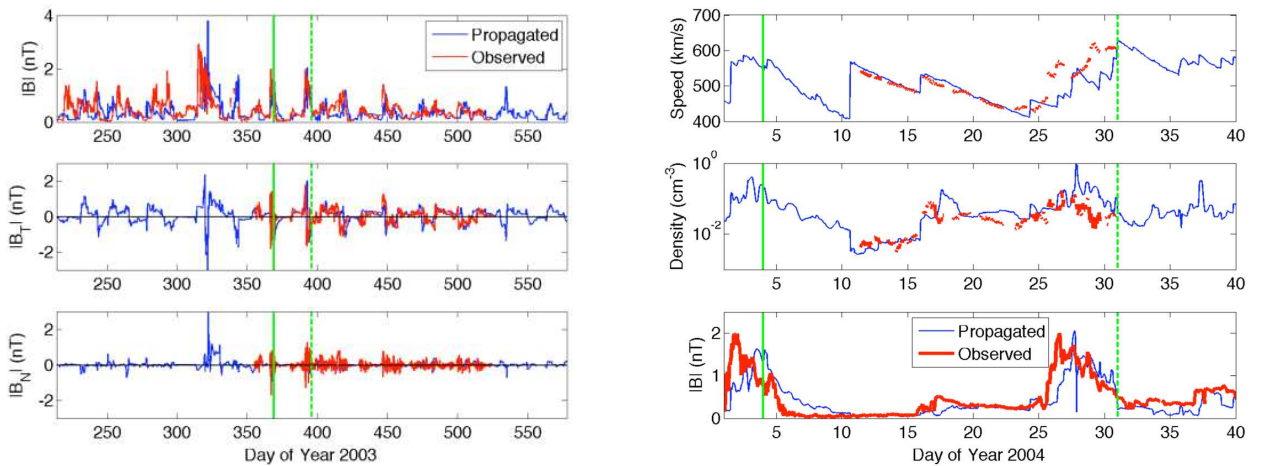


Fig. 40 Propagated and observed solar wind parameters for the 2003-2004 time period. Left panel: Propagated magnetic field values using the *Zieger and Hansen* method [201] compared to Cassini MAG observations [49]. Right panel: Propagated solar wind parameters obtained by the *Zieger and Hansen* method [201] compared to the Cassini CAPS observations [49].

wind speed can be predicted with the highest accuracy, the second best predicted variable is the IMF magnitude, followed by the density. Their statistical analysis of time lags between predicted and observed shocks at 10 AU revealed that the error of shock arrival times is as small as 10–15 hours within 75 days from apparent opposition during solar minimum. The results indicate that predicted shock arrival times tend to be late by at least 10 hours during solar maximum, introducing a systematic error in the shock arrival times that can be incorporated into forecast models. Figure 40 shows a comparison between predicted and observed solar wind parameters for the 2003–2004 period when Cassini was approaching Saturn.

6.2 Foreshock Region

A principal characteristics of interplanetary space near planetary bow shocks is the presence of energetic ions and electrons [109]. The Voyager 1 and 2 flybys in 1980 and 1981, respectively, observed such transient particle enhancements [108] whenever interplanetary magnetic field lines connected the spacecraft to the planetary bow shock. The origin of such bursts of ions cannot be established unambiguously, unless species that are characteristic of a particular source can be identified. For example, S^+ ions upstream of Jupiter are clearly of magnetospheric origin, given the Io plasma source, while He^{++} is a principal constituent of the solar wind and is likely accelerated outside the shock.

The absence of detailed composition and charge state measurements on the Voyagers at lower energies (≤ 0.3 MeV where intensities are highest) made identification of the source plasma difficult. The Cassini instrument complement, however, includes such sensors [110] so it has been possible to characterize these events in detail. Fig. 41 shows data from the MIMI and MAG

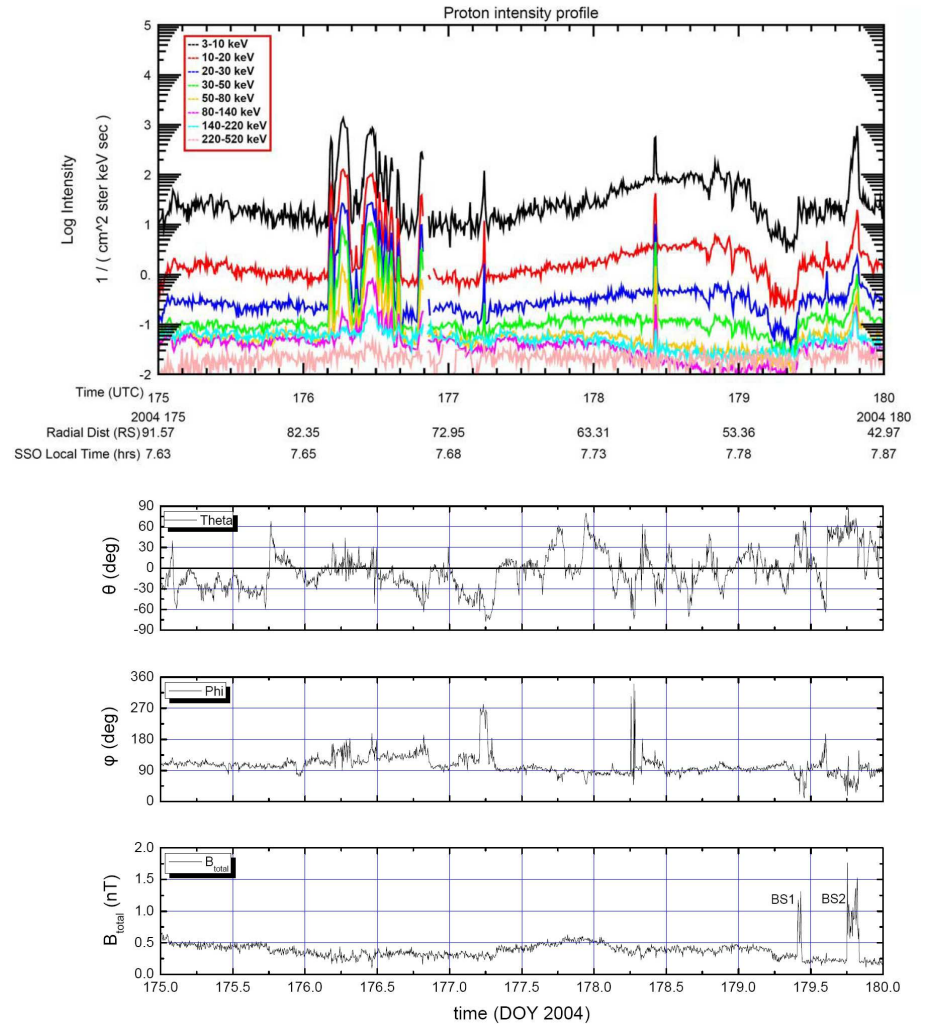


Fig. 41 Time intensity profile of energetic protons (top panel) upstream of Saturn's bow shock at local time ~ 0740 . The spikes on day 176 are shown in detail in the second panel. The lower panels show the direction and magnitude of the IMF (from [113]).

investigations (see [110, 56] for instrument descriptions) during the initial approach of Cassini to Saturn on day 176, 2004. Energetic ions are present throughout this period, from $\sim 92 R_S$ to the first bow shock crossing at $\sim 49 R_S$. Superimposed are discrete, high intensity bursts of varying duration, extending in energy to > 220 keV. Similarly, the IMF (bottom panel) shows notable fluctuations in direction as well as magnitude that correlate well with the particle increases.

The time interval 00:00–15:00 UT of day 176 is shown in more detail in Fig. 42. The top left panel displays an energy spectrogram of protons while the bottom left panels show the IMF direction. Intense increases are well correlated with excursions of the IMF azimuth toward the radial direction, which would connect the spacecraft location (at ~ 0740 local time, $\sim 80 R_S$) to the dawn bow shock. The right panels show that the particle pressure exceeds that of the IMF during each of the bursts, the ratio (plasma β) being as high as ≥ 10 . Detailed angular distribution measurements show that the onset of the event was generally field aligned, but then became isotropic, a characteristic that is common in upstream events at other planets [113].

Beginning with the onset of the events at ~ 0400 UT there are waves in the IMF (bottom trace in Fig. 41) that seemingly correspond to periods of ~ 45 and ~ 22 minutes. A wavelet analysis of the IMF revealed that these were magnetic signatures consistent with the presence of O^+ , and also O^{++} . The analysis of composition and charge state using the MIMI/CHEMS sensor (Fig. 43) shows the presence of H^+ , He^{++} , He^+ , and O^+ at the respective mass per charge locations.

The measurements in Fig. 43 suggest that the source of upstream bursts is the energetic particle population in the magnetosphere of Saturn, since singly charged oxygen is not a constituent of the upstream solar wind, but does represent a key constituent of the magnetospheric population [111]. Protons and helium are present in both, in the upstream solar wind as plasma and in the magnetosphere as an energetic particle population. Thus the most plausible scenario for upstream bursts is one whereby there is nearly continuous leakage of energized particles into the upstream region that are observed whenever the IMF direction is such that it connects the spacecraft to the bow shock. It is not possible to estimate the loss rate with confidence at this time because of the lack of comprehensive statistical studies that can establish the local time dependence and the continuity or intermittency of such escape. It is likely that additional acceleration may possibly occur in the upstream region, considering the turbulence in the IMF, the high beta plasma conditions, and the isotropization of the particle distributions after the initial anisotropies during onset. These and other issues will have to await further data analyses and modeling studies.

At lower energies (< 50 keV), CAPS observations show no evidence for water-group ions in the foreshock region, although there is clearly a suprathermal population of H^+ and He^{++} , as seen upstream from other bow shocks and interplanetary shocks [182]. The implication of this observation is that the energetic water-group ions observed by MIMI were not accelerated in the

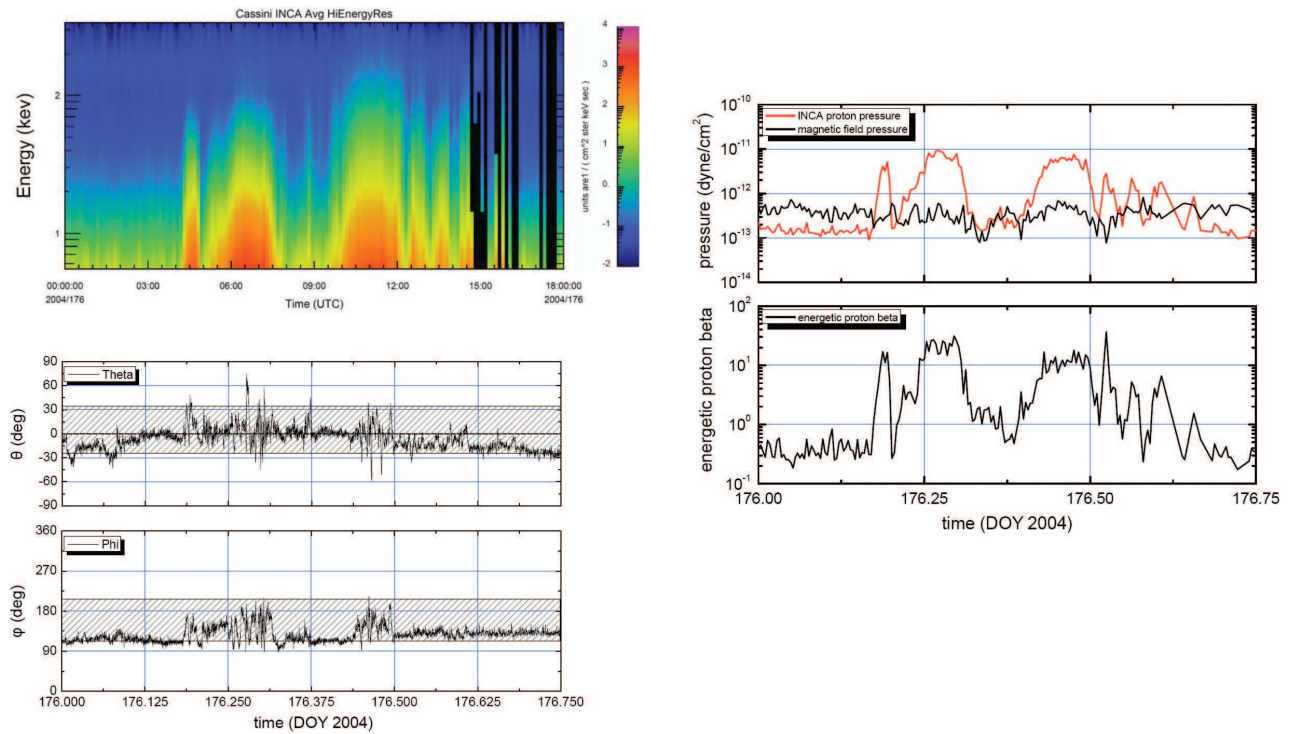
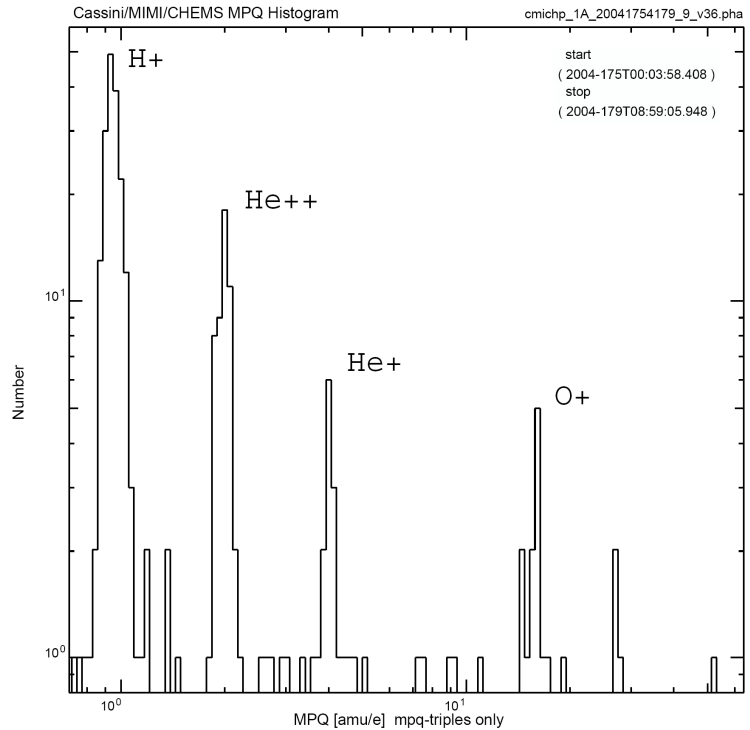


Fig. 42 Energy spectrogram of protons (top left panel) for day 176. The IMF direction and the respective particle and field pressures are shown as line-plots in the left and right panels (from [113]).

Fig. 43 Composition and charge state measurements ($36 < E < 220$ keV/e) with the MIMI/CHEMS sensor suite. A histogram from the standard display of mass vs mass per charge shows all points in the indicated time intervals during the events shown in Figs. 41 and Fig. 42. The histogram shows the clear presence of O^+ at 16 amu/e (from [113]).



foreshock region out of a leaked suprathermal population, but rather are due to direct leakage of already energized magnetospheric particles. The observed suprathermal population with solar-wind composition indicates that shock acceleration of solar wind particles occurs at Saturn's bow shock as at other shocks throughout the solar system.

Low frequency electromagnetic waves have also been detected upstream of Saturn's bow shock using the magnetometer [23]. An analysis of waves below the local proton cyclotron frequency suggested that they were sunward propagating ion-ion resonant right-hand (fast magnetosonic) mode waves that steepen and emit whistler precursors to prevent the steepening process in the non-linear regime. These waves were observed deep into the ion foreshock and *Bertucci et al.* [23] identified them as kronian counterparts of shocklets and discrete wave packets observed in the foreshock of Earth. These waves were found to be typical of the deep ion foreshock and therefore associated with diffuse back-streaming ion distributions. These ions have been observed with Cassini [182] but no direct correlation between superthermal ions and foreshock waves has yet been done.

Waves above the local proton cyclotron frequency were quasi-monochromatic and steepened with a right-handed polarization found closer to the bow shock than the first group. Typically the waves propagated at small angles to the magnetic field but waves with a higher amplitude exhibited a degree of compressibility and propagated obliquely to the field. The presence of apparent sunward propagating whistler precursors attached to the steepened waves led to the suggestion that the waves were produced by the ion-ion resonant left-hand instability and propagated sunward in the plasma frame. Again the hot ion distributions associated with these waves have yet to be clearly associated with specific wave events. *Bertucci et al.* [23] presented direct evidence that these waves participate in the reformation of the quasi-parallel bow shock.

Narrow regions of enhanced particle and magnetic pressure called Hot Flow Anomalies (HFA) are a common observation upstream of the terrestrial bow shock. These anomalies are the result of the interaction of an interplanetary current sheet with the bow shock. *Masters et al.* [122] presented Cassini observations from upstream of Saturn's bow shock which had characteristics similar to terrestrial HFAs. The analysis confirmed that the anomalies were the result of the interaction between a current sheet and the bow shock which focused energetic particles into the current sheet and formed the anomaly. In contrast with terrestrial HFAs the kronian HFAs were found to be associated with density enhancements (rather than depressions) and more modest electron heating. Estimates of the total pressure inside the HFAs suggested that their central regions were expanding. Subsequent analysis of at least one additional HFA event has revealed a profile much more similar to those seen in the terrestrial foreshock, including the strongly reduced internal density and strong flow deflection.

During the approach of Cassini to Saturn the CDA instrument observed high speed streams of nanometer-sized dust originating from the inner kronian system [103]. The dust grains were observed more often in corotating interaction regions, showing that once in the interplanetary medium the grains interact electromagnetically with the interplanetary magnetic field. Modelling and observations showed that the dust grains have radii between 2 and 25 nm, move with a speed in excess of 100 km/s, and are

composed primarily of silicon, suggesting that they are impurities in the ices in Saturn's inner magnetosphere and not of an icy composition.

6.3 Bow Shock and Magnetosheath

The most commonly used pre-Cassini model of Saturn's bow shock was published by *Slavin et al.* [171] based on bow shock crossings observed by Pioneer 11 and Voyagers 1 and 2. The shock crossings were fitted to a conic section with a focus shifted along the aberrated Saturn-Sun line. Since the size of the bow shock is a function of the upstream solar wind dynamic pressure the standoff distance of the bow shock was assumed to be a power-law function of the solar wind dynamic pressure, $R_{BS} \propto P_{sw}^{-1/\alpha}$. *Slavin et al.* [171] found that the compressibility was about $\alpha = 5.1$ with the average subsolar shock distance of $27.7R_S$.

In the era of Cassini-Huygens two empirical models have been developed to describe Saturn's bow shock [123]. An additional study used MHD simulations [81] to investigate the pressure-size relation of the bow shock. For the latter study, *Hansen et al.* [82] tuned the free parameters of the MHD model to match the locations of the boundary crossings identified in the Cassini magnetometer data. The subsolar locations of the bow shock (and magnetopause) were extracted from the simulation and plotted as a function of the solar wind dynamic pressure. *Hansen et al.* [82] found that the bow shock responded to changes in solar wind dynamic pressure with $\alpha \approx 5.9$, a somewhat different power-law than published by *Slavin et al.* [171]. The bow shock was also found to be less flared than that identified by *Slavin et al.* [171].

Two empirical models of Saturn's bow shock [123] use essentially the same dataset of shock crossings observed in Voyager data and Cassini magnetometer and electron spectrometer data, but differ in the way that they determine the upstream dynamic pressure at each crossing. *Masters et al.* [123] assumed a constant solar wind speed at each aberrated shock crossing location and used Langmuir plasma wave observations to estimate the plasma density, hence providing an estimate of the solar wind dynamic pressure. *Masters et al.* [123] fitted the observations to a conic section using a method similar to that employed by *Slavin et al.* [171] where the crossing locations were fitted to a conic section without pressure-correction, then the pressure estimates were used to scale all the crossing locations to a common dynamic pressure and the model was refit. The resulting model is marginally hyperbolic, and thus less flared than the *Slavin et al.* [171] model, and had an average size of $25 \pm 1R_S$ in good agreement with that found by *Slavin et al.* [171]. The power-law exponent was found to be $\alpha = 6 \pm 2$ and hence consistent with *Slavin et al.* [171] but with very large error bars. *Masters et al.* [123] also investigated the effect of the IMF orientation on the shock location but found no clear relationship. Using the model to estimate the shock stand-off distance at each shock crossing suggests that the stand-off distance lies between $18R_S$ and $46R_S$.

6.4 Magnetopause

Jackman et al. [90] presented an empirical voltage formula adapted from studies at Earth, to calculate the reconnection voltage across Saturn's dayside magnetopause, and thus to estimate the amount of open flux added to the system through dayside reconnection. This study indicated that Saturn's magnetosphere is immersed in highly structured solar wind, and reconnection can be driving a Dungey-type convection pattern [59] at least in the outer magnetosphere. More recently *McAndrews et al.* [128] presented *in-situ* evidence for dayside reconnection at Saturn's magnetopause using CAPS data, and they derived a value for the reconnection voltage from one example to be ~ 50 kV, in line with the estimates of *Jackman et al.* [90]. *Badman and Cowley* [18] considered the contribution of the solar wind driven Dungey cycle to flux transport in Saturn's magnetosphere, and found that under conditions of strong solar wind driving, the Dungey cycle return flow will make a significant contribution to the flux transport in the outer magnetosphere. The contribution of the solar wind driving to magnetospheric convection will be discussed in another section of this Chapter (see section 1.3).

6.4.1 Standoff Distance

Before Cassini-Huygens the average location of Saturn's magnetopause was thought to be $\sim 20R_S$. Recently *Achilleos et al.* [2] used an established statistical technique [99] with Cassini observations and the *Arridge et al.* [11] magnetopause model to test this pre-Cassini understanding and establish the long-term statistical behavior of the magnetopause. They obtained the best fit with a bimodal distribution, with peaks at $22R_S$ and $27R_S$ with uncertainties in the range of $1 - 2 R_S$. A similar bimodality of the standoff distance of the Jovian magnetopause was found by *Joy et al.* [99].

To identify the physical origin of this bimodality, *Achilleos et al.* [2] considered both external (i.e., a solar wind origin), and internal (mass-loading/rotational effects) mechanisms. The solar wind at the outer planets has been shown to be dominated by alternating patterns of compressions and rarefactions [90] and so one might expect compression regions to contain enhanced solar wind dynamic pressures. *Achilleos et al.* [2] compared the solar wind dynamic pressure distribution, inferred from the stand-off distance distribution, with solar wind pressures measured by the CAPS instrument [49]. The solar wind pressure distribution did not exhibit the bimodality found in the magnetopause standoff distance. Furthermore, there was no ordering of the standoff distance with heliocentric longitude, as might be expected for a solar wind driver.

Processes internal to the magnetosphere, such as mass loading/release mechanisms and rotational effects can also plausibly account for the observed bimodality. *Clarke et al.* [38] studied a set of magnetopause crossings on the dawn flank that were modulated at a period close to the ~ 10.5 hour periodicity seen in Saturn Kilometric Radiation (SKR) and interpreted these multiple crossings as evidence of an internal rotational anomaly (the camshaft [179]). *Clarke et al.* [38] found that the standoff distance was modulated with a peak-to-trough amplitude of $4R_S$ and interpreted it in terms of the effect of the camshaft. *Achilleos et al.* [2] examined the magnetopause standoff distance as a function of SKR phase [[116] and found no evidence that this rotational anomaly was producing the observed bimodality and concluded that it probably only contributed to producing the observed scatter about the peaks. Thus, it was concluded that internal mass-loading and mass release processes could account for the observed bimodality [2]. Such an effect has also been observed at Jupiter [99].

6.4.2 Compressibility

Pioneer and Voyager studies of the Jovian magnetosphere found that the size of the magnetosphere was unusually responsive to changes in upstream dynamic pressure, compared to the rather stiff terrestrial magnetosphere [171]. The suggestion was made that this reflected the effects of internal plasma stresses in the magnetosphere that were either not present or weaker at Earth (e.g., [172]). Thus, examining and modeling the pressure-dependent size of the kronian magnetopause is a useful diagnostic of the stresses inside the magnetosphere. In modeling studies the relationship between the size of the magnetosphere (typically represented by the location of the sub-solar point on the magnetopause, R_0) and the upstream dynamic pressure is expressed as a power-law:

$$R_{MP} \propto P_{sw}^{-1/\alpha} \quad (10)$$

The radial dependence of dipole field strength implies that the size of the terrestrial magnetopause should scale with pressure $\alpha = 6$. This expectation is consistent with the observed value of $\alpha = 6.6 \pm 0.8$ [164]. The unusually compressive Jovian magnetosphere has a magnetopause that follows a power-law of $\alpha \approx 4.5$ [89], hence R_0 changes more rapidly with P_{sw} than $\alpha = 6$. The physical explanation is that the more stretched the magnetic field lines are on the dayside (due to a combined effect of fast rotation and mass loading of magnetic field lines) the more compressible the magnetic field lines are. Dipole field lines in vacuum are quite “rigid” and this is why the terrestrial magnetopause standoff distance scales approximately as $\alpha = 6$. This is a similar functional form as the size of the shock discussed above, but compressibility of the shock is different than the compressibility of the magnetopause.

Examining data from the first part of the Cassini mission *Arridge et al.* [11] obtained a compressibility of $\alpha = 4.3 \pm 0.4$. This result implied that the kronian magnetosphere was even “softer” than the Jovian one. Recently, *Achilleos et al.* [2] examined a large multi-instrumental data set and obtained a compressibility parameter of $\alpha = 5.17 \pm 0.3$, implying that Saturn’s dayside magnetosphere was actually “stiffer” than Jupiter’s but still much “softer” than Earth’s. This result is in very good agreement with the compressibility value of $\alpha = 5.2$ deduced from a series of numerical simulations early in the Cassini mission [82]. Another recent analysis obtained a somewhat higher value for α ($\alpha = 5.6$). Recently *Achilleos et al.* [2] investigated the compressibility of Saturn’s dayside magnetosphere and concluded that at Saturn the dependence of the magnetopause standoff distance on the solar wind dynamics pressure was best fit with a value of $\alpha = 5.17 \pm 0.3$. While these values show some scatter the emerging picture clearly indicates that Saturn’s dayside magnetopause is somewhat less compressive than the magnetopause of Jupiter and much more compressive than the magnetopause of Earth. For comparison, we think that the best estimates for the compressibilities of Jupiter, Saturn and Earth are $\alpha \approx 4.5, 5$ and 6 , respectively.

As discussed earlier, a more compressible magnetosphere is interpreted as being due to the effect of internal plasma stresses in the magnetosphere. These results suggest that the internal plasma configuration of Saturn’s magnetosphere is quite similar to the Jovian magnetosphere. *Bunce et al.* [27] developed an empirical model for the magnetic moment of the ring current as a function of magnetospheric size and were able to show that the total magnetic moment (intrinsic magnetic field plus ring current) varied strongly with the size of the magnetosphere. They showed that this effect could be produced if a substantial portion of the ring current is generated by centrifugal forces. They went on to argue that this naturally led to the power-law that was consistent with the observed compressibilities of Earth, Jupiter and Saturn.

6.4.3 Shape

Two empirical models of Saturn's magnetopause were available prior to the arrival of Cassini-Huygens at Saturn. *Slavin et al.* [171] fitted conic sections to observed crossings from Pioneer 11 and Voyagers 1 & 2. The fit was highly flared (the conic section had hyperbolic geometry) and the size of the magnetopause followed an $\alpha = 6.1$ power-law. In a separate modeling study *Behannon et al.* [22] described modeling by *Ness et al.* [136] who used Voyager magnetopause crossings to produce a parabolic model which did not have the large flaring of the *Slavin et al.* [171] model.

Using Cassini and Voyager magnetopause crossings, *Arridge et al.* [11] developed an axisymmetric model of Saturn's magnetopause. Axial symmetry about the Saturn-Sun line was assumed, A Newtonian pressure balance was used to estimate the upstream dynamic pressure and the functional form of the magnetopause was assumed to be

$$R_{MP}(\theta, P_{sw}) = AP_{sw}^{-1/\alpha} \left(\frac{2}{1 + \cos \theta} \right)^{\beta - \kappa P_{sw}} \quad (11)$$

Arridge et al. [11] derived the following values for the model parameters: $\alpha = 4.3 \pm 0.4$, $A = 10R_S \pm 1R_S$, $\beta = 0.77 \pm 0.03$ and $\kappa = 1.5 \pm 0.3$.

7 Some Open Questions

After the completion of the Cassini mission (it is expected to plunge into Saturn's atmosphere in 2017) Saturn's magnetosphere will be the most studied planetary magnetosphere other than Earth. However, even at Earth, after literally hundreds of magnetospheric missions, there are many phenomena we do not fully understand. In addition, there are many individual phenomena that are intricately interrelated but we still need to understand the complex, nonlinear relationships between them. Obviously, the even more complex kronian magnetosphere cannot be explored and understood by a few flybys and a single orbiter mission, even if it is as successful as the Cassini mission is.

Here we list some open questions regarding the basic magnetospheric configuration that remain at the end of the Cassini Prime Mission. Hopefully some of these questions will be answered by the Cassini Equinox and Solstice Missions, but some of them will probably wait for the next mission to the Saturn system. Obviously, the questions reflect on the interests and priorities of the authors, and the list by no means is intended to be complete.

With these caveats, here is a list of some open questions:

- *Does the magnetosphere exhibit solar cycle or seasonal changes?*
 - What controls the interplay between the Dungey and Vasyliunas cycles?
 - Do the IMF B_y or B_z have an impact on the magnetospheric configuration?
 - What are the physical processes controlling radial mass transport in the magnetosphere?
 - What controls the periodic mass release to the magnetotail?
- *What is the temporal variability of Enceladus' plumes?* Enceladus is the dominant magnetospheric mass source ejecting ~ 300 kg/s of water into the inner magnetosphere. The plume disperses and becomes ionized, adding about 300 kg/s plasma to the magnetosphere. Cassini observations show close to a factor of two change in the plume output.
 - Is the Enceladus gas production changing with solar cycle or seasons?
 - How does the magnetosphere react to the changes of gas production rate?
 - Is the neutral gas composition different in different plumes? If it changes from plume to plume it would suggest different reservoirs, and conversely, if the composition of the plume is essentially identical in all plumes it would imply the presence of a global ocean below the surface.
- *How is the ionosphere coupled to the magnetosphere?*
 - What are the coupling currents between the ring current and the ionosphere?
 - Are the rings electrodynamically coupled to the ionosphere?
 - How are auroral particles accelerated?
 - How are magnetospheric periodicities coupled to the ionosphere?
 - How is the ionospheric rotation rate coupled to the rotation of the planetary interior?
 - Is there a solar cycle or seasonal variation of magnetospheric rotation periods?
 - Is the ionosphere and/or thermosphere differentially rotating?

- Are there UV satellite footprints on Saturn? (like at Jupiter)
- Is there a significant polar outflow from Saturn's high latitude ionosphere? Does this outflow exhibit seasonal or solar cycle variation?

Needless to say, there are many more questions we need to answer if we want to understand Saturn's complex magnetosphere. We are also certain that as we gain a better understanding of the Saturnian system there will be even more questions to answer. We are in an exciting stage of the exploration of Saturn. The veil starts to lift, but there is so much more to see.

Acknowledgements This work was sponsored by the international Cassini/Huygens Project. Authors were supported by NASA under the following contracts: JPL-1279089 (TIG), JPL-1279973 (AMP) and NASA NNX07AE74G (KKK). Work at JHU/APL (SMK) was supported by NASA under contract NAS5-97271 and NNX07AJ69G and by subcontracts at the University of Maryland and the Office for Space Research and Technology of the Academy of Athens while work at Fundamental Technologies (TPA) was supported by APL subcontract 946749. Work at Los Alamos National Laboratory was conducted under the auspices of the U.S. Department of Energy, with support from NASA grant W-19289. CSA was supported by the STFC rolling grant to MSSL-UCL. NK was supported by the German Bundesministerium für Bildung und Forschung through the Deutsches Zentrum für Luft- und Raumfahrt e.V. under contracts No. 50 OH 0801 and 50 OH 0802, and by the Max Planck Gesellschaft. The authors are indebted to Fran Bagenal for her valuable comments and suggestions.

References

1. Achilleos, N., C. Bertucci, C.T. Russell, G.B. Hospodarsky, A.M. Rymer, C.S. Arridge, M.E. Burton, M.K. Dougherty, S. Hendricks, E.J. Smith and B.T. Tsurutani: Orientation, location, and velocity of Saturn's bow shock: Initial results from the Cassini spacecraft. *J. Geophys. Res.* **111**, A03201, (2006) doi:10.1029/2005JA011297
2. Achilleos, N. C.S. Arridge, C. Bertucci, C.M. Jackman, M.K. Dougherty, K.K. Khurana and C.T. Russell: Large-scale dynamics of Saturn's magnetopause: Observations by Cassini. *J. Geophys. Res.* **113**, A11209, (2008) doi:10.1029/2008JA013265
3. Acuña, M.H., N.F. Ness and J.E.P. Connerney: The magnetic field of Saturn: Further studies of the Pioneer 11 observations. *J. Geophys. Res.* **85**, 5675–5678 (1980)
4. Alexeev, I. I., V. V. Kalegaev, E. S. Belenkaya, S. Y. Bobrovnikov, E. J. Bunce, S. W. H. Cowley, and J. D. Nichols: A global magnetic model of Saturn's magnetosphere and a comparison with Cassini SOI data. *Geophys. Res. Lett.*, **33**, L08101, (2006) doi:10.1029/2006GL025896
5. Anderson, J.D. and G. Schubert: Saturn's gravitational field, internal rotation, and interior structure. *Science* **317**, 1384–1387 (2007)
6. André, N., M. K. Dougherty, C. T. Russell, J. S. Leisner, and K. K. Khurana: Dynamics of the Saturnian inner magnetosphere: First inferences from the Cassini magnetometers about small-scale plasma transport in the magnetosphere. *Geophys. Res. Lett.* **32**, L14S06, (2005) doi:10.1029/2005GL022643
7. André, N., A. M. Persoon, J. Goldstein, J. L. Burch, P. Louarn, G. R. Lewis, A. M. Rymer, A. J. Coates, W. S. Kurth, E. C. Sittler Jr., M. F. Thomsen, F. J. Crary, M. K. Dougherty, D. A. Gurnett and D. T. Young: Magnetic signatures of plasma-depleted flux tubes in the Saturnian inner magnetosphere. *Geophys. Res. Lett.* **34**, L14108 (2007) doi:10.1029/2007GL030374
8. André, N., M. Blanc, S. Maurice, P. Schippers, E. Pallier, T. I. Gombosi, K. C. Hansen, D. T. Young, F. J. Crary, S. Bolton, E. C. Sittler, H. T. Smith, R.E. Johnson, R. A. Baragiola, A. J. Coates, A.M. Rymer, M. K. Dougherty, N. Achilleos, C. S. Arridge, S. M. Krimigis, D. G. Mitchell, N. Krupp, D. C. Hamilton, I. Dandouras, D.A. Gurnett, W. S. Kurth, P. Louarn, R. Srama, S. Kempf, H. J. Waite, L. W. Esposito, and J. T. Clarke: Identification of Saturn's magnetospheric regions and associated plasma processes: Synopsis of Cassini observations during orbit insertion, *Rev. Geophys.* **46**, RG4008, (2008) doi:10.1029/2007RG000238
9. Andrews, D.J., E.J. Bunce, S.W.H. Cowley, M.K. Dougherty, G. Provan and D.J. Southwood: Planetary period oscillations in Saturn's magnetosphere: Phase relation of equatorial magnetic field oscillations and SKR modulation. *J. Geophys. Res.* **113**, A09205 (2008) doi:10.1029/2007JA012937
10. Armstrong, T. P., S. Taherion, J. W. Manweiler, S. M. Krimigis, C. Paranicas, D. G. Mitchell, and N. Krupp: Energetic Ions Trapped in Saturn's Inner Magnetosphere. *Planet. Space Sci.* (in press), 2009.
11. Arridge, C.S., N. Achilleos, M.K. Dougherty, K.K. Khurana and C.T. Russell: Modeling the size and shape of Saturn's magnetopause with variable dynamic pressure. *J. Geophys. Res.* **111**, A11227 (2006) doi:10.1029/2005JA011574
12. Arridge, C.S., C.T. Russell, K.K. Khurana, N. Achilleos, N. André, A.M. Rymer, M.K. Dougherty and A.J. Coates: Mass of Saturn's magnetodisc: Cassini observations. *Geophys. Res. Lett.* **34**, L09108 (2007) doi:10.1029/2006GL028921
13. Arridge, C.S., C.T. Russell, K.K. Khurana, N. Achilleos, S.W.H. Cowley, M.K. Dougherty, D.J. Southwood and E.J. Bunce: Saturn's magnetodisc current sheet. *J. Geophys. Res.* **113**, A03214 (2008) doi:10.1029/2007JA012540
14. Arridge, C.S., K.K. Khurana, C.T. Russell, D.J. Southwood, N. Achilleos, M.K. Dougherty, A.J. Coates and H.K. Leinweber: Warping of Saturn's magnetospheric and magnetotail current sheets. *J. Geophys. Res.* **113**, A08217, (2008) doi:10.1029/2007JA012963
15. Arridge, C.S., N. André, N. Achilleos, K.K. Khurana, C.L. Bertucci, L.K. Gilbert, G.R. Lewis, A.J. Coates, M.K. Dougherty: Thermal electron periodicities at $20R_S$ in Saturn's magnetosphere. *Geophys. Res. Lett.* **35**, L15107, (2008) doi:10.1029/2008GL034132.
16. Badman, S. V., E. J. Bunce, J. T. Clarke, S. W. H. Cowley, J.-C. Gérard, D. Grodent, and S. E. Milan: Open flux estimates in Saturn's magnetosphere during the January 2004 Cassini-HST campaign, and implications for reconnection rates. *J. Geophys. Res.* **110**, A11216, (2005) doi:10.1029/2005JA011240
17. Badman, S.V., S.W.H. Cowley, J.-C. Gérard and D. Grodent: A statistical analysis of the location and width of Saturn's southern auroras. *Ann. Geophys.* **24**, 3533–3545 (2006)
18. Badman, S. V., S. W. H. Cowley: Significance of Dungey-cycle flows in Jupiter's and Saturn's magnetospheres, and their identification on closed equatorial field lines, *Annales Geophysicae* **25**, 941–951 (2007)
19. Barbosa, D.: Titan's atomic nitrogen torus: Inferred properties and consequences for the Saturnian magnetosphere. *Icarus* **72**, 53–61 (1987)

20. Beard, D. B.: The interaction of the terrestrial magnetic field with the solar corpuscular radiation. *J. Geophys. Res.* **65**, 3559–3568 (1960)
21. Beard, D.B. and M.A. Gast: The magnetosphere of Saturn. *J. Geophys. Res.* **92**, 5763–5767 (1987)
22. Behannon, K.W., R.P. Lepping and N.F. Ness: Structure and dynamics of Saturn's outer magnetosphere and boundary regions. *J. Geophys. Res.* **88**, 8791–8800 (1983)
23. Bertucci, C., N. Achilleos, C. Mazelle, G. B. Hospodarsky, M. Thomsen, M. K. Dougherty, and W. Kurth: Low-frequency waves in the foreshock of Saturn: First results from Cassini. *J. Geophys. Res.*, **112**, A09219, (2007)doi:10.1029/2006JA012098
24. Bunce, E. J. and Cowley, S. W. H.: A note on the ring current in Saturn's magnetosphere: Comparison of magnetic data obtained during the Pioneer-11 and Voyager-1 and -2 fly-bys, *Ann. Geophys.*, **21**, 661–669, (2003)
25. Bunce, E. J., Cowley, S. W. H., Wright, D. M., Coates, A. J., Dougherty, M. K., Krupp, N., Kurth, W. S., and Rymer, A. M.: In-situ observations of a solar wind compression-induced hot plasma injection in Saturn's tail. *Geophys. Res. Lett.* **32**, L20S04, doi:10.1029/2005GL022888, 2005.
26. Bunce, E.J., S.W.H. Cowley and S.E. Milan: Interplanetary magnetic field control of Saturn's polar cusp. *Annales. Geophys.* **23**, 1405–1431 (2005)
27. Bunce, E.J., S.W.H. Cowley, I.I. Alexeev, C.S. Arridge, M.K. Dougherty, J.D. Nichols and C.T. Russell: Cassini observations of the variation of Saturn's ring current parameters with system size. *J. Geophys. Res.*, **112**, A10202 (2007) doi:10.1029/2007JA012275
28. Bunce, E.J., C.S. Arridge, S.W.H. Cowley and M.K. Dougherty: Magnetic field structure of Saturn's dayside magnetosphere and its mapping to the ionosphere: Results from ring current modeling. *J. Geophys. Res.* **113**, A02207 (2008) doi:10.1029/2007JA012538.
29. Bunce, E. J., C. S. Arridge, J. T. Clarke, A. J. Coates, S. Cowley, M. K. Dougherty, J.-C. Gerard, D. Grodent, K. C. Hansen, J. D. Nichols, D. J. Southwood, and D. Talboys: Origin of Saturn's aurora: Simultaneous observations by Cassini and the Hubble Space Telescope. *J. Geophys. Res.*, **in press**, (2008) doi:10.1029/2008JA013257
30. Burch, J. L., J. Goldstein, T. W. Hill, D. T. Young, F. J. Crary, A. J. Coates, N. André, W. S. Kurth, and E. C. Sittler Jr.: Properties of local plasma injections in Saturn's magnetosphere. *Geophys. Res. Lett.* **32**, L14S02 (2005) doi:10.1029/2005GL022611
31. Burch, J.L., J. Goldstein, W.S. Lewis, D.T. Young, A.J. Coates, M. Dougherty, and N. André: Tethys and Dione as sources of outward flowing plasma in Saturn's magnetosphere. *Nature*, **447**, 833–835 (2007) doi:10.1038/nature05906
32. Carbary J.F., S.M. Krimigis and W.-H. Ip: Energetic particle microsignatures of Saturn's satellites. *J. Geophys. Res.* **88**, 8947–8958 (1983)
33. Carbary, J.F., D.G. Mitchell, S.M. Krimigis, D.C. Hamilton: Spin-period effects in magnetospheres with no axial tilt. *Geophys. Res. Lett.* **34**, L18107, (2007) doi:10.1029/2007GL030483.
34. Carbary, J.F., D.G. Mitchell, C. Paranicas, E.C. Roelof and S.M. Krimigis: Direct observation of warping in the plasma sheet of Saturn. *Geophys. Res. Lett.* **35**, L24201, (2008) doi:10.1029/2008GL035970
35. Carbary, J. F., D.G. Michell, S.W.H. Cowley, T.W. Hill, P. Zarka: The Dynamics of Saturn's Magnetosphere. **Chapter 11 in this book** (2009)
36. Carr, T. D., J. J. Schauble, and C. C. Schauble: Pre-encounter distributions of Saturn's low frequency radio emission, *Nature* **292**, 745–747 (1981)
37. Carr, T.D., M.D. Desch and J.K. Alexander: Phenomenology of magnetospheric radio emissions. in *Physics of the Jovian Magnetosphere*, edited by A.J. Dessler, (Cambridge University Press, New York 1983), pp. 226–284
38. Clarke, K.E., N. André, D.J. Andrews, A.J. Coates, S.W.H. Cowley, M.K. Dougherty, G.R. Lewis, H.J. McAndrews, J.D. Nichols, T.R. Robinson and D.M. Wright: Cassini observations of planetary-period oscillations of Saturn's magnetopause. *Geophys. Res. Lett.* **33**, L23104 (2006) doi:10.1029/2006GL027821
39. Connerney, J.E.P., M.H. Acuña and N.F. Ness: Saturn's ring current and inner magnetosphere. *Nature* **292**, 724–726 (1981)
40. Connerney, J.E.P., N.F. Ness and M.H. Acuña: Zonal harmonic model of Saturn's magnetic field from Voyager 1 and 2 observations. *Nature* **298**, 44–46 (1982)
41. Connerney, J.E.P., M.H. Acuña and N.F. Ness: Currents in Saturn's magnetosphere. *J. Geophys. Res.* **88**, 8779–8789 (1983)
42. Connerney, J. E. P., M.H. Acuña and N.F. Ness: The Z3 model of Saturn's magnetic field and the Pioneer 11 vector helium magnetometer observations. *J. Geophys. Res.* **89**, 7541–7544 (1984)
43. Cooper, J.F., Nuclear Cascades in Saturn's Rings: Cosmic Ray Albedo Neutron Decay and Origins of Trapped Protons in the Inner Magnetosphere. *J. Geophys. Res.* **88**, 3945–3954 (1983)
44. Cooper, J. F., J.H. Eraker, J.A. Simpson: The Secondary radiation under Saturn's A-B-C rings produced by cosmic ray interactions, *J. Geophys. Res.* **90**, 3415–3427 (1985)
45. Cowley, S. W. H. and Bunce, E. J.: Corotation-driven magnetosphere-ionosphere coupling currents in Saturn's magnetosphere and their relation to the auroras. *Ann. Geophys.* **21**, 1691–1707, (2003)
46. Cowley, S.W.H., E.J. Bunce and R. Prangé: Saturn's polar ionospheric flows and their relation to the main auroral oval. *Annales Geophys.* **22**, 1379–1394 (2004)
47. Cowley, S. W. H., Bunce, E. J., and O'Rourke, J. M.: A simple quantitative model of plasma flows and currents in Saturn's polar ionosphere, *J. Geophys. Res.* **109**, A05212 (2004) doi:10.1029/2003JA010375
48. Cowley, S. W. H., Badman, S. V., Bunce, E. J., Clarke, J. T., Gérard, J.-C., Grodent, D., Jackman, C. M., Milan, S. E., and Yeoman, T. K.: Reconnection in a rotation-dominated magnetosphere and its relation to Saturn's auroral dynamics, *J. Geophys. Res.* **110**, A02201 (2005) doi:10.1029/2004JA010796
49. Crary, F.J., J.T. Clarke, M.K. Dougherty, P.G. Hanlon, K.C. Hansen, J.T. Steinberg, B.L. Barraclough, A.J. Coates, J.-C. Gérard, D. Grodent, W.S. Kurth, D.G. Mitchell, A.M. Rymer, D.T. Young: Solar wind dynamic pressure and electric field as the main factors controlling Saturn's aurorae. *Nature*, **433**, 720–722 (2005)
50. Davis, L. Jr. and E.J. Smith: New models of Saturn's magnetic field using Pioneer 11 vector helium magnetometer data. *J. Geophys. Res.* **91**, 1373–1380 (1986)
51. Davis, L. Jr. and E.J. Smith: A model of Saturn's magnetic field based on all available data. *J. Geophys. Res.* **95**, 15257–15261 (1990)
52. Delamere, P.A. and F. Bagenal, V. Dols, and L. C. Ray: Saturn's neutral torus versus Jupiter's plasma torus. *Geophys. Res. Lett.* **34**, L09105, (2007) doi:10.1029/2007GL029437
53. Delamere, P.A. and F. Bagenal: Longitudinal plasma density variations at Saturn caused by hot electrons. *Geophys. Res. Lett.* **35**, L03107, (2008) doi:10.1029/2007GL031095
54. Delitsky, M.L., and A.L. Lane: Saturn's inner satellites: Ice chemistry and magnetosphere effects, *J. Geophys. Res.*, **107**, 5093 (2002) doi:10.1029/2002JE001855
55. Desch, M.D., and M.L. Kaiser: Voyager measurements of the rotation period of Saturn's magnetic field. *Geophys. Res. Lett.* **8**, 253–256 (1981)

56. Dougherty, M.K., S. Kellock, D. J. Southwood, A. Balogh, E. J. Smith, B. T. Tsurutani, B. Gerlach, K.-H. Glassmeier, F. Gleim, C. T. Russell, G. Erdos, F. M. Neubauer and S. W. H. Cowley: The Cassini magnetic field investigation. *Space Sci. Rev.* **114**, 331–383 (2004)
57. Dougherty, M. K., N. Achilleos, N. André, C.S. Arridge, A. Balogh, C. Bertucci, M.E. Burton, S.W.H. Cowley, G. Erdős, G. Giampieri, K.-H. Glassmeier, K.K. Khurana, J.S. Leisner, F.M. Neubauer, C.T. Russell, E.J. Smith, D.J. Southwood and B.T. Tsurutani: Cassini magnetometer observations during Saturn orbit insertion. *Science* **307**, 1266–1270 (2005)
58. Dougherty, M. K., Khurana, K. K., Neubauer, F. M., Russell, C. T., Saur, J., Leisner, J. S., and Burton, M. E.: Identification of a dynamic atmosphere at Enceladus with the Cassini magnetometer. *Science* **311**, 1406–1409, (2006) doi:10.1126/science.1120985
59. Dungey, J.W.: Interplanetary field and the auroral zones, *Phys. Rev. Lett.* **6**, 47–48, (1961)
60. Esposito, L.W., J.E. Colwell, K. Larsen, W.E. McClintock, A.I.F. Stewart, J.T. Hallett, D.E. Shemansky, J.M. Ajello, C.J. Hansen, A.R. Hendrix, R.A. West, H.-U. Keller, A. Korth, W.R. Pryor, R. Reulke, and Y.L. Yung: Ultraviolet imaging spectroscopy shows an active Saturnian system, *Science* **307**, 1251–1255, (2005)
61. Eviar, A., G. L. Siscoe, J. D. Scudder, E. C. Sittler, Jr., and J. D. Sullivan: The plumes of Titan. *J. Geophys. Res.* **87**, 8091–8103, (1982)
62. Eviar, A., R. L. McNutt, Jr., G. L. Siscoe, and J. D. Sullivan: Heavy ions in the outer Kronian magnetosphere. *J. Geophys. Res.* **88**, 823–831 (1983)
63. Eviar, A., and J. Richardson: Corotation of the Kronian magnetosphere. *J. Geophys. Res.* **91**, 3299–3303 (1986)
64. Fukazawa, K., S. Ogi, T. Ogino, and R. J. Walker: Magnetospheric convection at Saturn as a function of IMF B_z , *Geophys. Res. Lett.* **34**, L01105 (2007) doi:10.1029/2006GL028373
65. Fukazawa, K., T. Ogino, and R. J. Walker: Vortex-associated reconnection for northward IMF in the Kronian magnetosphere. *Geophys. Res. Lett.* **34**, L23201 (2007) doi:10.1029/2007GL031784
66. Gérard, J.-C., D. Grodent, J. Gustin, A. Saglam, J.T. Clarke and J.T. Trauger: Characteristics of Saturn's FUV aurora observed with the Space Telescope Imaging Spectrograph. *J. Geophys. Res.* **109**, A09207, (2004) doi:10.1029/2004JA010513
67. Giampieri, G. and M.K. Dougherty: Modelling of the ring current in Saturn's magnetosphere. *Annales Geophys.* **22**, 653–659 (2004)
68. Giampieri, G. and M.K. Dougherty: Rotation rate of Saturn's interior from magnetic field observations. *Geophys. Res. Lett.* **31**, L16701 (2004) doi:10.1029/2004GL020194
69. Giampieri, G., M.K. Dougherty, E.J. Smith and C.T. Russell: A regular period for Saturn's magnetic field that may track its internal rotation. *Nature* **441**, 62–64 (2006)
70. Gleeson, L.J. and W.I. Axford: An analytical model illustrating the effects of rotation on a magnetosphere containing low energy plasma. *J. Geophys. Res.* **81** 3403–3406 (1976)
71. Gloer, A., T.I. Gombosi, G. Tóth, K.C. Hansen, A.J. Ridley, and A. Nagy: Polar wind outflow model: Saturn results. *J. Geophys. Res.*, **112**, A01304 (2007) doi:10.1029/2006JA011755
72. Goertz, C. K.: Detached plasma in Saturn's front side magnetosphere. *Geophys. Res. Lett.*, **10**, 455–458 (1983)
73. Goldreich, P., and A. J. Farmer: Spontaneous axisymmetry breaking of the external magnetic field at Saturn. *J. Geophys. Res.*, **112**, A05225, (2007) doi:10.1029/2006JA012163
74. Gombosi, T.I., M. Horanyi, K. Kecskemty, T.E. Cravens and A.F. Nagy: Charge exchange in solar wind – cometary interactions. *Astrophys. J.* **268**, 889–898 (1983)
75. Gombosi, T.I.: Preshock region acceleration of implanted cometary H^+ and O^+ . *J. Geophys. Res.* **93**, 35–47, (1988)
76. Gombosi, T.I.: *Physics of the Space Environment*. (Cambridge, New York (1998)
77. Gombosi, T. I., G. Tóth, D. L. De Zeeuw, K. C. Hansen, K. Kabin, and K. G. Powell: Semi-relativistic magnetohydrodynamics and physics-based convergence acceleration. *J. Comput. Phys.* **177**, 176–205 (2001)
78. Gombosi, T.I. and K.C. Hansen: Saturn's variable magnetosphere, *Science* **307**, 1224–1226 (2005)
79. Gurnett, D.A., W.S. Kurth, G.B. Hospodarsky, A.M. Persoon, T.F. Averkamp, B. Cecconi, A. Lecacheux, P. Zarka, P. Canu, N. Cornilleau-Wehrlin, P. Galopeau, A. Roux, C. Harvey, P. Louarn, R. Bostrom, G. Gustafsson, J.-E. Wahlund, M.D. Desch, W.M. Farrell, M.L. Kaiser, K. Goetz, P.J. Kellogg, G. Fischer, H.-P. Ladreiter, H. Rucker, H. Alleyne, and A. Pedersen: Radio and plasma wave observations at Saturn from Cassini's approach and first orbit. *Science*, **307**, 1255–1259 (2005)
80. Gurnett, D. A., A. M. Persoon, W. S. Kurth, J. B. Groene, T. F. Averkamp, M. K. Dougherty, and D. J. Southwood: The variable rotation period of the inner region of Saturn's plasma disk. *Science*, **316**, 442–445 (2007)
81. Hansen, K.C., T.I. Gombosi, D.L. De Zeeuw, C.P.T. Groth and K.G. Powell: A 3D global MHD simulation of Saturn's magnetosphere. *Adv. Space. Res.*, **26**(10), 1681–1690 (2000)
82. Hansen, K.C., A.J. Ridley, G.B. Hospodarsky, N. Achilleos, M.K. Dougherty, T.I. Gombosi and G. Tth: Global MHD simulations of Saturn's magnetosphere at the time of Cassini approach. *Geophys. Res. Lett.* **32**, L20S06 (2005) doi: 10.1029/2005GL022835
83. Hansen, C.J., L. Esposito, A.I.F. Stewart, J. Colwell, A. Hendrix, W. Pryor, D. Shemansky and R. West: Enceladus' water vapor plume. *Science* **311** 1422–1425 (2006).
84. Hill, T.W. and J.F. Carbary: Centrifugal distortion of the Jovian magnetosphere by an equatorially confined current sheet. *J. Geophys. Res.* **83** 5745–5749 (1978)
85. Hill, T.W.: Inertial limit on corotation. *J. Geophys. Res.* **84**, 6554–6558, (1979)
86. Hill, T. W., A. M. Rymer, J. L. Burch, F. J. Cray, D. T. Young, M. F. Thomsen, D. Delapp, N. Andre, A. J. Coates, and G. R. Lewis: Evidence for rotationally-driven plasma transport in Saturn's magnetosphere. *Geophys. Res. Lett.* **32**, L41S10 (2005) doi: 10.1029/2005GL022620
87. Hill, T.W., M.F. Thomsen, M.G. Henderson, R.L. Tokar, A.J. Coates, H.J. McAndrews, G.R. Lewis, D.G. Mitchell, C.M. Jackman, C.T. Russell, M.K. Dougherty, F.J. Cray and D.T. Young: Plasmoids in Saturn's magnetotail. *J. Geophys. Res.* **113**, A01214, (2008) doi:10.1029/2007JA012626
88. Hospodarsky, G.B., T.F. Averkamp, W.S. Kurth, D.A. Gurnett, J.D. Menietti, O. Santolík, and M.K. Dougherty: Observations of chorus at Saturn using the Cassini Radio and Plasma Wave Science instrument. *J. Geophys. Res.*, **113**, A12206, (2008) doi:10.1029/2008JA013237
89. Huddleston, D. E., C. T. Russell, M. G. Kivelson, K. K. Khurana, and L. Bennett: Location and shape of the Jovian magnetopause and bow shock. *J. Geophys. Res.* **103**, 20,075–20,082 (1998)
90. Jackman, C. M., N. Achilleos, E. J. Bunce, S. W. H. Cowley, M. K. Dougherty, G. H. Jones, S. E. Milan, and E. J. Smith: Interplanetary magnetic field at 9 AU during the declining phase of the solar cycle and its implications for Saturn's magnetospheric dynamics. *J. Geophys. Res.* **109**, A11203, (2004) doi:10.1029/2004JA010614

91. Jackman, C.M., N. Achilleos, E. J. Bunce, B. Cecconi, J. T. Clarke, S. W. H. Cowley, W. S. Kurth, and P. Zarka: Interplanetary conditions and magnetospheric dynamics during the Cassini orbit insertion fly-through of Saturn's magnetosphere. *J. Geophys. Res.* **110**, A10212, (2005) doi:10.1029/2005JA011054
92. Jackman, C. M. and Cowley, S. W. H.: A model of the plasma flow and current in Saturn's polar ionosphere under conditions of strong Dungey-cycle driving, *Ann. Geophys.* **24**, 1029–1055 (2006)
93. Jackman, C. M., C. T. Russell, D. J. Southwood, C. S. Arridge, N. Achilleos, and M. K. Dougherty: Strong rapid dipolarizations in Saturn's magnetotail: In situ evidence of reconnection. *Geophys. Res. Lett.* **34**, L11203, (2007) doi:10.1029/2007GL029764
94. Jackman, C. M., R. J. Forsyth, and M. K. Dougherty: The overall configuration of the interplanetary magnetic field upstream of Saturn, as revealed by Cassini observations. *J. Geophys. Res.* **113**, A08114, (2008) doi:10.1029/2008JA013083
95. Jackman, C.M., C.S. Arridge, N. Krupp, E.J. Bunce, D.G. Mitchell, H.J. McAndrews, M.K. Dougherty, C.T. Russell, N. Achilleos, G.H. Jones and A.J. Coates: A multi-instrument view of tail reconnection at Saturn. *J. Geophys. Res.* **113**, A11213, (2008) doi:10.1029/2008JA013592
96. Johnson, R.E., H. T. Smith, O. J. Tucker, M. Liu, M. H. Burger, E. C. Sittler, and R. L. Tokar: The Enceladus and OH tori at Saturn, *Astrophys. J.* **644**, L137–L139 (2006)
97. Johnson, R. E., J. G. Luhmann, R. L. Tokar, M. Bouhram, J. J. Berthelier, E. C. Sittler, J. F. Cooper, T. W. Hill, H. T. Smith, M. Michael, M. Liu, F. J. Cray, and D. T. Young: Production, ionization, and redistribution of O₂ in Saturn's ring atmosphere. *Icarus* **180**, 393–402, (2006)
98. Johnson, R. E., M. Fam, M. Liu, R. A. Baragiola, E. C. Sittler, Jr., and H. T. Smith: Sputtering of ice grains and icy satellites in Saturn's inner magnetosphere. *Planet. Space Sci.* **56**, 1238–1243 (2008)
99. Joy, S.P., M.G. Kivelson, R.J. Walker, K.K. Khurana, C.T. Russell and T. Ogino: Probabilistic models of the jovian magnetopause and bow shock. *J. Geophys. Res.* **107**, 1309 (2002) doi:10.1029/2001JA009146
100. Jurac, S., R. E. Johnson, J. D. Richardson, and C. Paranicas: Satellite sputtering in Saturn's magnetosphere. *Plan. Space Sci.* **49**, 319–326 (2001)
101. Jurac, S., M. A. McGrath, R. E. Johnson, J. D. Richardson, V. M. Vasyliunas, and A. Eviatar : Saturn: Search for a missing water source. *Geophys. Res. Lett.* **29**, 2172, (2002) doi:10.1029/2002GL015855
102. Kane, M., D.G. Mitchell, J.F. Carbary, S.M. Krimigis and F.J. Cray: Plasma convection in Saturn's outer magnetosphere determined from ions detected by the Cassini INCA experiment. *Geophys. Res. Lett.* **35**, L04102 (2008) doi:10.1029/2007GL032342
103. Kempf, S., R. Srama, M. Horányi, M. Burton, S. Helfert, G. Moragas-Klostermeyer, M. Roy and E. Grün: High-velocity streams of dust originating from Saturn. *Nature*, **433**, 289–291 (2005)
104. Kennel, C.F. and H.E. Petschek: Limit on stably trapped fluxes. *J. Geophys. Res.*, **71**, 1–28 (1966)
105. Khurana, K.K., D.G. Mitchell, C.S. Arridge, M.K. Dougherty, C.T. Russell, C.P. Paranicas, N. Krupp and A.J. Coates: Sources of rotational signals in Saturn's magnetosphere. *J. Geophys. Res.* **114**, A02211 (2009) doi:10.1029/2008JA013312
106. Krimigis, S.M., and T.P. Armstrong, Two-component proton spectra in the inner Saturnian magnetosphere *Geophys. Res. Lett.* **9**, 1143–1146 (1982)
107. Krimigis, S.M. et al., (1981), Low-energy charged particles in Saturn's magnetosphere. Results from Voyager 1. *Science* **212**, 225–231 (1981)
108. Krimigis, S. M., J. F. Carbary, E. P. Keath, T. P. Armstrong, L. J. Lanzerotti, and G. Gloeckler: General characteristics of hot plasma and energetic particles in the Saturnian magnetosphere: Results from the Voyager spacecraft. *J. Geophys. Res.*, **88**, 8871–8892 (1983)
109. Krimigis, S. M.: Voyager energetic particle observations at interplanetary shocks and upstream of planetary bow shocks: 1977–1990, *Space Sci. Rev.*, **59**, 167–201 (1992)
110. Krimigis, S. M., D. G. Mitchell, D. C. Hamilton, S. Livi, J. Dandouras, S. Jaskulek, T. P. Armstrong, A. F. Cheng, G. Gloeckler, K. C. Hsieh, W.-H. Ip, E. P. Keath, E. Kirsch, N. Krupp, L. J. Lanzerotti, B. H. Mauk, R. W. McEntire, E. C. Roelof, B. E. Tossman, B. Wilken, and D. J. Williams: Magnetosphere Imaging Instrument (MIMI) on the Cassini Mission to Saturn/Titan. *Space Sci. Rev.*, **114**(1-4), 233–329 (2004) doi: 10.1007/s11214-004-1410-8
111. Krimigis, S.M., D.G. Mitchell, D.C. Hamilton, N. Krupp, S. Livi, E.C. Roelof, J. Dandouras, T. P. Armstrong, B.H. Mauk, C. Paranicas, P.C. Brandt, S. Bolton, A.F. Cheng, T. Choo, G. Gloeckler, J. Hayes, K.C. Hsieh, W.-H. Ip, S. Jaskulek, E.P. Keath, E. Kirsch, M. Kusterer, A. Lagg, L.J. Lanzerotti, D. LaVallee, J. Manweiler, R.W. McEntire, W. Rasmuss, J. Saur, F.S. Turner, D.J. Williams, and J. Wocj: Dynamics of Saturn's magnetosphere from MIMI during Cassini's orbital insertion. *Science* **307**, 1270–1273 (2005)
112. Krimigis, S.M., N. Sergis, D.G. Mitchell, D.C. Hamilton and N. Krupp: A dynamic, rotating ring current around Saturn. *Nature* **450**, 1050–1053, (2007) doi:10.1038/nature06425
113. Krimigis, S. M., N. Sergis, K. Dialynas, D. G. Mitchell, D. C. Hamilton, N. Krupp, M. Dougherty, and E. T. Sarris: Analysis of a sequence of energetic ion and magnetic field events upstream from the Saturnian magnetosphere. *Planet. Space Sci.* (2009) doi:10.1016/j.pss.2009.02.013
114. Krupp, N., A. Lagg, J. Woch, S.M. Krimigis, S. Livi, D.G. Mitchell, E.C. Roelof, C. Paranicas, B.H. Mauk, D.C. Hamilton, T.P. Armstrong and M.K. Dougherty (2005). The Saturnian plasma sheet as revealed by energetic particle measurements. *Geophys. Res. Lett.* **32**, L20S03, (2005) doi:10.1029/2005GL022829
115. Kurth, W.S., D. A. Gurnett, J. T. Clarke, P. Zarka, M. D. Desch, M. L. Kaiser, B. Cecconi, A. Lecacheux, W. M. Farrell, P. Galopeau, J.-C. Gérard, D. Grodent, R. Prangé, M. K. Dougherty and F. J. Cray: An Earth-like correspondence between Saturn's auroral features and radio emission. *Nature*, **433**, 722–725, (2005)
116. Kurth, W.S., A. Lecacheux, T.F. Averkamp, J.B. Groene and D.A. Gurnett: A Saturnian longitude system based on a variable kilometric radiation period. *Geophys. Res. Lett.* **34**, L02201 (2007) doi:10.1029/2006GL028336
117. Kurth, W.S., T.F. Averkamp, D.A. Gurnett, J.B. Groene: An update to a Saturnian longitude system based on kilometric radio emissions. *J. Geophys. Res.* **113**, A05222, (2008) doi:10.1029/2007JA012861.
118. Kurth, W.S., E.J. Bunce, J.T. Clarke, F.J. Cray, D.C. Grodent, A. P. Ingersoll, U.A. Dyudina, L. Lamy, D.G. Mitchell, A.M. Persoon, W.R. Pryor, J.S. Saur, T. Stallard: Auroral Processes. **Chapter 13 in this book** (2009)
119. Leisner, J.S., C.t. Russell, K.K. Khurana, M.K. Dougherty, and N. André: Warm flux tubes in the E-ring plasma and torus: Initial Cassini magnetometer observations. *Geophys. Res. Lett.*, **32**, L14S08 (2005) doi:10.1029/2005GL022652
120. Leisner, J. S., C. T. Russell, M. K. Dougherty, X. Blanco-Cano, R. J. Strangeway, and C. Bertucci: Ion cyclotron waves in Saturn's E ring: Initial Cassini observations. *Geophys. Res. Lett.* **33**, L11101 (2006) doi:10.1029/2005GL024875
121. Leisner, J.S., C.T. Russell, K.K. Khurana and M.K. Dougherty: Measuring the stress state of the Saturnian magnetosphere. *Geophys. Res. Lett.* **34**, L12103, (2007) doi:10.1029/2007GL029315

122. Masters, A., C. S. Arridge, M. K. Dougherty, C. Bertucci, L. Billingham, S. J. Schwartz, C. M. Jackman, Z. Bebesi, A. J. Coates, and M. F. Thomsen: Cassini encounters with hot flow anomaly-like phenomena at Saturn's bow shock. *Geophys. Res. Lett.*, **35**, L02202, (2008) doi:10.1029/2007GL032371
123. Masters, A., N. Achilleos, M.K. Dougherty, J.A. Slavin, G.B. Hospodarsky, C.S. Arridge and A.J. Coates: An empirical model of Saturn's bow shock: Cassini observations of shock location and shape. *J. Geophys. Res.*, **113**, A10210 (2008) doi:10.1029/2008JA013276
124. Mauk, B.H., S.M. Krimigis and R.P. Lepping: Particle and field stress balance within a planetary magnetosphere. *J. Geophys. Res.* **90**, 8253–8264 (1985)
125. Mauk, B.H., J. Saur, D.G. Mitchell, E.C. Roelof, P.C. Brandt, T.P. Armstrong, D.C. Hamilton, S.M. Krimigis, N. Krupp, S.A. Livi, J.W. Manweiler and C.P. Paranicas: Energetic particle injections in Saturn's magnetosphere. *Geophys. Res. Lett.* **32**, L14S05, (2005) doi:10.1029/2005GL022485
126. Mauk, B.H., D. Hamilton, T. Hill, G. Hospodarsky, R. Johnson, C. Paranicas, E. Roussos, C.T. Russell, D. Shemansky, E. Sittler, R. Thorne: Fundamental Plasma Processes in Saturn's Magnetosphere. **Chapter 12 in this book** (2009)
127. Maurice, S., I. Engle, M. Blanc and M. Skubis: Geometry of Saturn's magnetopause model. *J. Geophys. Res.* **101**, 27053–27059 (1996)
128. McAndrews, H. J., C. J. Owen, M. F. Thomsen, B. Lavraud, A. J. Coates, M. K. Dougherty, and D. T. Young: Evidence for reconnection at Saturn's magnetopause, *J. Geophys. Res.* **113**, A04210, (2008) doi:10.1029/2007JA012581
129. McAndrews, H.J., M.F. Thomsen, C.S. Arridge, C.M. Jackman, R.J. Wilson, M.G. Henderson, R.L. Tokar, K.K. Khurana, E.C. Sittler, A.J. Coates and M.K. Dougherty: Plasma in Saturn's nightside magnetosphere and the implications for global circulation. *Planet. Space Sci.* **in press** (2009) doi:10.1016/j.pss.2009.03.003.
130. McNutt, R.L.: Force balance in outer planet magnetospheres. In *Physics of Space Plasmas*, Proceedings of the 1982-4 MIT Symposia, number 5 in SPI Conference Proceedings and Reprint Series, Eds. Belcher, J., Bridge, H., Change, T., Coppi, B., and Jasperse, J., pp 179–210 (1983) Scientific Publishers, Inc.
131. Menietti, J.D., O. Santolík, A.M. Rymer, G.B. Hospodarsky, A.M. Persoon, D.A. Gurnett, A.J. Coates, and D.T. Young: Analysis of plasma waves observed within local plasma injections seen in Saturn's magnetosphere. *J. Geophys. Res.* **113**, A05213, (2008) doi:10.1029/2007JA012856
132. Mitchell, D. G., K. Hsieh, C. Curtis, D. Hamilton, H. Voss, E. Roelof, and P. C. Brandt: Imaging two geomagnetic storms in energetic neutral atoms. *Geophys. Res. Lett.* **28**, 1151–1155 (2001)
133. Mitchell, D. G., Brandt, P. C., Roelof, E. C., Dandouras, J., Krimigis, S. M., Mauk, B. M., Paranicas, C. P., Krupp, N., Hamilton, D. C., Kurth, W. S., Zarka, P., Dougherty, M. K., Bunce, E. J., Shemansky, D. E.: Energetic ion acceleration in Saturn's magnetotail: Substorms at Saturn? *Geophys. Res. Lett.* **32**, L20S01 (2005) doi:10.1029/2005GL022647
134. Moncuquet, M., A. Lecacheux, N. Meyer-Vernet, B. Cecconi, and W.S. Kurth: Quasi thermal noise spectroscopy in the inner magnetosphere of Saturn with Cassini/RPWS: Electron temperatures and density. *Geophys. Res. Lett.*, **32**, L20S02 (2005) doi:10.1029/2005GL022508.
135. Moritz, J.: Energetic protons at low equatorial altitudes. *Z. Geophys.* **38**, 701–717 (1972)
136. Ness, N.F., M.H. Acuña, K.W. Behannon, L.F. Burlaga, J.E.P. Connerney, R.P. Lepping and F.M. Neubauer: Magnetic field studies by Voyager-2 – Preliminary results at Saturn. *Science* **215**, 558–563 (1982)
137. Paranicas C. and C.F. Cheng: A model for satellite microsignatures for Saturn, *Icarus* **125**, 380–396 (1997)
138. Persoon, A.M., D.A. Gurnett, W.S. Kurth, G.B. Hospodarsky, J.b. Groene, P. Canu, and M.K. Dougherty: Equatorial electron density measurements in Saturn's inner magnetosphere. *Geophys. Res. Lett.* **32**, L23105 (2005) doi:10.1029/2005GL024294
139. Persoon, A.M., D.A. Gurnett, W.S. Kurth, and J.B. Groene: A simple scale height model of the electron density in Saturn's plasma disk. *Geophys. Res. Lett.* **33**, L18106 (2006) doi:10.1029/2006GL027090
140. Persoon, A.M., D.A. Gurnett, O. Santolík, W.S. Kurth, J.B. Faden, J.B. Groene, G.R. Lewis, A.J. Coates, R.J. Wilson, R.L. Tokar, J.-E. Wahlund, and M. Moncuquet: A diffusive equilibrium model for the plasma density in Saturn's magnetosphere. *J. Geophys. Res.* **in press** (2009) doi:10.1029/2008JA013912
141. Pontius Jr., D. H.: Radial mass transport and rotational dynamics, *J. Geophys. Res.* **102**, 7137–7150 (1997)
142. Porco, C.C., P. Helfenstein, P. C. Thomas, A. P. Ingersoll, J. Wisdom, R. West, G. Neukum, T. Denk, R. Wagner, T. Roatsch, S. Kieffer, E. Turtle, A. McEwen, T. V. Johnson, J. Rathbun, J. Veverka, D. Wilson, J. Perry, J. Spitale, A. Brahic, J. A. Burns, A. D. DelGenio, L. Dones, C. D. Murray, and S. Squyres: Cassini observes the active south pole of Enceladus, *Science* **311**, 1393–1401 (2006)
143. Powell, K. G., P. L. Roe, T. J. Linde, T. I. Gombosi, and D. L. D. Zeeuw: A solution-adaptive upwind scheme for ideal magnetohydrodynamics. *J. Comput. Phys.* **154**, 284–309 (1999)
144. Richardson, J. D.: Thermal ions at Saturn: Plasma parameters and implications. *J. Geophys. Res.* **91**, 1381–1390 (1986)
145. Richardson, J.D. and E.C. Sittler: A plasma density model for Saturn based on Voyager observations. *J. Geophys. Res.* **95**, 12019–12031, (1990)
146. Richardson, J.D.: An extended plasma model for Saturn. *Geophys. Res. Lett.*, **22**, 1177–1180 (1995)
147. Richardson, J. D., A. Eviatar, M. A. McGrath, and V. M. Vasyliunas: OH in Saturn's magnetosphere: Observations and implications. *J. Geophys. Res.* **103**, 20,245–20,255 (1998)
148. Richardson, J.D.: Thermal plasma and neutral gas in Saturn's magnetosphere. *Geophys. Res. Lett.* **36**, 501–524 (1998)
149. Richardson, J.D. and S. Jurac: A self-consistent model of plasma and neutrals at Saturn: The ion tori. *Geophys. Res. Lett.* **31**, L24803 (2004) doi:10.1029/2004GL020959
150. Roussos, E.: Interactions of weakly or non-magnetized bodies with solar system plasmas: Mars and the moons of Saturn. (PhD thesis, Technical University Braunschweig, Germany) (2008).
151. Roussos, E., N. Krupp, T. P. Armstrong, C. Paranicas, D.G. Mitchell, S. M. Krimigis, G.H. Jones, K. Dialynas, N. Sergis and D.C. Hamilton: Discovery of a transient radiation belt at Saturn. *Geophys. Res. Lett.* **35**, L22106 (2008) doi:10.1029/2008GL035767
152. Roussos, E., G.H. Jones, N. Krupp, C. Paranicas, D.G. Mitchell, S.M. Krimigis, J. Woch, A. Lagg, and K. Khurana: Energetic electron signatures of Saturn's smaller moons: Evidence of an arc of material at Methone. *Icarus* **193**, 455–464 (2008) doi:10.1016/j.icarus.2007.03.034
153. Russell, C.T.: Outer planet magnetospheres: a tutorial. *Advances in Space Research* **33(11)**, 2004–2020 (2004)
154. Rymer, A.M., B.H. Mauk, T.W. Hill, C. Paranicas, N. André, E.C. Sittler, Jr., D.G. Mitchell, H.T. Smith, R.E. Johnson, A.J. Coates, D.T. Young, S.J. Bolton, M.F. Thomsen, and M.K. Dougherty: Electron sources in Saturn's magnetosphere, *J. Geophys. Res.* **112**, A02201 (2007) doi:10.1029/2006JA012017
155. Rymer, A.M., B.H. Mauk, T.W. Hill, C. Paranicas, D.G. Mitchell, A.J. Coates, and D.T. Young: Electron circulation in Saturn's magnetosphere. *J. Geophys. Res.*, **113**, A01201, (2008) doi:10.1029/2007JA-12589

156. Santos-Costa, D., M. Blanc, S. Maurice, and S. J. Bolton: Modeling the electron and proton radiation belts of Saturn. *Geophys. Res. Lett.* **30**, 2059 (2003) doi:10.1029/2003GL017972
157. Saur, J., B.H. Mauk, A. Kaner and F.M. Neubauer: A model for the azimuthal plasma velocity in Saturn's magnetosphere. *J. Geophys. Res.* **109**, A05217, (2004) doi:10.1029/2003JA010207
158. Seidelmann, P.K., V. K. Abalakin, M. Bursa, M. E. Davies, C. De Bergh, J. H. Lieske, J. Oberst, J. L. Simon, E. M. Standish, P. Stooke and P. C. Thomas: Report of the IAU/IAG working group on cartographic coordinates and rotational elements of the planets and satellites: 2000. *Celes. Mech. Dyn. Astron.*, **82**, 83–110 (2002)
159. Sergis, N., S.M. Krimigis, D.G. Mitchell, D.C. Hamilton, N. Krupp, B.H. Mauk, E.C. Roelof and M.K. Dougherty: Ring current at Saturn: Energetic particle pressure in Saturn's equatorial magnetosphere measured with Cassini/MIMI. *Geophys. Res. Lett.* **34**, L09102, (2007) doi:10.1029/2006GL029223
160. Sergis N., S. M. Krimigis, D. G. Mitchell, D. C. Hamilton, N. Krupp, B. H. Mauk, E. C. Roelof, M. K. Dougherty: Energetic particle pressure in Saturn's magnetosphere measured with the Magnetospheric Imaging Instrument on Cassini. *J. Geophys. Res.* **114**, A02214 (2009) doi:10.1029/2008JA013774.
161. Shemansky, D. E., P. Matheson, D. T. Hall, H.-Y. Hu, and T. M. Tripp: Detection of the hydroxyl radical in the Saturn magnetosphere. *Nature* **363**, 329–331 (1993)
162. Shi, M., R. A. Baragiola, D. E. Grosjean, R. E. Johnson, S. Jurac, and J. Schou: Sputtering of water ice surfaces and the production of extended neutral atmospheres. *J. Geophys. Res.* **100**, 26,387–26,395 (1995)
163. Showalter, M.R., J. N. Cuzzi, and S. M. Larson: Structure and particle properties of Saturn's E Ring. *Icarus* **94**, 451–473 (1991)
164. Shue, J.-H., J. K. Chao, H. C. Fu, C. T. Russell, P. Song, K. K. Khurana and H. J. Singer: A new functional form to study the solar wind control of the magnetopause size and shape. *J. Geophys. Res.* **102**, 9497–9511 (1997)
165. Siscoe, G. L. and Summers, D.: Centrifugally-driven diffusion of iogenic plasma. *J. Geophys. Res.* **86**, 8471–8479, (1981)
166. Sittler, E.C., K.W. Ogilvie and J.D. Scudder: Survey of low-Energy plasma electrons in Saturn's magnetosphere: Voyagers 1 and 2. *J. Geophys. Res.* **88**, 8847–8870 (1983)
167. Sittler, E.C., Jr., M. Thomsen, D. Chornay, M.D. Shappirio, D. Simpson, R.E. Johnson, H.T. Smith, A.J. Coates, A.M. Rymer, F. Crary, D.J. McComas, D.T. Young, D. Reisenfeld, M. Dougherty, and N. André: Preliminary results on Saturn's inner plasmasphere as observed by Cassini: Comparison with Voyager. *Geophys. Res. Lett.*, **32**, L14S07 (2005) doi:10.1029/2005GL022653
168. Sittler Jr., E.C., M. Thomsen, R.E. Johnson, R.E. Hartle, M. Burger, D. Chornay, M.D. Shappirio, D. Simpson, H.T. Smith, A.J. Coates, A.M. Rymer, D.J. McComas, D.T. Young, D. Reisenfeld, M. Dougherty and N. André: Cassini observations of Saturn's inner plasmasphere: Saturn orbit insertion results. *Planet. Space Sci.*, **54**, 1197–1210 (2006)
169. Sittler Jr., E.C., M. Thomsen, R.E. Johnson, R.E. Hartle, M. Burger, D. Chornay, M.D. Shappirio, D. Simpson, H.T. Smith, A.J. Coates, A.M. Rymer, D.J. McComas, D.T. Young, D. Reisenfeld, M. Dougherty and N. André: Erratum to "Cassini observations of Saturn's inner plasmasphere: Saturn orbit insertion results". *Planet. Space Sci.* **55**, 2218–2220 (2007)
170. Sittler Jr., E. C., N. André, M. Blanc, M. Burger, R.E. Johnson, A. Coates, A. Rymer, D. Reisenfeld, M.F. Thomsen, A. Persoon, M. Dougherty, H.T. Smith, R.A. Baragiola, R.E. Hartle, D. Chornay, M.D. Shappirio, D. Simpson, D.J. McComas, D.T. Young: Ion and neutral sources and sinks within Saturn's inner magnetosphere: Cassini results. *Planet. Space Sci.*, **56**, 3–18 (2008)
171. Slavin, J.A., E.J. Smith, J.R. Spreiter and S.S. Stahara: Solar wind flow about the outer planets: Gas dynamic modelling of the Jupiter and Saturn bow shocks. *J. Geophys. Res.* **90**, 6275–6286 (1985)
172. Smith, E.J., L. Davis Jr., D.E. Jones, P.J. Coleman, D.S. Colburn, P. Dyal, C.P. Sonett and A.M.A. Frandsen: The planetary magnetic field and magnetosphere of Jupiter: Pioneer 10. *J. Geophys. Res.* **79**, 3501–3513 (1974)
173. Smith, E.J., L. Davis Jr., D.E. Jones, P.J. Coleman Jr., D.S. Colburn, P. Dyal and C.P. Sonett: Saturn's magnetosphere and its interaction with the solar wind. *J. Geophys. Res.* **85**, 5655–5674 (1980)
174. Smith, H.T., M. Shappirio, E.C. Sittler, D. Reisenfeld, R.E. Johnson, R.A. Baragiola, F.J. Crary, D.J. McComas, and D.T. Young: Discovery of nitrogen in Saturn's inner magnetosphere. *Geophys. Res. Lett.* **32**, L14S03 (2005) doi:10.1029/2005GL022654
175. Smith, H. T., R. E. Johnson, E. C. Sittler, M. Shappirio, D. Reisenfeld, O. J. Tucker, M. Burger, F. J. Crary, D. J. McComas, and D. T. Young: Enceladus: The likely dominant nitrogen source in Saturn's magnetosphere. *Icarus* **188**, 356–66 (2007)
176. Smith, H. T., M. Shappirio, R. E. Johnson, D. Reisenfeld, E. C. Sittler, Jr., F. J. Crary, D. J. McComas, and D. T. Young: Enceladus: A potential source of ammonia products and molecular nitrogen for Saturn's magnetosphere. *J. Geophys. Res.* **113**, A11206 (2008) doi:10.1029/2008JA013352
177. Southwood, D. J., and M. G. Kivelson: Magnetospheric interchange instability. *J. Geophys. Res.* **92**, 109–116 (1987)
178. Southwood, D. J. and M.G. Kivelson: Magnetospheric interchange motion. *J. Geophys. Res.* **94**, 299–308 (1989)
179. Southwood, D.J. and M. G. Kivelson: Saturnian magnetospheric dynamics: Elucidation of a camshaft model. *J. Geophys. Res.* **112**, A12222, (2007) doi: 10.1029/2007JA012254
180. Spahn, F., J. Schmidt, N. Albers, M. Horning, M. Makuch, M. Seiss, S. Kempf, R. Srama, V. Dikarev, S. Helfert, G. Moragas-Klostermeyer, A.V. Krivov, M. Sremcevic, A.J. Tuzzolino, T. Economou and E. Grün: Cassini dust measurements at Enceladus and implications for the origin of the E ring. *Science* **311**, 1416–1418 (2006)
181. Thomsen M.F. and J.A. Van Allen: On the inference of properties of Saturn's ring E from energetic charged particle observations. *Geophys. Res. Lett.*, **6**, 893–896 (1979)
182. Thomsen, M. F., J. P. DiLorenzo, D. J. McComas, D. T. Young, F. J. Crary, D. Delapp, D. B. Reisenfeld, and N. André: Assessment of the magnetospheric contribution to the suprathermal ions in Saturn's foreshock region, *J. Geophys. Res.*, **112**, A05220 (2007) doi:10.1029/2006JA012084
183. Tokar, R. L., R. E. Johnson, M. F. Thomsen, D. M. Delapp, R. A. Baragiola, M. F. Francis, D. B. Reisenfeld, B. A. Fish, D. T. Young, F. J. Crary, A. J. Coates, D. A. Gurnett, W. S. Kurth: Cassini observations of the thermal plasma in the vicinity of Saturn's main rings and the F and G rings. *Geophys. Res. Lett.*, **32**, L14S04 (2005) doi:10.1029/2005GL022690
184. Tokar, R. L., Johnson, R. E., Hill, T. W., Pontius, D. H., Kurth, W. S., Crary, F. J., Young, D. T., Thomsen, M. F., Reisenfeld, D. B., Coates, A. J., Lewis, G. R., Sittler, E. C., and Gurnett, D. A.: The interaction of the atmosphere of Enceladus with Saturn's plasma, *Science*, **311**, 1409–1412, (2006) doi:10.1126/science.1121061
185. Tokar, R.L., R.J. Wilson, R.E. Johnson, M.G. Henderson, M.F. Thomsen, M.M. Cowee, E.C. Sittler, Jr., D.T. Young, H.J. McAndrews, and H.T. Smith: Cassini detection of water group pick-up ions in Saturn's toroidal atmosphere, *Geophys. Res. Lett.* **35**, L14202 (2008) doi:10.1029/2008GL034749

186. Tóth, G., D. L. De Zeeuw, T. I. Gombosi, and K. G. Powell: A parallel explicit/implicit time stepping scheme on block-adaptive grids. *J. Comput. Phys.* **217**, 722–758, (2006)
187. Tsyganenko, N. A.: Modeling of twisted/warped magnetospheric configurations using the general deformation method. *J. Geophys. Res.*, **103**, 23,551–23,653 (1998)
188. Tsyganenko N.A.: A model of the near magnetosphere with a dawn-dusk asymmetry - 1. Mathematical structure. *J. Geophys. Res.*, **107**, 1179, doi:10.1029/2001JA000219 (2002)
189. Tsyganenko N. A.: A model of the near magnetosphere with a dawn-dusk asymmetry - 2. Parameterization and fitting to observations. *J. Geophys. Res.*, **107**, 1176, doi:10.1029/2001JA0002205 (2002)
190. Van Allen, J.A., Randall, B.A., and Thomsen, M.F.: Sources and sinks of energetic electrons and protons in Saturn's magnetosphere, *J. Geophys. Res.* **85**, 5679–5694 (1980)
191. Van Allen, J.A., Absorption of Energetic Protons by Saturn's Ring G. *J. Geophys. Res.* **88**, 6911–6918 (1983)
192. Van Allen, J.A., Energetic particles in the inner magnetosphere of Saturn. in *Saturn*, ed. Gehrels, T., and Matthews, M.S., (University of Arizona Press, Tucson, 1984) pp. 281–317
193. Vasyliūnas, V.M.: Plasma distribution and flow. in *Physics of the Jovian Magnetosphere*, edited by A.J. Dessler, (Cambridge University Press, New York 1983), pp. 395–453
194. Vasyliūnas, V.M.: Comparing Jupiter and Saturn: dimensionless input rates from plasma sources within the magnetosphere. *Ann. Geophys.* **26**, 1341–1343, (2008)
195. Wahlund, J.-E., R. Bostrom, G. Gustafsson, D.A. Gurnett, W.S. Kurth, T. Averkamp, G.B. Hospodarsky, A.M. Persoon, P. Canu, A. Pedersen, M.D. Desch, A.I. Eriksson, R. Gill, M.W. Morooka, and M. André: The inner magnetosphere of Saturn: Cassini RPWS cold plasma results from the first encounter. *Geophys. Res. Lett.*, **32**, L20S09 (2005) doi:10.1029/2005GL022699
196. Waite, J.H., Jr., T.E. Cravens, W.-H. Ip, W.T. Kasprzak, J.G. Luhmann, R.L. McNutt, H.B. Niemann, R.V. Yelle, I. Mueller-Wodarg, S.A. Ledvina, and S. Scherer: Oxygen ions observed near Saturn's A ring. *Science* **307**, 1260–1262 (2005)
197. Waite J.H., M.R. Combi, W.-H. Ip, T.E. Cravens, R.L. McNutt, W. Kasprzak, R. Yelle, J. Luhmann, H. Niemann, D. Gell, B. Magee, G. Fletcher, J. Lunine, W.L. Tseng: Cassini ion and neutral mass spectrometer: Enceladus plume composition and structure. *Science* **311**, 1419–1422 (2006)
198. Waite J.H., D.T. Young, T.E. Cravens, A.J. Coates, F.J. Crary, B. Magee, J. Westlake: The Process of Tholin Formation in Titan's Upper Atmosphere. *Science* **316**, 870–875 (2007)
199. Wilson, R.J., R.L. Tokar, M.G. Henderson, T.W. Hill, M.F. Thomsen and D.H. Pontius Jr.: Cassini plasma spectrometer thermal ion measurements in Saturn's inner magnetosphere. *J. Geophys. Res.* **113**, A12218 (2008) doi:10.1029/2008JA013486
200. D. T. Young, J.-J. Berthelier, M. Blanc, J. L. Burch, S. Bolton, A. J. Coates, F. J. Crary, R. Goldstein, M. Grande, T. W. Hill, R. E. Johnson, R. A. Baragiola, V. Kelha, D. J. McComas, K. Mursula, E. C. Sittler, K. R. Svenes, K. Szeg, P. Tanskanen, M. F. Thomsen, S. Bakshi, B. L. Barraclough, Z. Bebesi, D. Delapp, M. W. Dunlop, J. T. Gosling, J. D. Furman, L. K. Gilbert, D. Glenn, C. Holmlund, J.-M. Illiano, G. R. Lewis, D. R. Linder, S. Maurice, H. J. McAndrews, B. T. Narheim, E. Pallier, D. Reisenfeld, A. M. Rymer, H. T. Smith, R. L. Tokar, J. Vilppola, and C. Zinsmeyer: Composition and dynamics of plasma in Saturn's magnetosphere, *Science* **307**, 1262–1266 (2005)
201. Zieger, B. and K.C. Hansen: Statistical validation of a solar wind propagation model from 1 to 10 AU. *J. Geophys. Res.* **113**, A08107 (2008) doi:10.1029/2008JA013046